Modelling sea-level observations to investigate the source and magnitude of major meltwater pulses during termination 1

Bassett, Sophie Elizabeth

Modelling Sea-Level Observations to Investigate the Source and Magnitude of Major Meltwater Pulses During Termination 1

Sophie Elizabeth Bassett

A thesis submitted for the degree of Doctor of Philosophy at Durham University

Department of Earth Sciences

2006

Modelling Sea-level Observations to Investigate the Source and Magnitude of Major Meltwater Pulses During Termination 1

S. E. Bassett

Ph. D. 2006

Abstract

The research presented in this thesis utilises available near and far-field sea-level records to provide constraints on the major rapid sea-level rise events that occurred during the most recent period of deglaciation (Termination 1).

The far-field modelling results show that previous, large discrepancies between predictions and observations of sea-level at Barbados, Huon, Tahiti and Sunda Shelf can be resolved by utilising a model of glacial isostatic adjustment characterised by a high viscosity lower mantle (4×10^{22} Pa s) and a major Antarctic contribution (~15 m) to meltwater pulse IA (~14.5-13.5 cal. kyr BP). The latter constraint is contrary to previous suggestions that this event was sourced from northern hemisphere ice sheets, and adds further to the hypothesis that an Antarctic source for mwp-IA is a possible mechanism to explain the progression of millennial scale climatic events that occurred during Termination 1. Furthermore, the far-field sea-level records preclude the existence of the smaller meltwater pulse IB event (~11 cal. kyr BP) and can not conclusively rule out a meltwater pulse event at 19 cal. kyr BP.

Modelling of all available near-field sea-level data from the coast of Antarctica supports the far-field results in that the data do not preclude a dominant Antarctic source to mwp-IA and indicate that this event may have been caused by rapid melting of the Weddell and Ross Sea regions.

Declaration

I hereby declare that this thesis is a record of work undertaken by myself, that it has not been the subject of any previous application for a degree, and that all sources of information have been duly acknowledged.

Acknowledgements

First and foremost, I would like to thank my supervisor Glenn Milne for his extensive support, friendship and encouragement during my time in Durham. I would also like to thank Jerry Mitrovica, Mike Bentley and Peter Clark for their guidance and discussions about this work.

Many thanks to all Earth Sciences staff and students for all their hard work for making the department an easy and enjoyable place to work especially Chris for his help with GMT and juggling. Special thanks to Lisa and Kirstin for their constant friendship and coffee breaks.

The endless support and patient ears of my family have been much appreciated, especially my parents for their understanding and accommodation. I am also grateful for all the kind encouragement and interest from the Baker family over the last couple of years.

Many friends and housemates have made my time in Durham an enjoyable one with special thanks to Glenn, Sylvie, Sophie, Paul, Rachel, Jen, Padraig, Jens, Wibke, Jon and Stuart. Particular thanks go to John Collins and Sue Roy for their attention to the garden during my absence and to Anna Stork and Nancy Moss for maintaining my sanity during my stay in California.

Financial support from NERC, the department of Earth Sciences made this research possible.

Finally for the friendship, love, support and encouragement (and van) of Nick Baker I am forever grateful.

Contents

Abstract ii

Declaration iii

Acknowledgements iv

Contents v

List of Tables viii

List of Figures ix

Chapter 1 Introduction 1

1.1 Ice Age Climate Change 1

1.2 Ice Sheets and Sea-level Change 5

1.3 Outline of Thesis 11

1.4 Theory 13

Chapter 2 Far Field Sea-Level Modelling of Mwp-IA 16

2.1 Introduction 16

2.2 Observational Data 17

2.2.1 Barbados 17

2.2.2 Sunda Shelf 19

2.2.3 Huon Peninsula 23

2.2.4 Tahiti 23

2.3 Modelling 24

2.3.1 Sensitivity of Predictions to Source of Mwp-IA 26

2.3.2 Increasing the Antarctic Contribution to Mwp-IA 27

2.3.3 Exploring other Source Scenarios.....33

2.3.4 Understanding the Results 35

2.3.5 Sensitivity of Predictions to Earth Model Viscosity Structure...40

2.3.6 Understanding the Results 44

2.4 Discussion and Summary.....49

Chapter 3 Far-Field Sea-Level Modelling of Mwp-IB and the 19 kyr Pulse..

.....52

3.1 Introduction.....52

3.2 Modelling of Mwp-IB.....53

3.3 Exploring the LGM misfit 58

3.4 Modelling the 19 cal. kyr pulse 62

3.5 Discussion and Summary.....70

Chapter 4 Near Field Sea-level Modelling of the Antarctic.....73

4.1 Introduction.....73

4.2 Observational Data 76

4.3 Modelling.....80

4.3.1 Input Ice Histories.....81

4.3.2 Sensitivity of Predictions to Antarctic versus North American Source 82

4.3.3 Sensitivity of Predictions to Earth Viscosity Structure 87

4.3.4 Sensitivity of Predictions to Geometry of Antarctic Source.....92

4.4 Discussion and Summary.....97

Chapter 5 Discussion and Summary.....100

5.1 Summary of Key Results 100

5.2 Future Work.....102

Bibliography.....104

List of Tables

Table 3.1: χ^2 values for a number of different viscosity and ice models as discussed in the text. 56

Table 3.2: Table to show the eustatic contributions from each ice sheet in the various ice models used to generate the results in Figure 3.6. 65

Table 3.3: χ^2 values for the period from LGM to present day for a number of different source models for 19 cal. kyr BP event as discussed in the text....66

Table 3.4: Same as Table 3.3 except the $\chi 2$ values are calculated for the time period shown in Figure 3.7 only. 69

List of Figures

Figure 1.1: Marine (delta) oxygen isotope record over the last 0.7 Myr 2

Figure 1.2: Ice core determined oxygen isotope records (a proxy for ancient air temperature) and sea-level variations during Termination 1 3

Figure 1.3: The effect of meltwater influx on the thermohaline circulation 5

Figure 1.4: Sea level observations from three far-field locations 8

Figure 1.5: Normalised (dimensionless) sea-level change associated with different melt scenarios. 10

Figure 2.1: Sea-level observations at four sites based on the indicators described in detail in the text 18

Figure 2.2: Predictions and map showing the large spatial gradient in sea-level across the Sunda Shelf region 22

Figure 2.3: Sea-level predictions based on the reference earth model and a range of melt scenarios. 28

Figure 2.4: Flow chart to illustrate the scaling process employed to fit the models to the Barbados sea-level record 30

Figure 2.5: Predicted sea-level change, in metres, over the past 13 cal. kyr relative to the predicted change at Barbados. 32

Figure 2.6: Sea-level predictions for Tahiti, Huon Peninsula and Sunda Shelf within the Lateglacial time window for four different source scenarios for the mwp-IA event 34

Figure 2.7: The total sea-level prediction at Barbados for a model run in which there is a 0 m contribution to mwp-IA from Antarctica split into the spatially uniform and spatially varying components 35

Figure 2.8: The spatially varying components of the sea-level signal at all four far-field sites for 0 m eustatic and 15 m eustatic contributions to mwp-IA from Antarctica 37

Figure 2.9: Sea-level predictions based on 0 m eustatic contribution from Antarctica to mwp-IA for three earth models with different lithospheric thicknesses.....41

Figure 2.10: Sea-level predictions based on a 0 m eustatic contribution from Antarctica to mwp-IA for three earth models with different upper mantle viscosities.....42

Figure 2.11: Sea-level predictions based on a 0 m eustatic contribution from Antarctica to mwp-IA for three earth models with different lower mantle viscosities.....43

Figure 2.12: The effect of altering the lower mantle viscosity on the spatially varying component of the total sea-level signal.....45

Figure 2.13: Normalised χ^2 misfit between predictions generated using GIA models tuned to the Barbados sea-level record and post-LGM observations as a function of lower mantle viscosity.....47

Figure 2.14: Sea-level predictions based on a dominant Antarctic contribution (15 m eustatic) to mwp-IA for three earth models with different lower mantle viscosities.....48

Figure 3.1: The effect of including mwp-IB on sea-level predictions based on a dominant Antarctic contribution (15 m eustatic) to mwp-IA for an earth model with lower mantle viscosity of 5 x 10^{22} Pa s. 55

Figure 3.2: Sea-level predictions based on a dominant Antarctic contribution to mwp-IA and no distinct mwp-IB event for earth models with lower mantle viscosity of 3 x 10^{22} Pa s and 4 x 10^{22} Pa s.....57

Figure 3.3: Comparison of observed and predicted sea levels at Bonaparte Gulf for the two best fitting earth models of Section 3.2. 59

Figure 3.4: Sea-level predictions based on an earth model with lower mantle viscosity of 4 x 10^{22} Pa s and a range of melt scenarios.....60

Figure 3.5: Normalised χ^2 misfit between predictions for an earth model with a lower mantle viscosity of 4 x 10^{22} Pa s at four locations for a range of Antarctic contributions to mwp-IA.....62

Figure 3.6: Sea-level predictions based on an earth model with lower mantle viscosity of 4 x 10^{22} Pa s and a range of melt scenarios to illustrate the sensitivity to changes in the relative contributions of the N. American, European and Antarctic ice sheets to the 19 cal. kyr BP event 64

Figure 3.7: Same as Figure 3.6 except only the LGM data and predictions for Barbados, Bonaparte Gulf and Sunda Shelf have been shown.....68

Figure 3.8: The Bonaparte Gulf data and predictions for the 19 cal. kyr BP pulse melt scenarios. The inset shows the younger data and predictions accounting for the spatial variation across the data 70

Figure 4.1: Location map for data sites used in this chapter. 75

Figure 4.2: Sea-level observations at the eight sites shown in Figure 4.1 and discussed in detail in Section 4.2.....77

Figure 4.3: Sea-level predictions based on the reference earth model and two end member mwp-IA source scenarios. 84

Figure 4.4: Sea-level predictions based on the sole northern hemisphere and dominant Antarctic mwp-IA scenarios shown in Figure 4.3 for three earth models with different lithospheric thicknesses.....88

Figure 4.5: The same as Figure 4.4 except that the upper mantle viscosity is varied. 89

Figure 4.6: The same as Figure 4.4 except that the lower mantle viscosity is varied 90

Figure 4.7: Sea-level predictions based on the reference earth model and three different models of Antarctic mwp-IA melt scenarios. 94

Figure 4.8: Sea-level predictions based on a revised version of the combined (Ross/Weddell) model of Figure 4.7.....96

Chapter 1 Introduction

1.1 Ice Age Climate Change

Recent Earth history has been defined by the existence of large continental ice sheets that have grown and melted in a quasi-periodic fashion (see Figure 1.1). The most recent of these glacial cycles began around 120,000 years ago, following a relatively warm interglacial period during which northern hemisphere ice cover was thought to be limited to Greenland and a small number of mountain glaciers. Global ice volume reached its maximum around 21,000 years ago: this event is referred to as the Last Glacial Maximum (LGM). During this period there was extensive glaciation of many high latitude northern hemisphere locations (e.g. North America, Greenland and North West Europe) and there was also increased glacial coverage of the southern hemisphere although this was limited mainly to the Antarctic continent due to the lack of land coverage at high latitudes. The causes of the Late Pleistocene glacial cycles and the triggers for moving from glaciated periods to interglacial periods are governed by a number of factors. In order to determine the effect on future climate change of these glaciation cycles, past events must be studied.

The Milankovitch theory partly explains the long period cycles of glaciation and deglaciation by the variation of solar radiation received by the Earth as a result of changes in the Earth-Sun orbit. There are, however, a number of more rapid events that cannot be explained by the Milankovitch theory. These events include

so-called "terminations" (see Figure 1.1), which mark the rapid transition between full glacial and interglacial conditions within ~10 kyr as well as more rapid events that occur in ~1 kyr or less, so-called "millennial-scale" events.

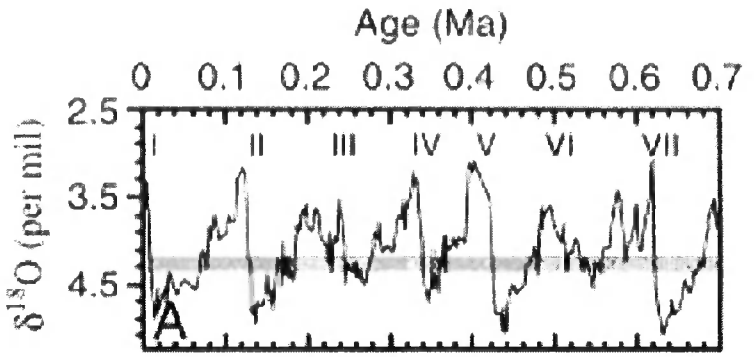

Figure 1.1: Marine (delta) oxygen isotope record from ocean drilling programme (ODP) site 849 as a proxy for global ice volume over the last 0.7 Myr. Terminations I-VII are labelled. From [1].

In this thesis I look at the Termination 1 event (Figure 1.1 and Figure 1.2) which is the period of rapid deglaciation following the LGM (~21,000 calibrated years BP to ~7,000 yrs BP). Although this period shows an overall warming resulting in the deglaciation of the ice sheets, there occurred a number of more rapid and short-lived millennial-scale temperature variations: for example, those associated with the Bølling Allerød warm interval (~14 calibrated kyr before present (cal. kyr BP)) and the Younger Dryas cold interval (~11 cal. kyr BP) (Figure 1.2). The Earth's climate and the growth and melting of ice sheets are linked through a number of processes including, for example, surface albedo, topographic effects, melt water discharge, and iceberg calving (e.g. [1, 2]). Constraining the history of the major ice reservoirs is therefore a key step towards interpreting different climate records and advancing our understanding of forcings and feedbacks within the climate system. In this thesis I aim to apply this philosophy to the primary climatic events that occurred during Termination 1.

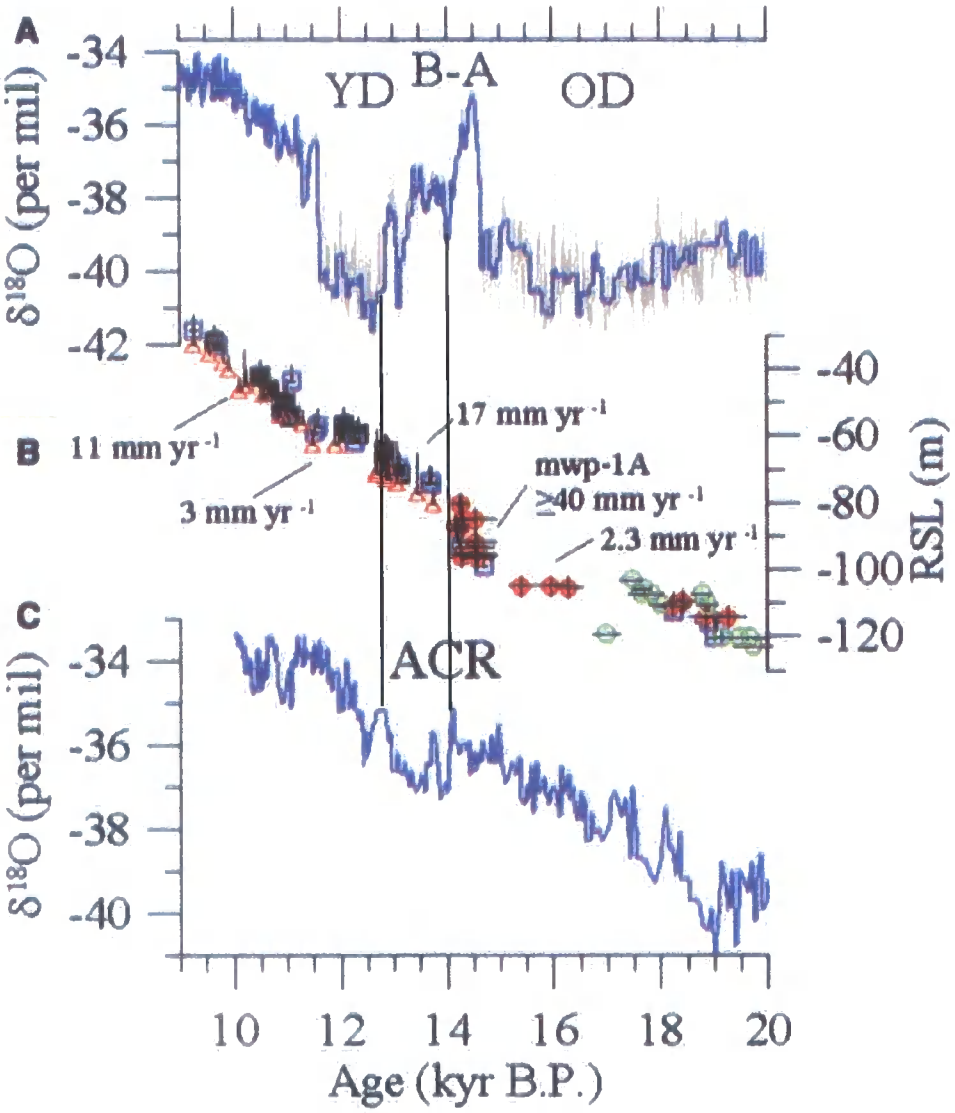

Figure 1.2: Ice core determined oxygen isotope records (a proxy for ancient air temperature) and sea-level variations during Termination 1. **(A)** Greenland ice sheet project 2 (GISP2) oxygen isotope record where OD is the Oldest Dryas cold interval, YD is the Younger Dryas cold interval and B-A is the Bølling Allerød warm interval. **(B)** The combined relative sea-level data from far-field locations (Bonaparte Gulf, Sunda Shelf, Barbados, Tahiti and Huon (see Sections 2.2 and 3.3 for detailed descriptions of these data). **(C)** The Byrd oxygen isotope record. ACR is Antarctic cold reversal. From [3].

Figure 1.2 shows that the northern and southern hemispheres have exhibited very different temperature profiles during Termination 1. The southern hemisphere has been marked by a gradual warming followed by a sudden cooling (the Antarctic Cold Reversal) (Frame C). The northern hemisphere, however, shows a rapid

warming event (the Bølling Allerød warm interval) followed by a cold period (Younger Dryas) (Frame A). The relative sea-level record (Frame B) shows a rapid sea-level rise event (mwp-IA) occurring at about the time of the Bølling Allerød warm interval and preceding the Antarctic Cold Reversal and the Younger Dryas event. The freshwater influx to the oceans associated with a rapid sea-level rise event such as mwp-IA would have a dramatic influence on the global climate.

Previous melt source scenarios for mwp-IA which contain a dominant North American contribution have been unable to adequately explain the effect of a large freshwater forcing in the North Atlantic coincident with the Bølling Allerød warm interval and an active thermohaline circulation [4]. A large freshwater influx to the North Atlantic would weaken the thermohaline circulation in the Atlantic and cause an associated cooling in the northern hemisphere (Figure 1.3, Frame B) which is contrary to the dramatic warming associated with the onset of the Bølling Allerød interval [4].

Recently, however, work by Weaver et al. [3] has suggested that prolonged warming of the southern hemisphere (Frame C) resulted in the partial collapse of the Antarctic ice sheet. Using a climate model, Weaver et al. [3] showed that a freshwater influx to the southern oceans results in a strengthening of the thermohaline circulation causing a warming of the northern hemisphere (Figure 1.3, Frame A) (the Bølling Allerød) and an associated cooling in the southern hemisphere (the Antarctic Cold Reversal). The warming of the northern hemisphere may then have resulted in the melting of the northern hemisphere ice sheets and a freshwater forcing in the North Atlantic resulting in a weakening of the thermohaline circulation and an associated cooling in the northern hemisphere (the Younger Dryas) (Figure

1.3, Frame B).

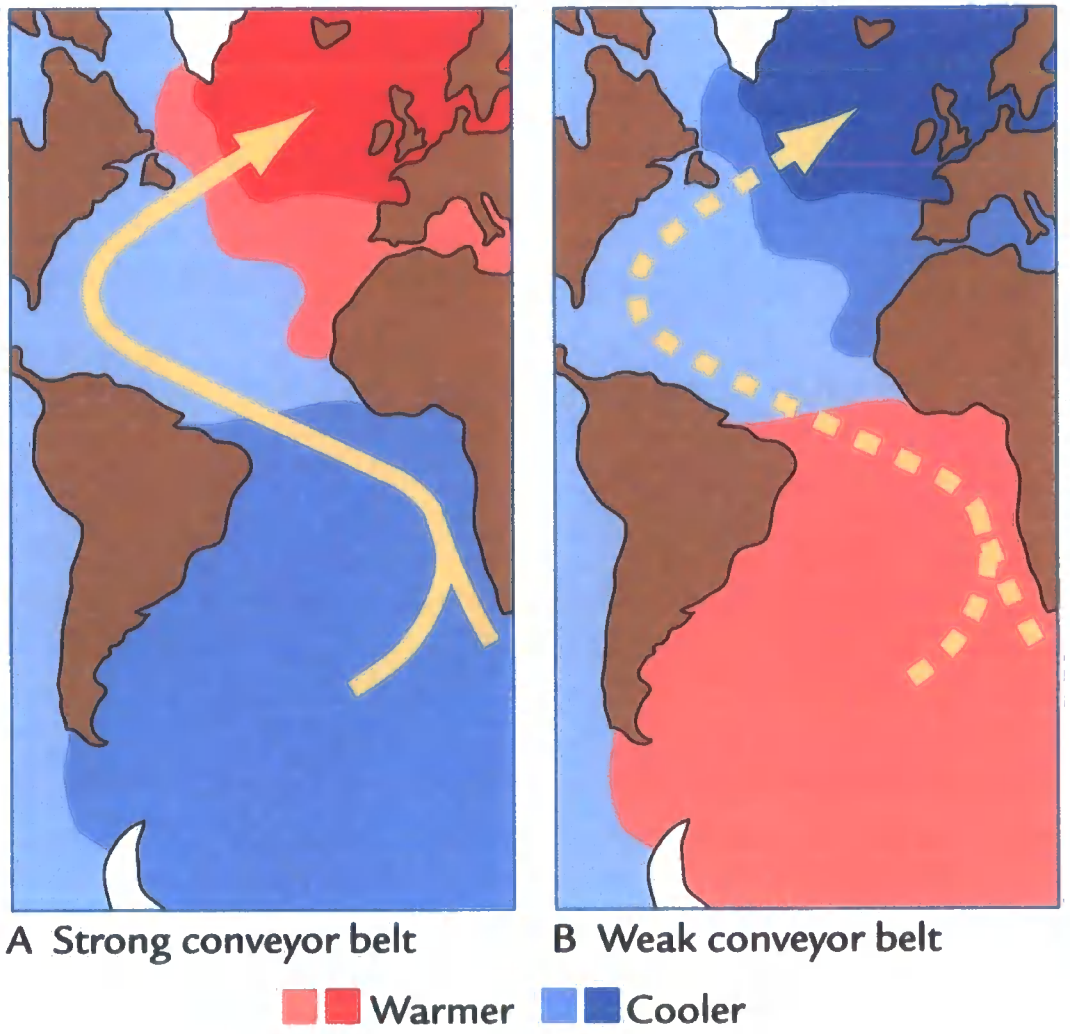

Figure 1.3: The effect of meltwater influx on the thermohaline circulation. (A) Strong Atlantic circulation results in a warm northern hemisphere and a cool southern hemisphere. (B) Weakening the circulation causes the opposing effect. From [5].

1.2 Ice Sheets and Sea-level Change

Observations of sea-level change are one of the principal data sets used to constrain the space-time history of past ice sheets. The surface ice-water mass redistribution associated with glaciation and deglaciation acts to perturb both the solid surface of the Earth and the gravity field, leading to a distinct spatial pattern in

sea-level change ([6, 7]). Sea-level records in regions close to areas of previous glaciation (so called near-field sites) are sensitive to variations in the local ice history and the associated isostatic response of the solid Earth. These observations have, therefore, been employed to infer information relating to both local ice and earth parameters, and, to a lesser extent, the global meltwater influx. (e.g. [8-14]). In regions distant from major glaciation centres (so-called "far-field" locations), the influx of glacial meltwater is the dominant component of the signal producing an overall sea-level rise. As a result, far-field observations have provided the most useful constraints on the net volume and rates of change of global ice from the LGM to the present (e.g. [13, 15-19]). The work described in this thesis is concerned with utilising available near and far-field sea-level records to constrain details of global ice history during Termination 1 and information about deep earth structure. The primary focus of the work presented here is to examine three rapid sea-level rise events or meltwater pulses that have been identified in far-field data records.

Far-field observations from Barbados [20], Bonaparte Gulf [21] and the Sunda Shelf [22] show a sea-level rise of ~120-130m from the LGM to present (see Figure 1.4). The sea-level records from two of these far field sites, Barbados and Sunda Shelf [20, 22], resolve a rapid rise in sea level of ~20-30 m around 14.5 cal. kyr BP (Figure 1.4, Frames A and B). This event, termed meltwater pulse IA (mwp-IA), accounts for 20 – 25% of the total sea-level rise since the LGM. A further meltwater event termed meltwater pulse IB (mwp-IB) has also been identified in the Barbados record [20]. Mwp-IB is smaller in magnitude than mwp-IA and occurs at ~11 cal. kyr BP (Figure 1.4, Frame A). Although clearly visible in the Barbados sea-level reconstruction there is no evidence for this event in the other far-field sea-level

records at this time (e.g. Huon and Tahiti [23, 24]). There is also evidence from near-field sea-level records in Scotland that does not support the existence of this event [25]. The existence of mwp-IB, therefore, remains highly disputed. A rapid sea-level rise of between 10-15 m has also been observed in the Bonaparte sea-level record at ~19 cal. kyr BP [21] (Figure 1.4, Frame C). The existence of this has been disputed [26] and there is no clear evidence for such an event in either the Barbados or Sunda Shelf records. There is, however, further evidence for a rapid sea-level rise at this time from sediment records from the Irish Sea [27].

It is believed that rapid and large magnitude melting events such as mwp-IA, mwp-IB and the 19 cal. kyr event would have had major impacts on the climate system. For example, as discussed in Section 1.1, recent research has shown that a significant southern hemisphere source for mwp-IA may explain the onset of the Bølling-Allerød warm interval [3]. However, this result remains controversial given the current debate on whether the mwp-IA event was sourced primarily from the northern or southern hemispheres [4, 19, 28, 29].

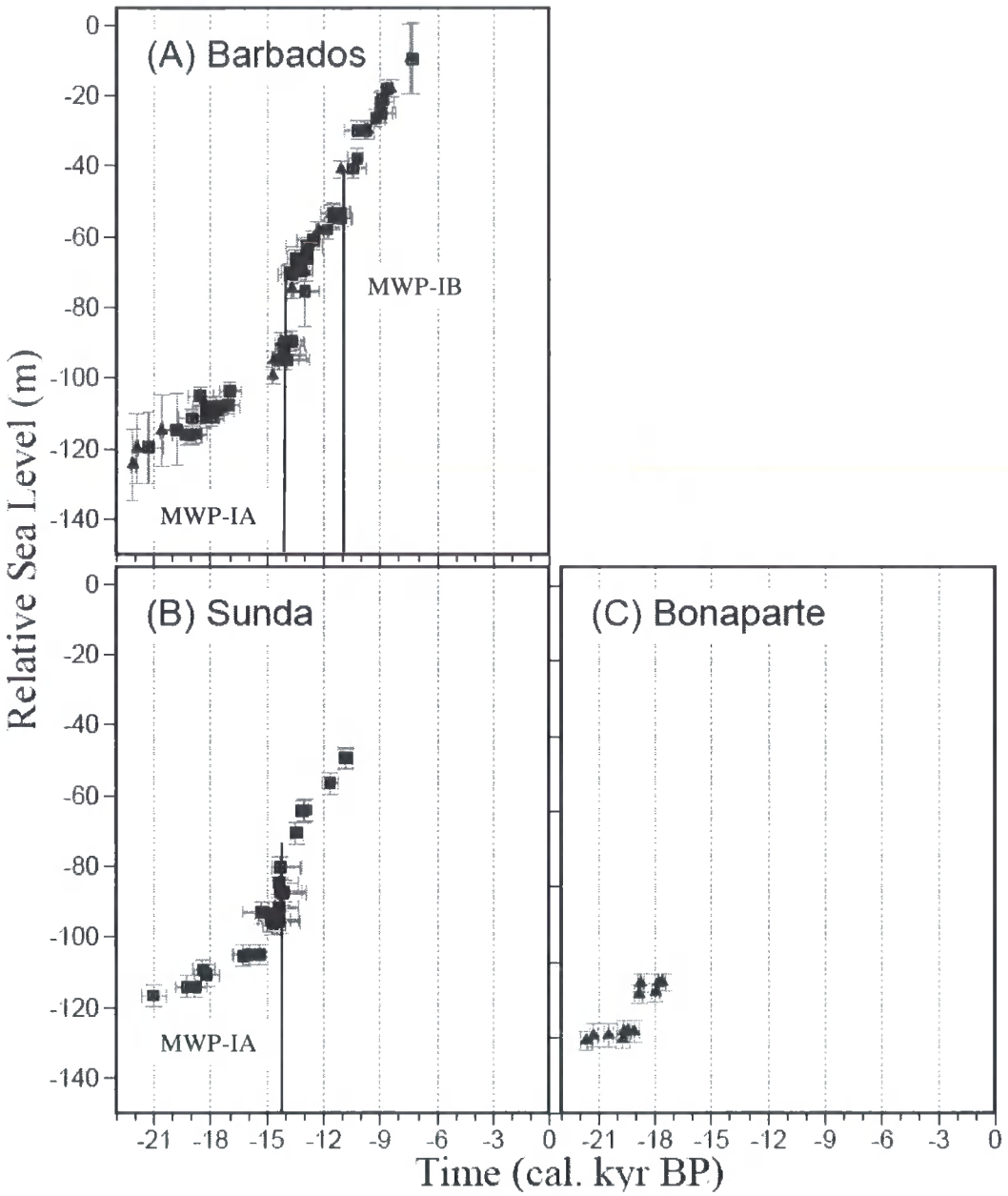

Figure 1.4: Sea level observations from three far-field locations triangles and squares represent U-Th and calibrated ^{14}C dated samples, respectively. Details on the data and errors are given in Sections 2.2 and 3.3.

The Fennoscandian and Barents ice sheets were unlikely to have made significant contributions to mwp-IA since the oxygen isotope record in the Norwegian and Greenland Seas show no single anomaly linked to a large freshwater input at this time. The Laurentide Ice Sheet has been generally viewed as the most

plausible contributor to mwp-IA due to its large volume. Furthermore, oxygen isotope records from the Gulf of Mexico and the Bermuda rise recording freshwater discharge from the southern Laurentide region contain an anomaly that is consistent with an increase in melting at the time of mwp-IA. However, several lines of evidence suggest this ice sheet was not the dominant source for the melt event [4]: (1) glaciological data indicate that melting the volume of ice contained in this southern Laurentide region corresponds to only ~2 m of sea-level; (2) geological fieldwork suggests no significant retreat of the southern component of the Laurentide ice sheet during mwp-IA; (3) geochemical records show no increase of freshwater flux through other major drainage basins such as the Gulf of Saint Lawrence and the Hudson Strait; (4) climate modelling results demonstrate that a freshwater influx of ~20 m into the Gulf of Mexico would produce a dramatic climatic cooling, through a disruption of the thermohaline circulation, which is not observed. The Antarctic ice sheet has also been proposed as a significant contributor to mwp-IA, mainly due to its relatively large marine based component, but there is no strong geomorphological or geochemical evidence to support this scenario.

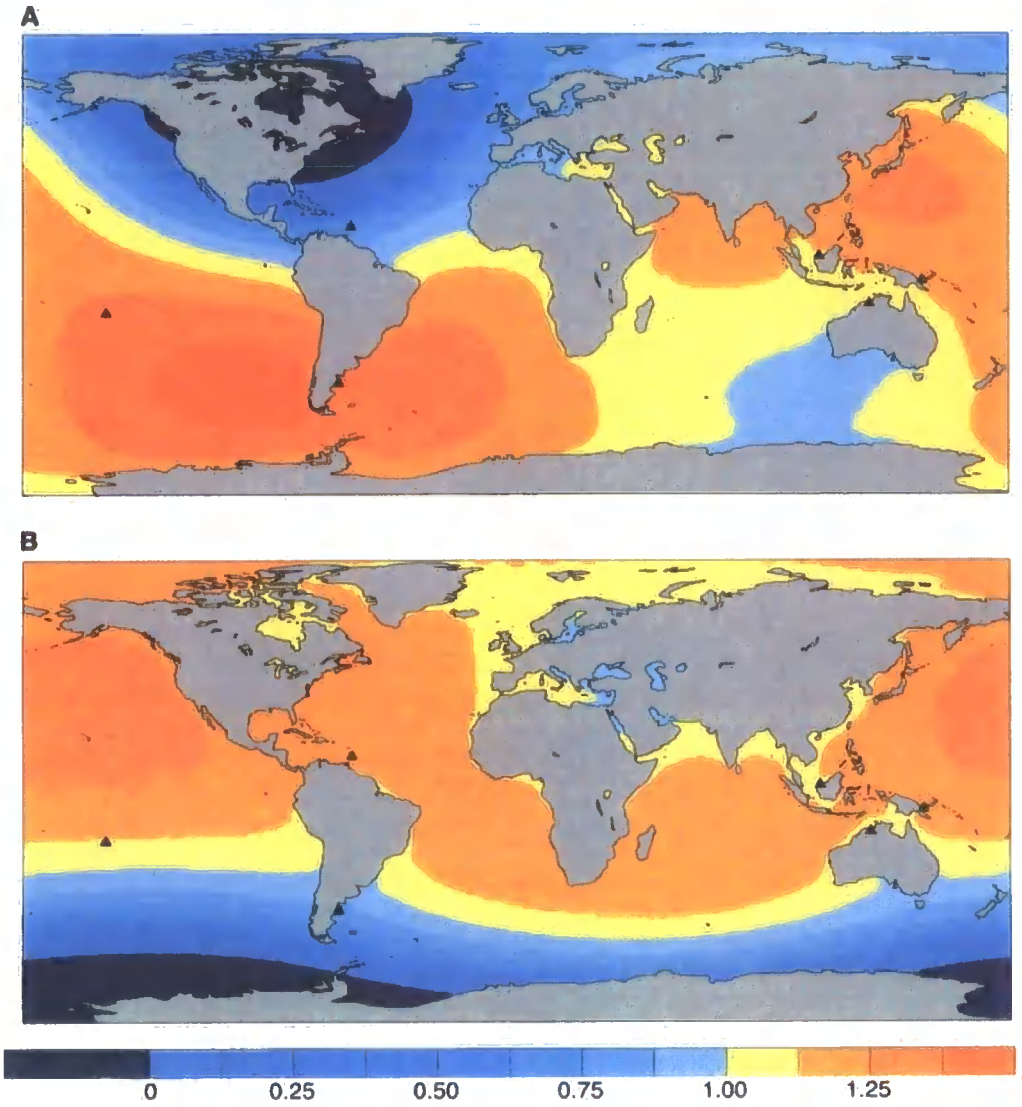

Figure 1.5: Normalised (dimensionless) sea-level change associated with melting from (A) the southern one-third of the Laurentide Ice Sheet and (B) West Antarctica, as they existed at the onset of the mwp-IA event. The predictions are normalised by the eustatic sea-level change; the colour scale refers to fractions of this change. The small triangles denote the locations of six far-field sites: (from left to right) Tahiti, Argentine Shelf, Barbados, Sunda Shelf, Bonaparte Gulf, and Huon Peninsula. From [28].

A recent study has argued that far-field sea-level observations spanning the short lived mwp-IA can be used to constrain the source geometry of this event [28]. The proposed method is based on the result that rapid melting of a specific ice reservoir produces a spatially distinct geographic pattern, or fingerprint, of sea-level change [30]. The spatial variation is dominated by the perturbation to the

geopotential and the elastic response of the solid Earth produced by the change in ice mass distribution. This approach is particularly robust since the predictions of rapid sea-level variation over short time intervals are independent of the viscosity structure of the Earth's mantle, which is not well constrained. A previous study, [28], used the observed sea-level rise associated with mwp-IA at Barbados and the Sunda Shelf to test a number of melt scenarios. For example, their results demonstrate that the data are not consistent with a sole Laurentide source for mwp-IA (Frame A, Figure 1.5); these data are, however, consistent with several other scenarios, including a significant Antarctic source (Frame B, Figure 1.5). In order to be consistent with the observations at Sunda and Barbados, these sites should both fall on or near the same contour i.e. exhibit a similar sized sea-level change. Due to the lack of far-field data that capture the magnitude of mwp-IA and the difficulty associated with accurately estimating the magnitude of the rise at these two sites, it has been argued that the observational error permits a sole northern hemisphere source scenario that is dominated by the Laurentide ice sheet [29] and so there remains considerable debate on this topic.

1.3 Outline of Thesis

The principal focus of this thesis is to investigate the meltwater pulses described above to determine what conclusions can be drawn about the source, magnitude and existence of these events. This is achieved by comparing sea-level predictions based on a number of different ice and earth models to both far and near field sea-level observations.

In Chapter 2 I focus on mwp-IA and consider the influence of melt source and

earth structure on the sea-level predictions at four far-field locations. The effect of varying the Antarctic contribution and the lower mantle viscosity structure is explored in detail in order to examine the influence of these parameters on the Lateglacial (13-10 cal. kyr BP) changes in predictions. The primary aim of Chapter 2 is to ascertain if the misfit to the far-field sea-level records observed in a number of previous studies [13, 29, 31, 32] can be reduced by considering a different ice/earth model combination.

In Chapter 3 I extend the work from Chapter 2 to consider the two smaller more controversial meltwater pulses at ~19 cal. kyr BP and ~11 cal. kyr BP (mwp-IB). I investigate the influence of including these events on the fit to the far-field sea-level records. The primary aims of Chapter 3 are to ascertain if there is any evidence in the sea-level records to support these events and to explore what constraints can be placed on their source geometry.

In Chapter 4 I return to the mwp-IA source problem by considering near-field sea-level records from the Antarctic coast. In particular, I adopt a high resolution, glaciological, ice model [33] for the Antarctic ice complex to determine if the near-field data can preclude the existence of a dominant Antarctic source for mwp-IA and if not go on to consider if any constraints can be placed on the deglaciation of the ice complex during mwp-IA.

Finally, in Chapter 5 the main points of Chapters 2 through 4 are summarised and the primary implications of the results are discussed in more detail.

1.4 Theory

In this section some key concepts related to predicting sea-level change that are used in the following chapters are discussed.

The sea-level model accounts for changes driven by the process of glacial isostatic adjustment (GIA). A number of previous publications have described the physical principles and computational techniques incorporated into GIA models of sea-level change (e.g. [17, 34-37]). Changes in sea-level associated with earth glaciation can be defined as [6],

$$S_G(\theta,\psi,t) = \frac{1}{g}\Phi(\theta,\psi,t) - R(\theta,\psi,t) + G^M(t) \qquad \text{Equation 1.1}$$

where $S_G(\theta,\psi,t)$ describes the sea-level change at a particular time, t, and location given by the co-latitude, θ, and east longitude, ψ. The functions $\Phi(\theta,\psi,t)$ and $R(\theta,\psi,t)$ are the perturbations to the geopotential and the solid surface produced as a result of surface ice and ocean mass redistribution and changes in the rotational potential associated with this mass redistribution [38]. The geopotential term is normalised by the surface gravitational acceleration, g, in order to convert the geopotential perturbation into a height shift of the ocean surface. The perturbation to the geopotential is commonly separated into changes produced directly by the surface ice-ocean mass redistribution and the changing rotational potential (the so-called "direct effect") and those produced indirectly by the solid earth deformation driven by the surface loading and rotational potential (the so-called "indirect effect").

The third term on the right-hand-side of Equation 1.1 describes a spatially uniform height shift of the geoid. This term is added to ensure the conservation of

surface ice/water mass within the cryosphere-hydrosphere system. There are a number of processes that contribute to this term ([6, 17, 35, 39]). For convenience of discussion in the following sections, we shall class these processes into two groups: eustatic and non-eustatic. The eustatic contribution can be written,

$$G^{M}_{EUST}(t) = -\frac{1}{\rho_W}\int_0^t \frac{\dot{M}_I(t)}{A_0(t)}dt \qquad \text{Equation 1.2}$$

in which $\dot{M}_I(t)$ is the rate of mass increase in grounded ice since the beginning of the loading event, ρ_W is the density of the water and $A_0(t)$ is the area of the ocean basins (which changes in time as sea levels rise and fall and marine based ice margins advance and retreat). The processes that contribute to the non-eustatic component are associated with GIA-induced vertical perturbations of the geoid and the ocean floor and the collapse of marine-based components of continental ice sheets, all of which affect the volume of the ocean basins through time.

The solid earth isostatic component of the sea-level signal is computed numerically using an impulse response formalism [40] which yields the response of a spherically symmetric, self-gravitating, and compressible Maxwell viscoelastic earth model to an impulse forcing. The radial elastic and density structure of the earth model is based on the seismically inferred PREM [41] and is depth parameterised into 25 km thick shells. The radial viscosity structure is more crudely parameterised into an upper region of effectively infinite viscosity to simulate an elastic lithosphere, and two deeper regions, each with a uniform viscosity, that correspond to the sub-lithospheric upper mantle and the lower mantle (below 670 km depth). These three parameters are varied in the modelling analysis.

Sea-level predictions are computed by solving the revised sea-level equation

described in [42, 43]. Recent advances in sea-level modelling, such as perturbations to the rotation vector, time-varying shorelines, and an accurate treatment of sea-level change in regions of ablating marine-based ice are, therefore, incorporated in the predictions described in following chapters.

Chapter 2 Far Field Sea-Level Modelling of Mwp-IA

2.1 Introduction

In this chapter the work of Clark et al. (2002) [28] is extended to consider the sea-level response both during and after the occurrence of mwp-IA. The motivation for this extension is two fold. First, the quantity of data that can be used to constrain model parameters is significantly expanded. Specifically, data from the Huon Peninsula and Tahiti in addition to those from Barbados and the Sunda Shelf are employed to examine the fit to the predicted sea-level response over the entire post-LGM period. Second, studies have shown that models tuned to fit the Barbados record produce a poor fit to the data from Huon, Tahiti and the Sunda Shelf during the Lateglacial period [13, 17, 31, 32, 44] (see Section 2.3.1). However, these studies assumed that the mwp-IA event was sourced primarily from the Laurentide ice sheet. The aim is to determine if this discrepancy can be reconciled by varying the source distribution of this major melt event. Since a substantial (~20 kyr) time window is considered, the predictions will also be sensitive to the adopted profile of mantle viscosity. Accordingly this profile is also treated as a set of free parameters in the modelling.

In Section 2.2 the various sea-level indicators that are used in the modelling analysis and the dating procedures and errors associated with these are discussed.

The sea-level equation utilised in this study has been previously described in Chapter 1. The key model inputs used to predict the sea-level signal at the far-field locations are described in Section 2.3. A number of different melt scenarios and earth models are introduced in Sections 2.3.1 and 2.3.5 and the performance of these models in simultaneously fitting sea-level constraints at the four far-field sites is assessed.

2.2 Observational Data

The sea-level data sets utilised cover different periods of time from the LGM to present with varying degrees of accuracy and precision. The model predictions are generated in calibrated kyr before present (cal. kyr BP) and so all the observations based on the Carbon-14 timescale have been calibrated using the CALIB 4.3 program with a 2-sigma range [45]. All data sets are corrected for the effect of localised tectonic activity using previously calculated uplift rates (see below). Finally, the depth used to mark a specific sea-level index point is a mean depth when taking into account the depth of formation of the particular sea-level indicator. The various data sets are described in detail below and illustrated in Figure 2.1.

2.2.1 Barbados

The Barbados coral data is one of the most complete records of sea-level change, with data covering the time period from the LGM to the early Holocene [20, 46-48]. This data set was collected from several closely spaced cores so, although the variability in sea level between coring sites can be considered to be negligible, the record may not represent a period of continuous reef growth.

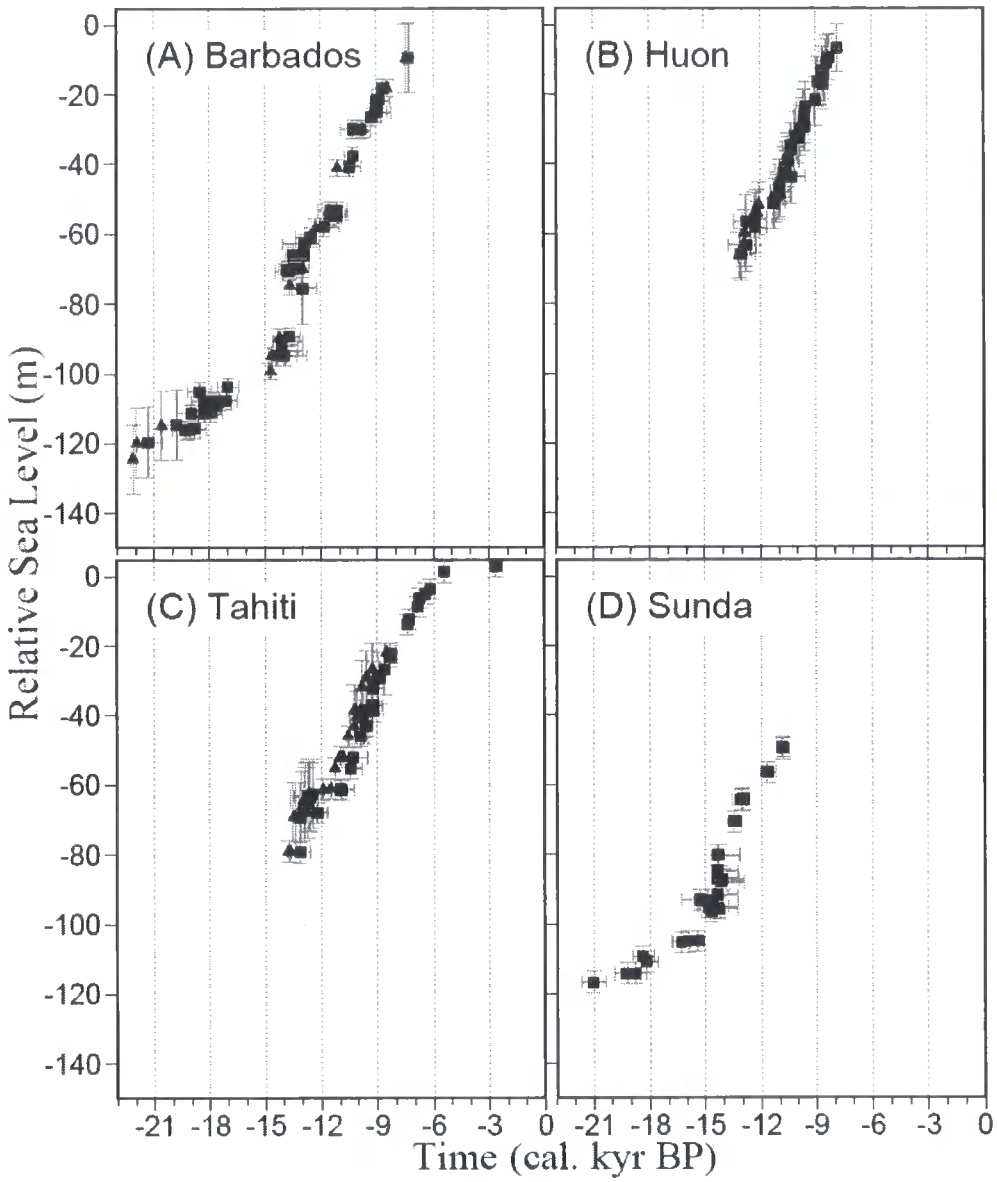

Figure 2.1: Sea-level observations at four sites based on the indicators described in detail in the text. The triangles represent U-Th dated samples and the squares are calibrated carbon samples.

The primary sea-level indicator at this location is the reef-crest coral *Acropora Palmata*. This species of coral is a reliable source of sea-level information due to its restricted depth of habitation (<~5m) and its resistance to post-depositional transport and compaction due to its rigid framework [49]. Mean sea level is therefore assumed to be at an altitude 2.5 m shallower than the recovery depth of a given coral sample, with an associated error of ± 2.5 m to match the range of possible habitation depth.

Some of the points in the Barbados record relate to the coral species *Porites Asteroides* which can live to depths of up to 20 m below the sea surface. For this species, sea level is, therefore, defined to be 10 m shallower than the recovery depth of a given coral sample, with an associated error of ±10 m. The Barbados sea-level data shown in Fig. 1 includes index points dated using both radiocarbon [20] and Uranium-Thorium [46-48] techniques.

Under the assumption that the uplift of the Barbados region occurred at a relatively constant rate since LGM, this rate can be calculated using the last interglacial reef position relative to present sea level. Observations of the height of the last interglacial reef relative to the core sites give a record of the overall uplift and a consequent average uplift rate of ~0.25 mm/yr [50]. The observations have been corrected for this rate to remove the effect of local tectonics.

The second, relatively rapid, sea-level rise evident in the Barbados data between 12 and 11 cal. kyr BP has been termed meltwater pulse IB (mwp-IB) [20]. There is no evidence for this event in other far-field records, however.

2.2.2 Sunda Shelf

This data set [22] is derived from a number of cores taken across the Sunda Shelf from offshore Vietnam to the Kalimantan region. Like the Barbados record, these data also provide a relatively long time series of sea-level change, covering the time interval from LGM to just before the Holocene.

Unlike the records at the other far-field sites considered in the analysis (Barbados, Huon and Tahiti), the sea-level indicators from the Sunda Shelf are wood fragments, macrofibres of mangrove and leached residues of bulk sediments.

Mangroves are known to be good sea-level indicators as present-day mangrove swamps exist only in the tidal range between mean sea-level and mean high water. In the region around Sunda Shelf the tidal range throughout the time period under consideration was less than ~2 m; therefore, sea levels based on mangrove macrofibres are defined to be at the same altitude as the recovery depth for the material with an associated error of ±3 m [51]. It is possible that some of the material dated and used to construct the sea-level data set shown in Figure 2.1D may not have been discovered in situ. This could have a significant impact on the accuracy of both the date and height information associated with certain samples.

All the samples have been dated using accelerator mass spectrometry radiocarbon techniques and the resulting ^{14}C dates were then calibrated to calendar years. The age errors plotted on the Sunda Shelf graph are those associated with the calibration programme only. The dating of the older samples in Figure 2.1D (age > 18 cal. kyr BP) was based on leached residue from the bulk sediment samples available at this depth. This bulk sediment analysis has a greater likelihood of suffering from contamination of more recent biological material and older reworked organic and inorganic substances. Dates obtained by applying the leaching process may also be less accurate because this process may not have removed the more mobile humic acids from the sample prior to dating [52-55]. Finally, age uncertainties might also be introduced due to riverine exports which would result in the samples being significantly younger than the ages given here [56].

The Sunda region is believed to have been tectonically stable from the time of the LGM to the present and therefore no corrections have been applied to the data for this effect. However, comparisons of the data to model predictions are complicated

by the fact that the core sites are distributed over a relatively large area. Figure 2.2 (inset) shows the locations where the cores were taken (solid grey and black circles) as well as contours of sea level predicted at 15 cal. kyr BP (based on the reference viscosity model and a dominant Laurentide source contribution to mwp-IA - see Section 2.3.1). These predictions show that there is a large spatial gradient in sea level and so it would be inaccurate to compare the entire data set to a prediction based at a single location [16].

The data set is split into two subsets, labelled 'A' and 'B'. The data from off-shore Vietnam are from two core locations, with a larger number of index points being derived from the more westerly located core. These data comprise the bulk of subset B (shown as solid black circles in Figure 2.2 (inset)). The black triangle represents the weighted mean position of these two cores (weighted to account for the number of index points derived from each core). The most southerly located core was also grouped into subset B since it is predicted to lie close to the sea-level values at location B. (This result was obtained regardless of the adopted ice and earth model.) Index points derived from these cores are shown as black squares on the main frame of Figure 2.2. These data can be compared to the dashed line in Figure 2.2 which is a prediction of sea-level change at the location 'B' (marked by a solid black triangle).

The weighted mean position of the cores comprising subset A (shown by solid grey circles) is also indicated by a black triangle. Data from these cores are shown by grey shaded squares on the main frame of Figure 2.2. These data can be compared to the solid black line, which represents a prediction of sea level at location A. In Section 2.3, all data-model comparisons for the Sunda region will be

separated into the two localities, A and B.

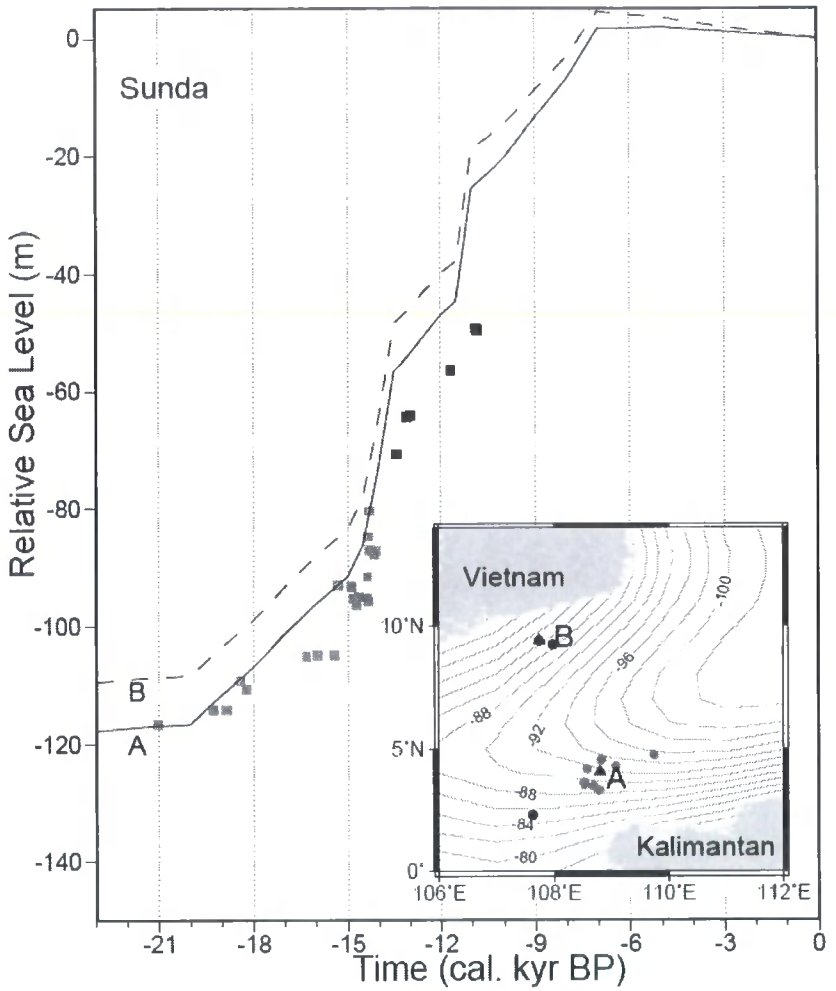

Figure 2.2: The inset map shows the locations of cores (solid grey and black circles) in the Sunda Shelf region from which sea-level index points in Figure 2.1E were derived. The contours on this map show a prediction of sea level at 15 cal. kyr BP based on the reference viscosity model and an ice model with a dominant Laurentide source contribution to mwp-IA (see Section 2.3.1 for details). The prediction shown in the inset illustrates that there is a large spatial gradient in sea level across the region and so comparing the data to a model prediction valid for a single location would result in a significant systematic error ([16]). For this reason, the core locations have been grouped into two subsets, A (grey circles) and B (black circles), and a mean location (indicated by black triangles) has been determined for each subset – see text for details. In the main frame, data derived from cores in subset A (grey squares) can be compared with the prediction for location A (solid line), whereas data derived from cores in subset B (black squares), can be compared with the prediction for location B (dashed line).

2.2.3 Huon Peninsula

The Huon Peninsula record is from a single core through a continuous coral reef framework on an emerged barrier [23]. Compared to the data from Barbados and the Sunda Shelf, the samples cover the relatively short period from ~13 cal. kyr BP to ~8 cal. kyr BP. The core comprised several coral species: *Porites*, *Acropora*, *Montipora*, *Pocillopora* and *Favia Goniopora*, with the dominant species at this site being *Porites*. The depth to which each of these species can survive at this location is not well known since they have been observed to live at a variety of depths in the current environment at Huon [23]. For this study, mean sea level is assumed to be 5 m shallower than the recovery depth of a given coral sample, and attach a relatively large error of ± 5 m to this value (following [16]). Both the Uranium series and Carbon-14 dates obtained from the corals at this location are utilised [57].

The Huon Peninsula is an area undergoing rapid uplift. The height of the last interglacial coral terrace above present sea level suggests an average uplift rate of 0.7 mm/yr in the northwest compared to 3.5 mm/yr uplift in the east. These values have been used to estimate an average uplift rate at the data site of 1.76 mm/yr [58]. There is also evidence to suggest that the rate at this location has varied through time, with values as high as ~2.16 mm/yr during the Holocene [59]. To partly account for the uncertainty associated with the average uplift rate in this region, an additional vertical uncertainty of ± 1.5 m to the observations is included.

2.2.4 Tahiti

The Tahiti data set is from two cores separated by 700 m [24]. The cores sample different coral species and cover the period from ~14 cal. kyr BP to ~3 cal.

kyr BP. The coral species used to determine sea-level variation at this site are *Acropora gr. robusta-danai, Pocillopora cf. verrucosa, domal Porites* and *Pocillopora* and tabular *Acropora* [60]. These species all exist within different depth ranges at present and tend to have significantly different growth forms depending on their growth depth (e.g. *Acropora*). The branching corals (e.g. *Acropora gr. robusta-danai* and *Pocillopora cf. verrucosa*) are assumed to grow at a relatively shallow depth of ~4 ± 2 m whereas the tabular forms (e.g. *Acropora*) and the domal varieties (e.g. Porites) tend to grow at ~10 ± 5 m and ~12 ± 8 m, respectively. These values have been adopted, in the same manner as for Barbados and Huon, to reconstruct the sea-level record for this location (see Figure 2.1). The different depth error bars evident in the Tahiti data set reflects the different habitation depth ranges of these coral species. Both Uranium-Thorium dates and, where these are unavailable, calibrated radiocarbon dates are adopted. Tahiti is expected to be undergoing slow subsidence due to the isostatic response to volcanic loading and hence a positive correction of 0.1 ± 0.05 mm/yr has been made to the data shown in Figure 2.1 [61].

2.3 Modelling

Sea-level predictions are computed by solving the revised sea-level equation described in Section 1.3. Recent advances in sea-level modelling, such as perturbations to the rotation vector, time-varying shorelines, and an accurate treatment of sea-level change in regions of ablating marine-based ice are therefore incorporated in the predictions described below. The two variable inputs to the sea-level algorithm are the earth and the ice history models.

The solid earth isostatic component of the sea-level signal is computed using

the impulse response formalism [40] which yields the response of a spherically symmetric, self gravitating and compressible Maxwell viscoelastic earth model to an impulse forcing. The radial elastic and density structure of the earth model is based on the seismically inferred PREM [41] and is depth parameterised into 25 km thick shells. The radial viscosity structure is more crudely parameterised into an upper region of effectively infinite viscosity to simulate an elastic lithosphere, and two deeper regions, each with a uniform viscosity, that correspond to the sub-lithospheric upper mantle and the lower mantle (below 670 km). These three parameters are varied in the modelling analysis. It is convenient to define a preferred, or reference, viscosity model. For this purpose a 96 km thick elastic lithosphere and viscosities of 0.5×10^{21} Pa s for the upper mantle and 10^{22} Pa s for the lower mantle region was chosen. These parameters are broadly consistent with the results of a number of recent viscosity inferences (e.g. [10, 11, 59, 62-66]).

The initial ice model utilised in this study was derived by revising the ICE-3G deglaciation history [14] to include a chronology based on the calibrated carbon scale as recorded by Bard et al. (1990) [47] and a glaciation phase. The glaciation phase consists of the same ice increments as the deglaciation phase, reversed in sign and extended over time so that the loading episodes occur every 7 cal. kyr (compared to every 1 cal. kyr during deglaciation). Glaciation begins at 123 cal. kyr BP, at which time the ice extent is assumed to be the same as at present. Maximum ice extent (LGM) occurs between 25 and 20 cal. kyr BP. The deglaciation model was also interpolated to include ice geometries at 0.5 cal. kyr intervals during mwp-IA (at 14.5 and 13.5 cal. kyr BP) and mwp-IB (at 11.5 cal. kyr BP), so that these rapid events are better captured by the model.

2.3.1 Sensitivity of Predictions to Source of Mwp-IA

The Barbados sea-level record [20, 47] was chosen as the 'reference data set' since it is based on a relatively consistent set of sea-level indicators (the coral species *Acropora palmata*) from a single locality and it provides the most complete temporal record of relative sea level change at any far-field site. Since the ice model will be tuned to fit the Barbados data, the quality of fit at the remaining three sites provides a measure of the success of a specific model run.

Sea-level predictions based on the initial ice model and the reference earth model do not provide a good fit to the Barbados record. In particular, the net rise from the LGM to present is under-predicted by ~15 m and there is no rapid rise at the time of mwp-IA. In order to produce a good fit to these data the Laurentide component of the ice model only is altered. In particular, the total volume is increased by ~30% (equivalent to ~15 m eustatic sea-level rise) and the timing of melt is adjusted until a reasonable fit to the Barbados data was achieved. The tuning method used was relatively crude since the thickness of the entire ice sheet is simply scaled; however, this approach is adequate for the present study since there is modelling of far-field data only, and these are not particularly sensitive to the spatial details within individual ice sheets.

Increasing the total volume of the Laurentide ice sheet by ~30% may seem unrealistic; however, this scaling is consistent with recent modelling and observational results. A large suite of glaciological simulations of North American ice extent produced a range of LGM volumes equivalent to 69 to 94 m of eustatic sea-level rise [67]. The scaled version of the Laurentide ice sheet represents ~65 m of eustatic sea-level rise, which fits into this range when the contributions of the

Inuitian and Cordilleran ice sheets are considered. Note, however, that the pre-scaled version of the Laurentide ice sheet (equivalent to about 50 m eustatic sea-level rise) is not consistent with these glaciological results. Furthermore, observations of changes in the gravity field in central Canada suggest a significant increase in ice volume over this region [13].

2.3.2 Increasing the Antarctic Contribution to Mwp-IA

The sensitivity of the predictions to the source of mwp-IA is explored first. The optimum model fit assuming a dominant Laurentide source for mwp-IA is shown as the black line in Figure 2.3. This scenario assumes no contribution to mwp-IA from the Antarctic ice sheet but includes minor contributions from other reservoirs (specifically, ~26 m from Laurentide and ~2 m from sources other than Laurentide). At Huon, Tahiti and Sunda Shelf this model is shown to result in predicted sea levels that are significantly too high following mwp-IA. This first order misfit has been noted in recent work (e.g. [13, 17, 32, 44]) but no attempt has been made to explore this discrepancy by varying the input model parameters.

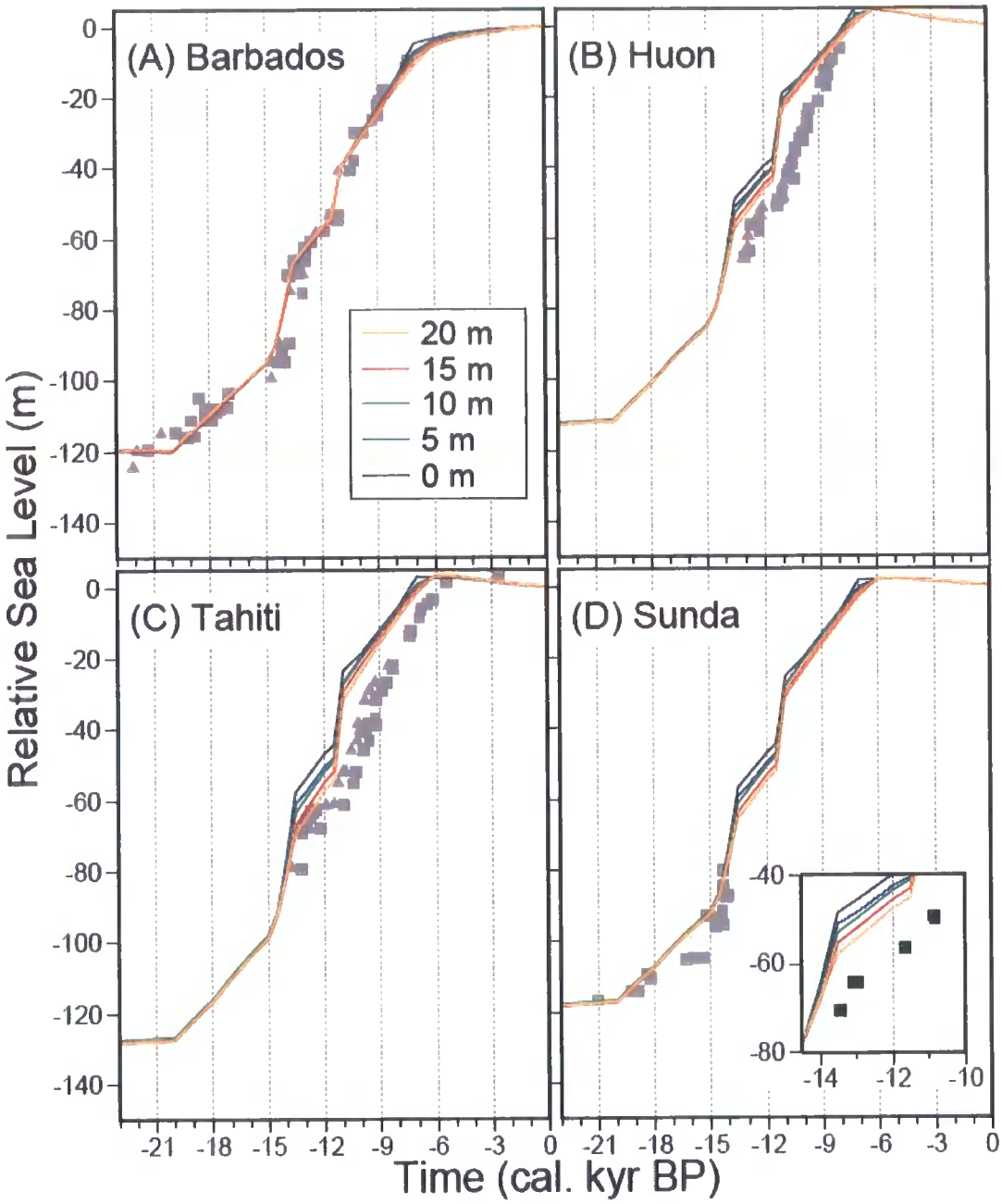

Figure 2.3: Sea-level predictions based on the reference earth model and a range of melt scenarios to illustrate the sensitivity to changes in the relative contributions of the Laurentide and Antarctic ice sheets to mwp-IA. The key in Frame A identifies the contribution, in eustatic sea level, from the Antarctic ice sheet for each model run. Each model was tuned to fit the Barbados record and so the success of each melt scenario can be gauged by the quality of the fit at the three southern hemisphere sites (Frames B to D). The inset in Frame D shows the fit of the model predictions to the data from location B shown in Figure 2.2. The triangles and squares indicate the sea-level observations described in the text and shown in Figure 2.1. Note that data error bars are not shown to improve the clarity of the figure.

Figure 2.3 shows the effect of progressively increasing the Antarctic component of mwp-IA on the sea-level signal predicted at these four sites. In order to examine the effect of an increasing contribution from Antarctica, the eustatic contribution from this ice sheet was increased in 5 m increments from 0 m to 20 m (Figure 2.3). Note that the net contribution from the Laurentide ice sheet to mwp-IA was systematically reduced in this process to ensure that the model remained faithful to the Barbados record. In the original ICE-3G model the Antarctic ice sheet does not begin to melt until 11 cal. kyr BP and produces a relatively uniform sea-level rise from 11 to 5 cal. kyr BP. In order to introduce a contribution to mwp-IA, the beginning of the Antarctic deglaciation phase is brought forward to 14.5 cal. kyr BP. In contrast to the adjustments to the Laurentide ice sheet, the total volume of ice melt from the Antarctic ice sheet was not increased in this suite of predictions since recent estimates put the volume of ice contained in this ice sheet at the LGM compared to present in the range ~10-20 m (e.g. [33, 68]). (The Antarctic component in the ICE-3G model already exceeds the upper limit of this range by ~8 m.). Consequently, the larger the contribution of the Antarctic component to mwp-IA, the less this ice sheet is assumed to contribute to eustatic sea level following mwp-IA.

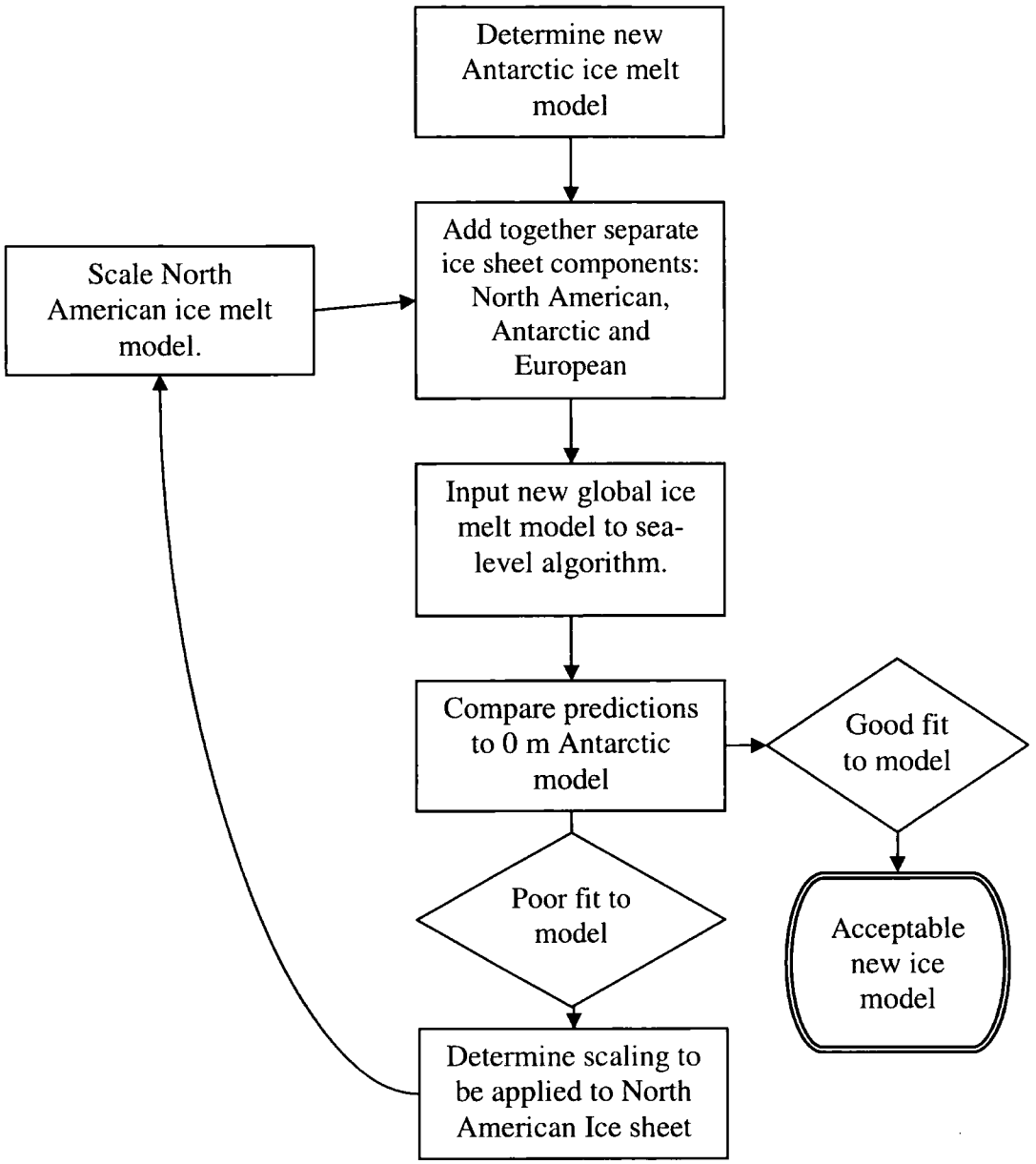

Figure 2.4: Flow chart to illustrate the scaling process employed to fit the models to the Barbados sea-level record.

In order to tune the predictions to the Barbados record an iterative procedure was used to scale the North American ice sheet. To fit the Barbados record the total sea-level rise from LGM to present day and the sea-level change increments must be kept the same in the new model as in the original model. When increasing the Antarctic component to mwp-IA the total eustatic signal from Antarctica is altered in order to provide the required sea-level rise across the pulse (e.g. 0, 5 10, 15, 20 m),

once this has been obtained the contribution from the Antarctic ice complex is assumed to be linear from the end of the pulse (13.5 cal. kyr BP) to 5 cal. kyr BP. Once the new Antarctic component has been added to the North American and European components the new model is compared to the original model fit to Barbados. First the new model LGM is tested against the LGM of the reference model, if necessary the North American ice sheet is scaled up or down at LGM to compensate for any differences in sea-level rise from LGM to present. Once the LGM value of the new model is the same as the original model the difference in sea-level at each time step (0.5 or 1 kyr intervals) in the new model is compared to the original (0 m Antarctic model). For the purpose of determining an initial scaling factor to apply to the North American ice change file the relationship between sea-level and ice change was assumed to be linear. This scaling is applied and the new rate of ice change is calculated. The model is then re-run to produce new predictions. This process is repeated until the sea-level change in each Barbados prediction is approximately the same. This scaling is applied only to the first part of the record, after 11 cal. kyr BP to cessation of North American ice melt a linear change is used. This scaling process is illustrated in Figure 2.4.

It is evident from inspection of Figure 2.3 that increasing the Antarctic contribution lowers the predicted post-mwp-IA sea-level signal at Huon, Tahiti and Sunda and therefore significantly improves the quality of the fit. A 15 m Antarctic contribution is adopted as optimal in terms of improving the fit to the far-field data (giving some consideration to the suggested limited volume available from this ice sheet). In the following discussion, the focus is, thus, on scenarios in which the Antarctic ice sheet contributes either 0 m or 15 m to mwp-IA (the black and red lines

in Figure 2.3 respectively).

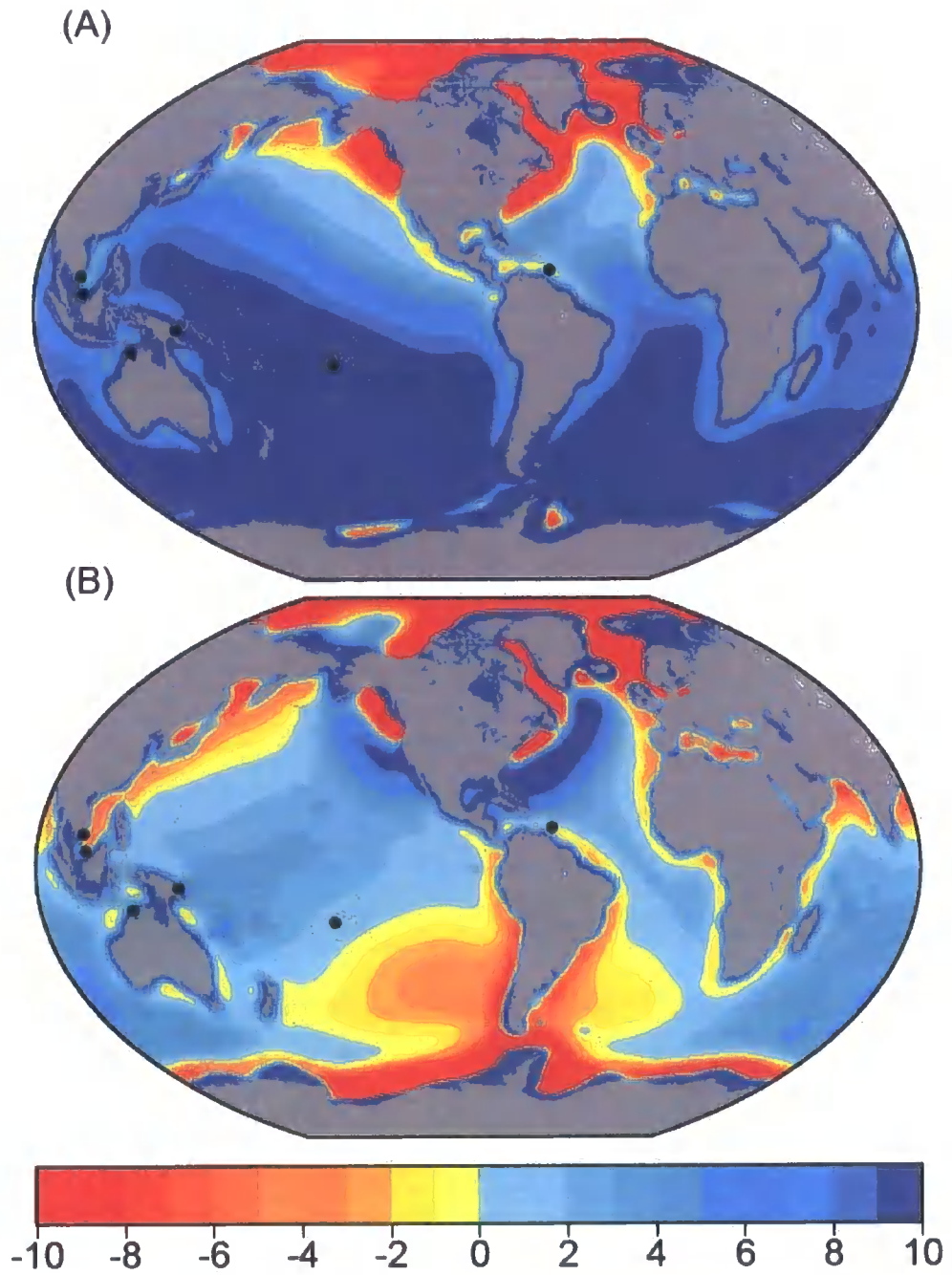

Figure 2.5: Predicted sea-level change, in metres, over the past 13 cal. kyr relative to the predicted change at Barbados (i.e., predictions of the raw sea-level change across this time interval are shifted by the specific prediction at Barbados, and thus the Barbados prediction falls on the zero contour in each panel). (A) The scenario in which North American ice is the sole source for the mwp-IA event (as in the black line in Figure 2.3; $\upsilon_{LM} = 1 \times 10^{22}$ Pa s). (B) The scenario for assuming that the Antarctic ice sheet contributes an equivalent eustatic sea-level rise of 15 m to the event (as in the prediction shown by the red line in Figure 2.3).

The improvement in fit is due to a number of factors which are discussed in more detail below. Maps of the predicted sea-level change over the past 13 cal. kyr (i.e., relative sea-level change since Lateglacial time) for the scenarios in which the Antarctic ice complex contributes either 0 or 15 m to mwp-IA (Figure 2.5) indicate a significant change in the geometry of the associated GIA effects. Each map is plotted relative to the prediction at Barbados. The observed relative sea-level of markers of age ~13 cal. kyr BP at Barbados, Tahiti, Huon Peninsula, and Sunda Shelf are all at a depth of ~60 m (Figure 2.1 and Figure 2.3). In the scenario where Antarctic mass flux dominates the mwp-IA event (Figure 2.5B), the predicted zero contour passes close to each of these sites and thus the 13 cal. kyr BP sea-level markers are fit more closely by this scenario. In contrast, the dominant North American source for mwp-IA yields significantly more discrepant predictions at these four sites (Figure 2.5).

2.3.3 Exploring other Source Scenarios

The analysis by Clark et al. [28] highlighted several possible mwp-IA scenarios which would be consistent with the relative size of the sea-level jump observed in the Barbados and Sunda Shelf records. The following freshwater sources were consistent with the study by Clark et al. [28]: the Barents Sea plus Fennoscandian ice complexes, and melting distributed over all ice sheets in the ICE-3G deglaciation model [14] (All-ICE3G), the entire Antarctic ice complex, or either the east or west portions. As discussed in the introduction there are independent constraints (e.g. oxygen isotope records [4]) which suggest that the Barents and Fennoscandian model is unlikely. Other models which performed less well in the study by Clark et al. [28] included the "North-ICE-3G" model which has similar contributions to mwp-IA as

those in the ICE-5G model of Peltier [69].

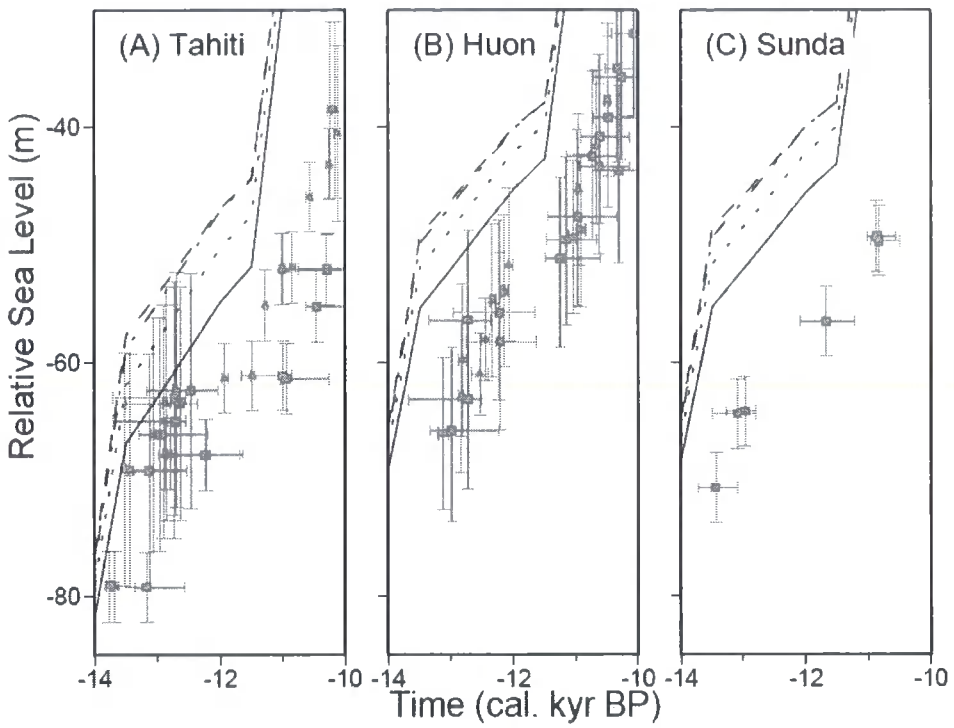

Figure 2.6: Sea-level predictions for Tahiti, Huon Peninsula and Sunda Shelf within the Lateglacial time window for four different source scenarios for the mwp-IA event. The solid and dashed lines represent the 0 m and 15 m contributions form the Antarctic ice complex (in units of equivalent eustatic sea-level rise) considered in Figure 2.3 and Figure 2.5. The dotted line shows the prediction for a global melt source distribution based on the All-ICE3G model of Clark et al. [28]; in this case the relative contributions to mwp-IA from North American, Antarctic and European ice sheets are 16, 5 and 5 m (eustatic). The dashed-dotted line shows the prediction for a northern hemisphere source distribution based on the model proposed by Peltier [69]; in this case the relative contributions from North American and European ice sheets are 22 and 5 m (eustatic), respectively.

In Figure 2.6 two of these additional mwp-IA source scenarios are considered: a global distribution of sources based on the "All-ICE-3G" scenario described in [28] and a northern hemisphere source distribution based on the "North-ICE-3G" scenario described in [28] and [69]. The northern hemisphere model produces a fit very similar to that generated for the case of a dominant North American source. In comparison, the global source model provides an improved fit but there remain

systematic discrepancies at Huon, Tahiti and Sunda Shelf which are improved when a larger (15 m) Antarctic source is considered.

2.3.4 Understanding the Results

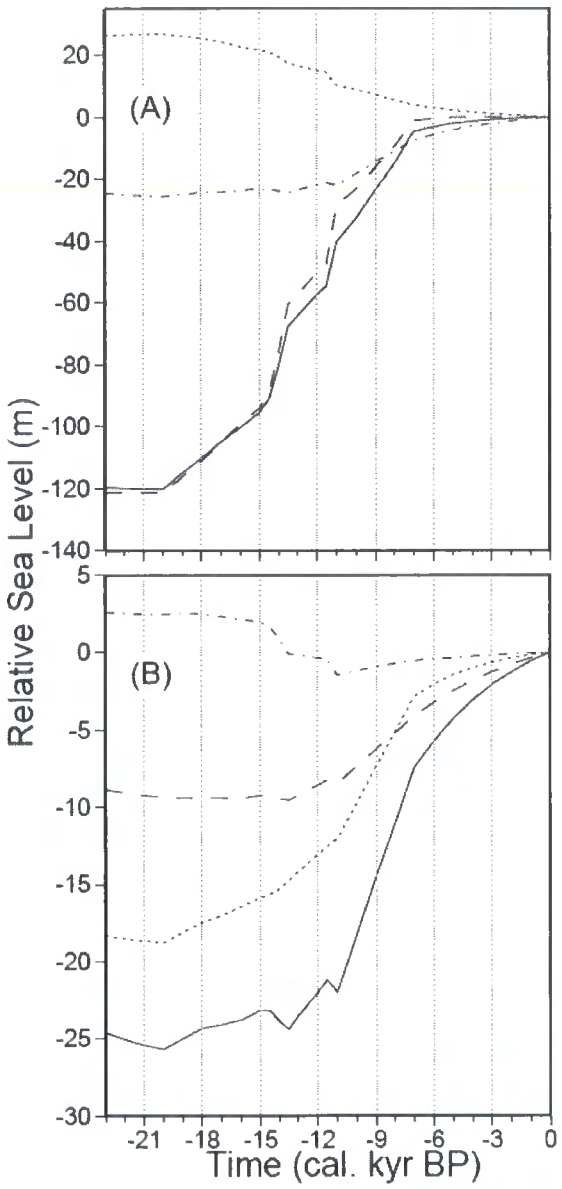

Figure 2.7: (A) The total sea-level prediction at Barbados for a model run in which a 0 m contribution to mwp-IA from Antarctica (solid line) is assumed. The dashed, dotted and dashed-dotted lines show the contributions from, respectively, the eustatic and non-eustatic spatially uniform and the spatially varying sea-level signal (see text for details). (B) The spatially varying signal at Barbados (solid line) split into components associated with ice-(dotted), ocean-(dashed) and rotation-induced (dot-dashed) perturbations to sea level.

There are a number of processes that contribute to an improved fit to the far-field data set when an Antarctic source is assumed. To illustrate these, the predicted RSL signal is separated into contributions that are spatially varying (first two terms in Equation 1.1) and spatially uniform (third term in Equation 1.1). In Figure 2.7A, the predicted signal at Barbados for the model that assumes a dominant Laurentide contribution to mwp-IA is decomposed. The total sea-level signal (solid line) is comprised of a site dependent component (dash-dotted line) and a spatially uniform component (sum of dashed and dotted lines). Both the eustatic (dashed) and non-eustatic (dotted) spatially uniform components are shown. The spatially varying signal can also be separated into components associated with the three GIA forcings: ice loading, ocean loading and the perturbations to the rotational potential [37]. This decomposition is illustrated in Figure 2.7B.

The spatially uniform, non-eustatic fall in sea level since the LGM (dotted line, Frame A) is driven, mainly, by equatorial ocean siphoning [35, 39] and the retreat of marine-based ice [37, 70]. Note that this signal is similar in magnitude but opposite in sign to the spatially variable component of the signal (dash-dotted line, Figure 2.7A). As a consequence, the total signal (solid line) never deviates more than ~10 m from the eustatic curve at this site. This result is, of course, sensitive to the input ice and earth model. Figure 2.7B illustrates that the spatially variable sea-level signal at Barbados is dominated by the ice loading (dotted line). This ice-induced signal is largely due to the peripheral bulge subsidence associated with ablating North American ice. The ocean-induced signal (dashed line) produces a rise of ~10 m due, mainly, to the response of the solid Earth to the addition of ~120 m of water at this location. The rotation-induced signal (dash-dotted line) has the smallest

magnitude and contributes a more complex sea-level fall from the LGM to the Late Glacial followed by a sea-level rise during the Holocene [38].

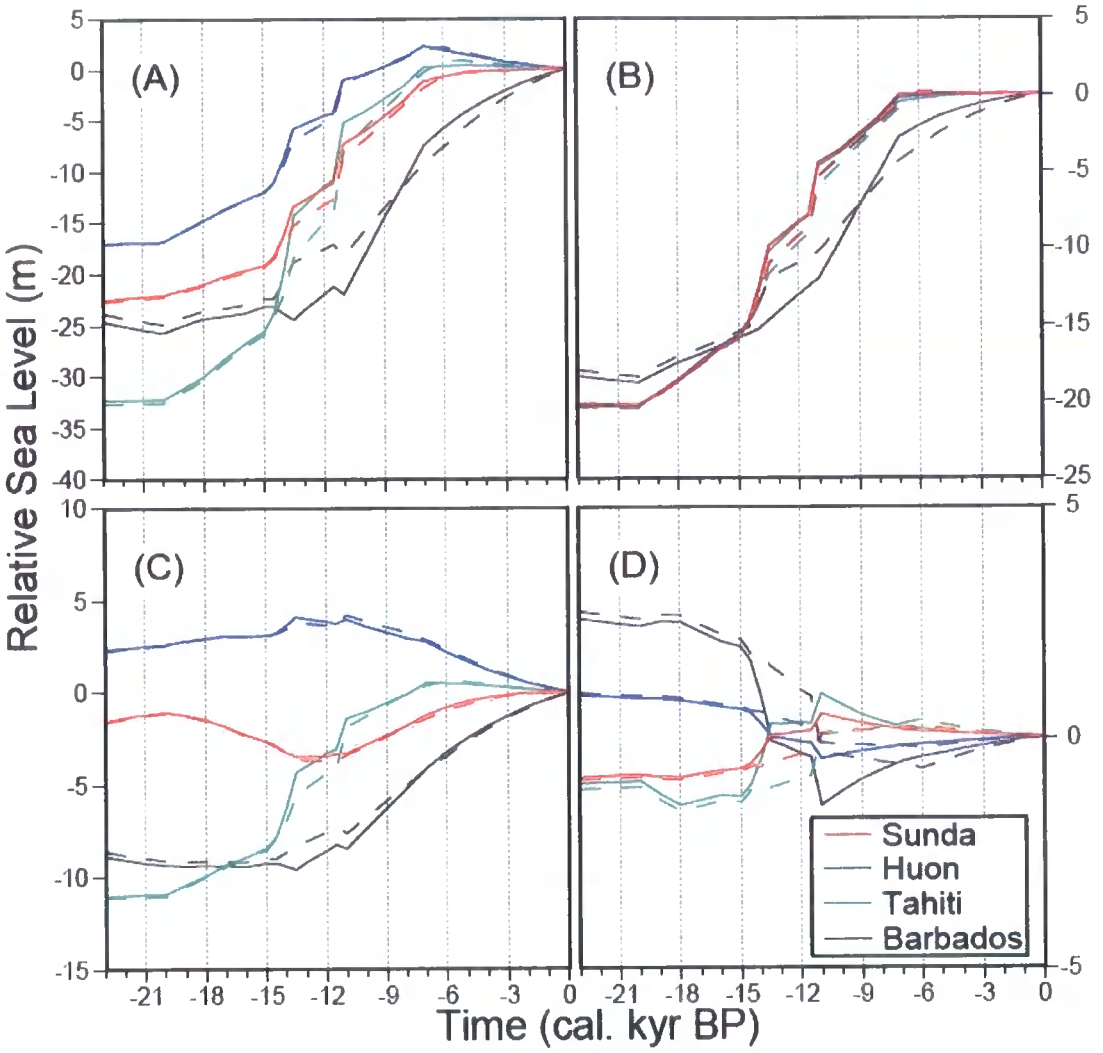

Figure 2.8: (A) The spatially varying components of the sea-level signal at all four far-field sites (see key Frame D) for 0 m eustatic (solid) and 15 m eustatic (dashed) contributions to mwp-IA from Antarctica. Frames (B) to (D) show the contributions to the signals in (A) from ice- (B), ocean- (C), and rotation-induced (D) GIA forcings. The predictions for the Sunda Shelf are calculated for location A shown in Figure 2.2.

Differences in the spatially varying signal between the four far-field sites will govern how well a specific model can simultaneously fit the observations. In particular, the data require a model that significantly reduces the predicted sea-level rise across mwp-IA at Sunda, Tahiti and Huon relative to Barbados. Figure 2.8A

shows the spatially varying signal at all four sites for the case of a dominant Laurentide source (solid lines) and a dominant (15 m eustatic) Antarctic source (dashed lines). The contribution of the ice-, ocean- and rotation-induced signals to the predictions in Figure 2.8A are shown in Figure 2.8(B-D), respectively.

The predictions based on a dominant Laurentide source in Figure 2.8A (solid lines) illustrate why this model does not produce a good fit at all four sites. The predictions for Sunda, Huon and Tahiti all show a rapid and large magnitude rise across both mwp-IA and mwp-IB. In contrast, at Barbados, the signal over the time window 14.5 – 11 cal. kyr BP shows a relatively small net rise with a small magnitude *fall* in sea level across mwp-IA and mwp-IB. The largest sea-level rise at Barbados occurs between 11 cal. kyr BP and the present, during which time the signal at the other sites is much less pronounced. This spatial difference in the signals results in the predictions for Sunda, Tahiti and Huon becoming too shallow too early.

Inspection of the results in Frames B-D shows that the spatial variation described above is dominated by the ice- and ocean- induced signals. The ice-induced signal at Barbados (solid line, Figure 2.8B) is anomalous compared to the analogous prediction at the other three sites. The three southern hemisphere (Sunda, Huon, and Tahiti) sites show a sharp sea-level rise at the times of mwp-IA and mwp-IB, whereas this is not the case at Barbados. This difference relates to the geometry (or fingerprint) of sea-level change in response to a rapidly ablating ice reservoir. As discussed by Clark et al. [28], this shows a sea-level fall in the immediate vicinity of the ice mass and an increasing sea-level rise with distance from the ice sheet beyond this region. The principal cause of this variation is the direct gravitational effect of

the ablating ice sheet as well as the uplift of the solid surface in the near-field of ablation.

The solid lines in Figure 2.8A are computed under the assumption that the Laurentide ice sheet is the primary source for mwp-IA and mwp-IB. In this case, Barbados is significantly closer to the source than the other three sites and so the spatially varying component of the sea-level change is distinctly different at this site compared to the three sites located in the southern hemisphere. The ice-induced signal at Barbados (Figure 2.8B, solid line) shows no sign of either mwp-IB or mwp-IA due to the sea-level fall associated with the direct gravitational effect being cancelled by a rise produced by rapid subsidence of the solid surface in the Barbados region.

The spatial variations associated with the ocean-induced signals are related to the contrasting coastline geometry at the different sites. For example, Tahiti is an island surrounded by ocean and so is particularly sensitive to the local sea-level change and the corresponding ocean loading. In contrast, the Sunda Shelf was exposed continental shelf for a significant portion of the deglaciation period and so the net impact of sea-level change in terms of local ocean loading is relatively small.

The rotation-induced signal, although smaller in magnitude than the other two, contributes to the spatial variation shown in Figure 2.8A. This contribution is associated with the position of each site with respect to the four-quadrant "beach ball" pattern associated with this signal (e.g. [38]).

The analogous results for a dominant contribution (15 m eustatic) to mwp-IA from the Antarctic ice sheet are now considered. The dashed lines in Figure 2.8 show the total spatially varying signal (Figure 2.8A) and the respective contributions

to this signal from the three GIA forcings (Figure 2.8B-D) for this case. The results in Figure 2.8A illustrate why the data prefer a dominant Antarctic source. At all southern hemisphere sites, the effect of increasing the Antarctic contribution is to moderately reduce the size of the sea-level rise across mwp-IA. In contrast, the spatially varying component of sea-level change at Barbados is significantly increased from a fall to a rise across mwp-IA for this scenario. This difference originates primarily from the ice–induced sea-level fingerprint described above. Barbados is the most significantly affected due to its relatively close proximity to the Laurentide ice sheet.

The ice-induced signal at Barbados shows a clear sea-level rise across mwp-IA for the Antarctic dominant scenario (Figure 2.8B) since the direct and deformational effects do not cancel out in this case. In contrast the change in the ocean-induced signal is less dramatic for the two mwp-IA source scenarios (Figure 2.8C). The gradient in the rotation-induced signal across mwp-IA is significantly reduced when a dominant Antarctic source is adopted. This is because high-latitude ice mass changes do not efficiently excite wander of the rotation pole (e.g. [71]).

2.3.5 Sensitivity of Predictions to Earth Model Viscosity Structure

In the following, the results of the previous section are extended to consider the influence of changing the mantle viscosity structure on sea-level predictions for the two mwp-IA scenarios: a dominant Laurentide source (with no contribution from the Antarctic) and a dominant Antarctic source (a contribution equivalent to 15 m eustatic sea-level rise). For each earth viscosity model considered, the North

American ice history was scaled to maintain an accurate fit to the Barbados sea-level history. The following parameter ranges are considered: lithospheric thickness (71 – 120 km), upper mantle viscosity (1 – 10 × 10^{20} Pa s) and lower mantle viscosity (1 – 50 × 10^{21} Pa s).

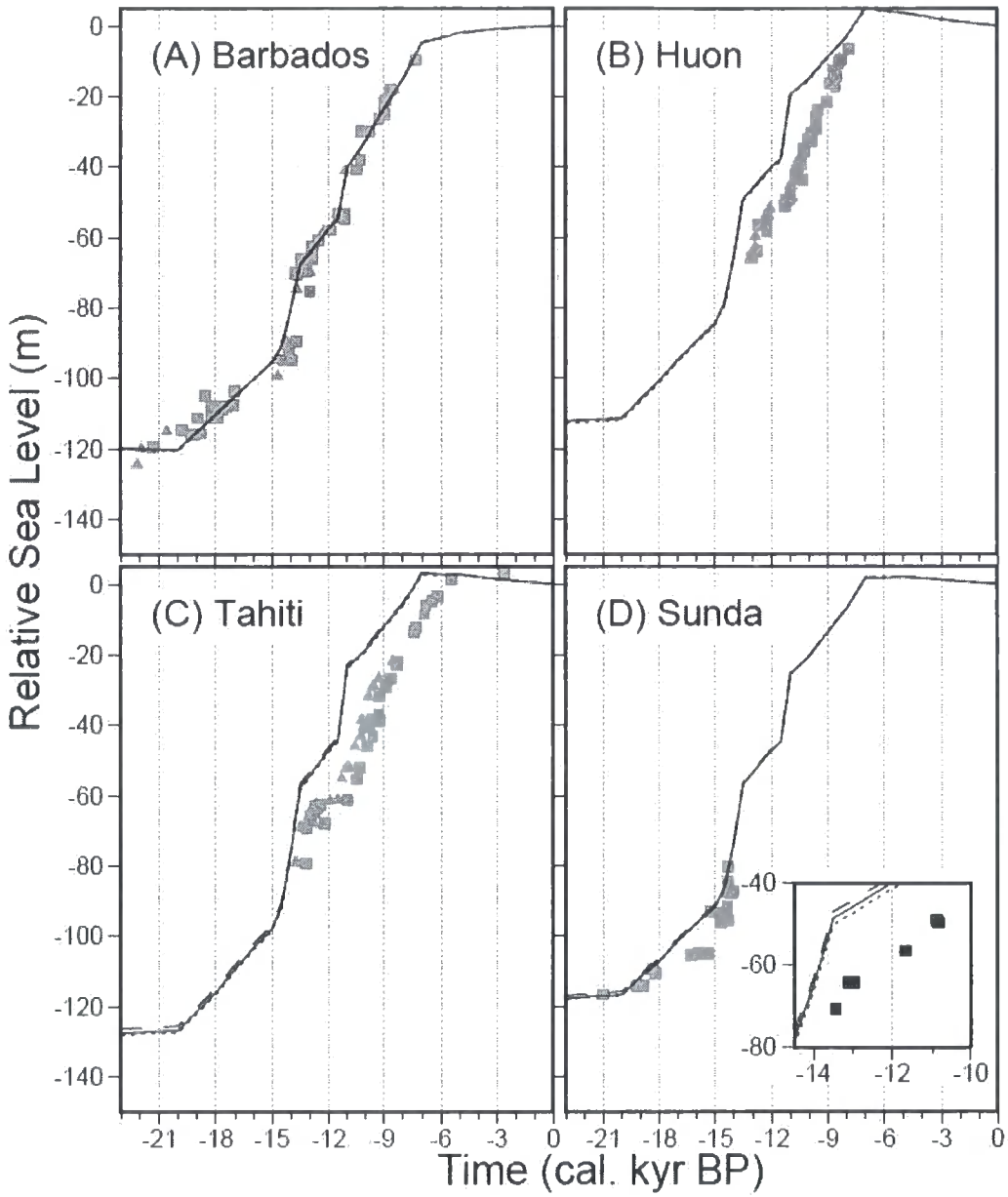

Figure 2.9: Sea-level predictions based on a dominant Laurentide contribution (0 m eustatic contribution from Antarctica) to mwp-IA for the reference earth model (solid line) and two other earth models that are the same as the reference model except that the lithospheric thickness is reduced to 71 km (dashed) or increased to 120 km (dotted). The inset in Frame D shows the fit of the model predictions to the data from location B shown in Figure 2.2.

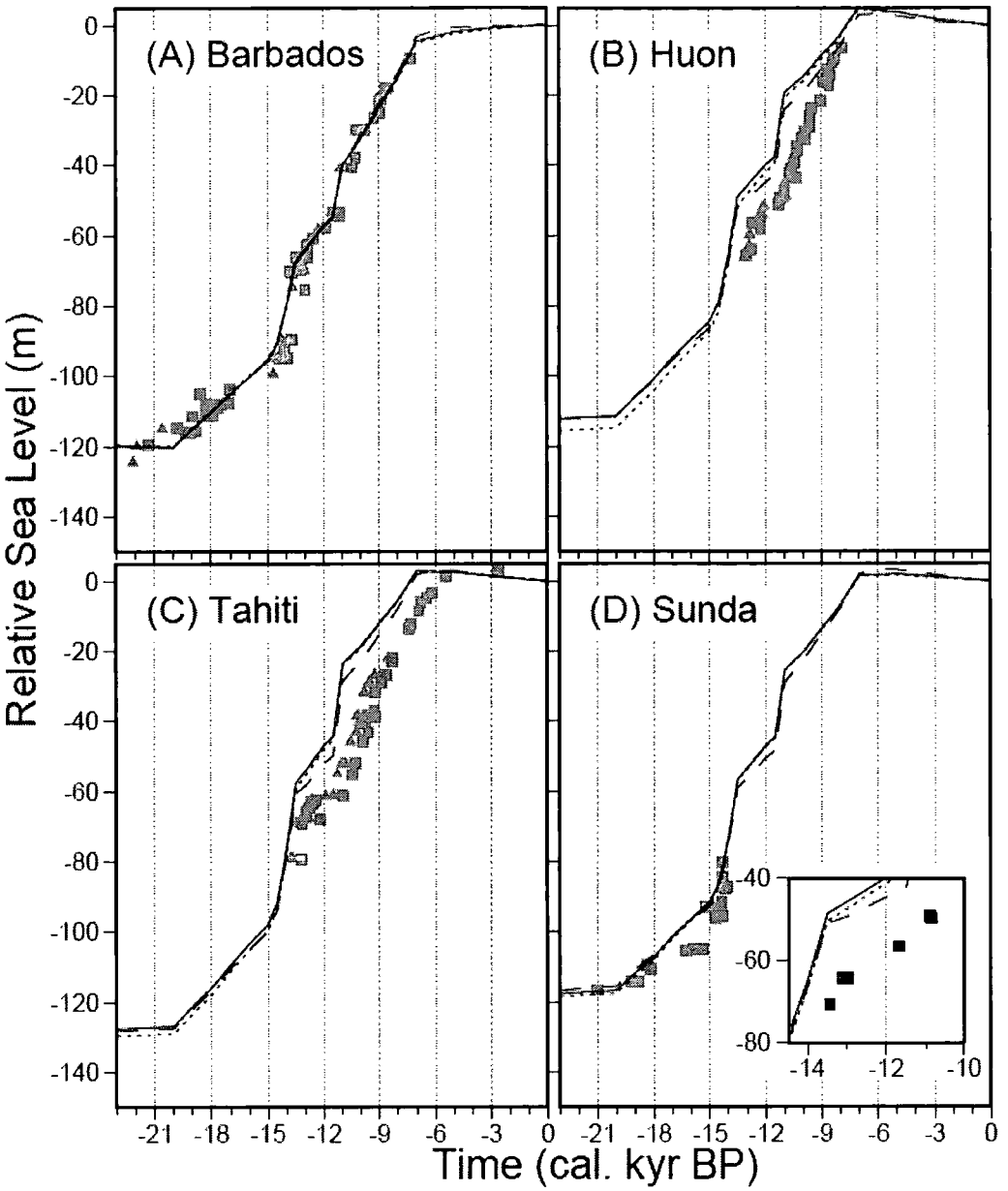

Figure 2.10: Sea-level predictions based on a dominant Laurentide contribution (0 m eustatic contribution from Antarctica) to mwp-IA for the reference earth model (solid line) and two other earth models that are the same as the reference model except that the upper mantle viscosity is reduced to 1 x 10^{20} Pa s (dashed) or increased to 10 x 10^{20} Pa s (dotted). The inset in Frame D shows the fit of the model predictions to the data from location B shown in Figure 2.2.

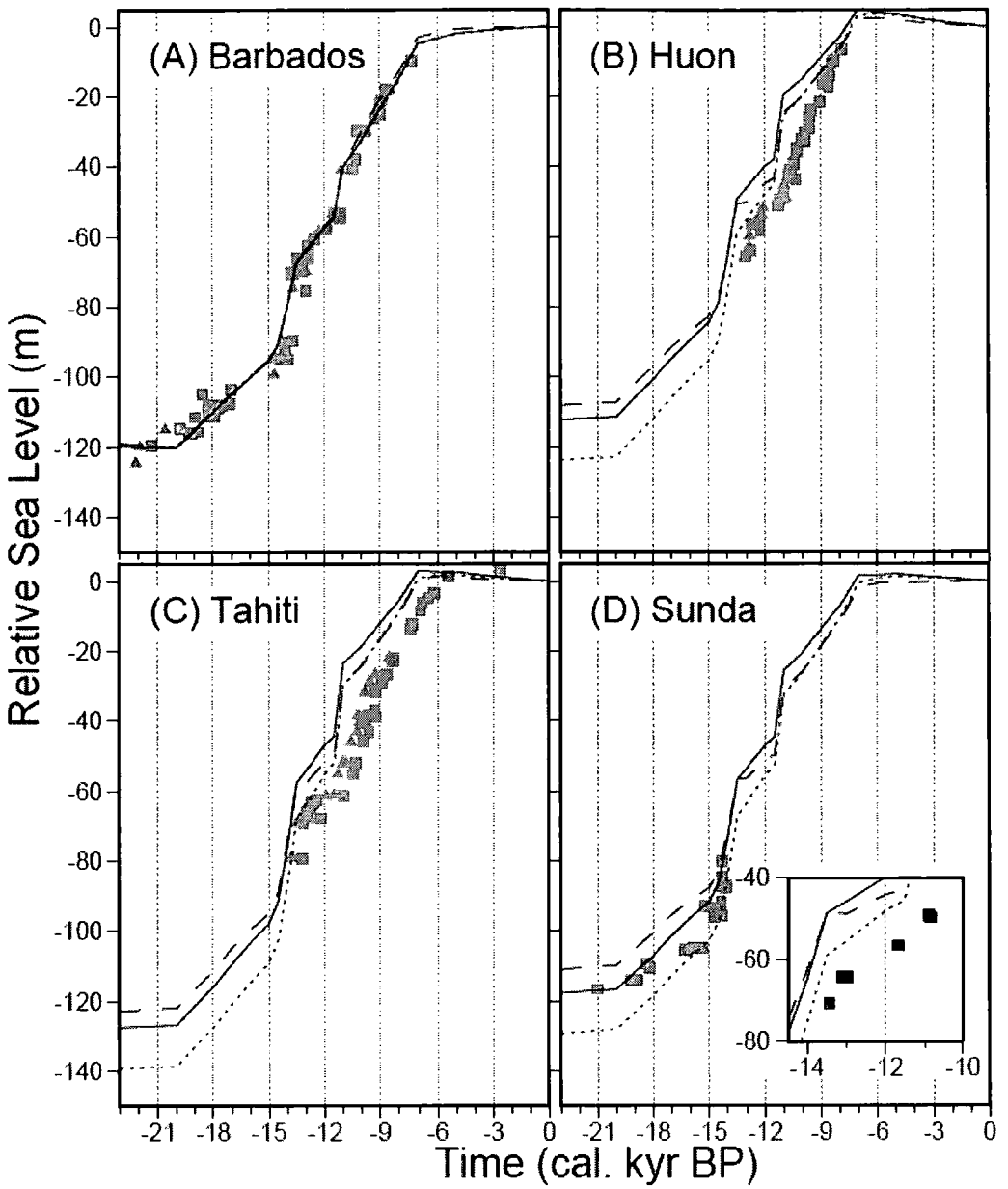

Figure 2.11: Sea-level predictions based on a dominant Laurentide contribution (0 m eustatic contribution from Antarctica) to mwp-IA for the reference earth model (solid line) and two other earth models that are the same as the reference model except that the lower mantle viscosity is reduced to 1 x 10^{21} Pa s (dashed) or increased to 50 x 10^{21} Pa s (dotted). The inset in Frame D shows the fit of the model predictions to the data from location B shown in Figure 2.2

First, the scenario of a dominant Laurentide source to mwp-IA is considered. Figure 2.9 and Figure 2.10 show the predictions based on the reference model and models that are the same as this model except the lithospheric thickness (Figure 2.9) or upper mantle viscosity (Figure 2.10) is altered. Altering the upper mantle and

lithospheric thickness parameters has an insignificant effect on the predicted sea-level change at these locations. The most significant variation in predictions is seen when the lower mantle viscosity is increased or decreased as illustrated in Figure 2.11.

Figure 2.11 shows predictions based on the reference viscosity model (solid lines) as well as viscosity models that are the same as this model except that the viscosity in the lower mantle is reduced to 10^{21} Pa s (dashed lines) or increased to 5×10^{22} Pa s (dotted lines). These predictions show that reasonable variations in the lower mantle viscosity can significantly alter the fit to the observations. For each viscosity profile, the ice history was tuned to fit the Barbados sea-level record (Section 2.3.2). Therefore, the change in the predicted sea-level curves at the southern sites is a consequence of both changes in the viscosity model and changes in the ice model. The post-mwp-IA fit at the three southern hemisphere sites is improved for the two bounding values of lower mantle viscosity, with the high viscosity model yielding the best results. However, both bounding models result in a significant misfit from the LGM to the time of mwp-IA at the Sunda Shelf.

2.3.6 Understanding the Results

In Figure 2.12 the spatially varying component of the total signal for each prediction shown in Figure 2.11 is shown. From Figure 2.12A, it is clear that the spatially varying signal at Barbados is dramatically altered when the lower mantle viscosity is changed. This result is not surprising since Barbados is situated within the peripheral bulge region of the North American ice sheets (e.g., [17]). The spatially varying signal at the other sites is less sensitive to changes in mantle

viscosity structure since they are located further from major glaciation centres.

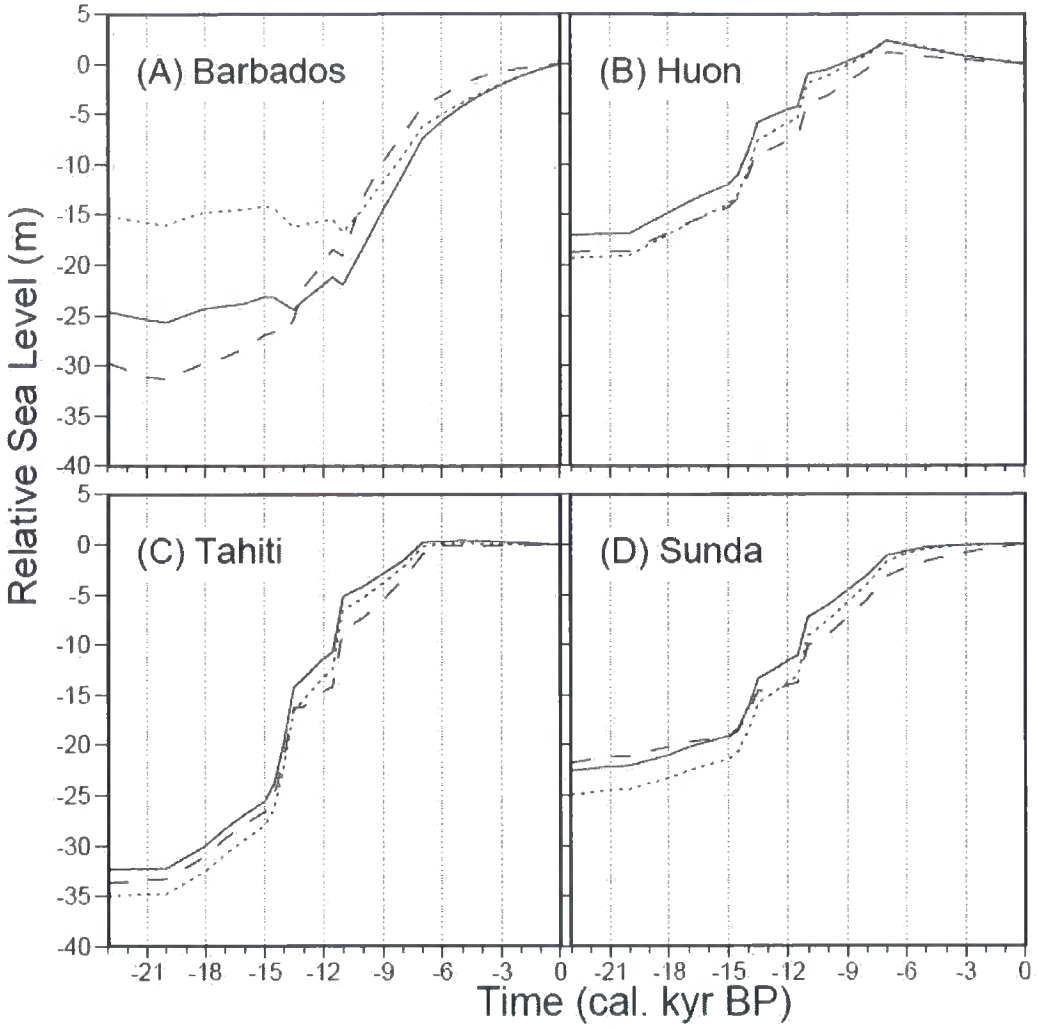

Figure 2.12: The spatially varying component of the total sea-level signal at the four data sites for the scenario of a 0 m eustatic contribution to mwp-IA from Antarctica. The solid line corresponds to a prediction based on the reference earth model. The dashed and dotted lines correspond to earth models that are the same as the reference model except that the lower mantle viscosity is 10^{21} Pa s and 5 $\times 10^{22}$ Pa s, respectively. The predictions for the Sunda Shelf are calculated for location A shown in Figure 2.2.

The sensitivity of the predictions to viscosity, shown in Figure 2.12, can be used to gain insight into the results shown in Figure 2.11. For example, the improved fit for the model with a reduced lower mantle viscosity (dashed line) is due to the increased rise produced between 14 and 11 cal. kyr BP at Barbados compared to that for the reference viscosity model. The lower viscosity permits the earth

model to respond faster to the rapid deglaciation of the Laurentide ice sheet during mwp-IA. The more rapid sea-level rise due to solid earth deformation during this period is compensated for by reducing the melt signal to maintain a good fit to the Barbados data set. This decrease in the melt input is the dominant effect on predicted sea-level change at the southern hemisphere sites in Figure 2.11 and results in an improved fit following mwp-IA. Note, however, that the sea-level rise across mwp-IA remains too large at all the southern hemisphere sites for this source scenario.

For the case of a high lower mantle viscosity (dotted line), the isostatic response is much slower and so the magnitude of sea-level rise due to crustal subsidence at Barbados from LGM to present is significantly reduced compared to the reference viscosity model. To compensate for this, and thus maintain a good fit to the Barbados data, a greater amount of melt is required from the Laurentide ice sheet during the deglaciation period. This change in the ice model produces an additional and relatively steady increment sea-level rise at the southern hemisphere sites and an improved fit to the data following mwp-IA.

Figure 2.13 shows normalised χ^2 values for the post LGM fit to far-field data and the dominant Laurentide and Antarctic melt scenarios. Results are shown for five earth models with different lower mantle viscosities. The normalised χ^2 values (Figure 2.13) are consistent with the discussion of Figure 2.11; the reference model yields the worst overall fit and models with relatively stiff lower mantle regions produce the lowest chi-squared values. (A normalised chi-squared value of one or less indicates a model prediction that fits all the data to within the specified error). The preference of the data for a relatively high value of lower mantle viscosity is

consistent with the results in a recent study [16] which considered far-field sea-level data both prior to and following the LGM.

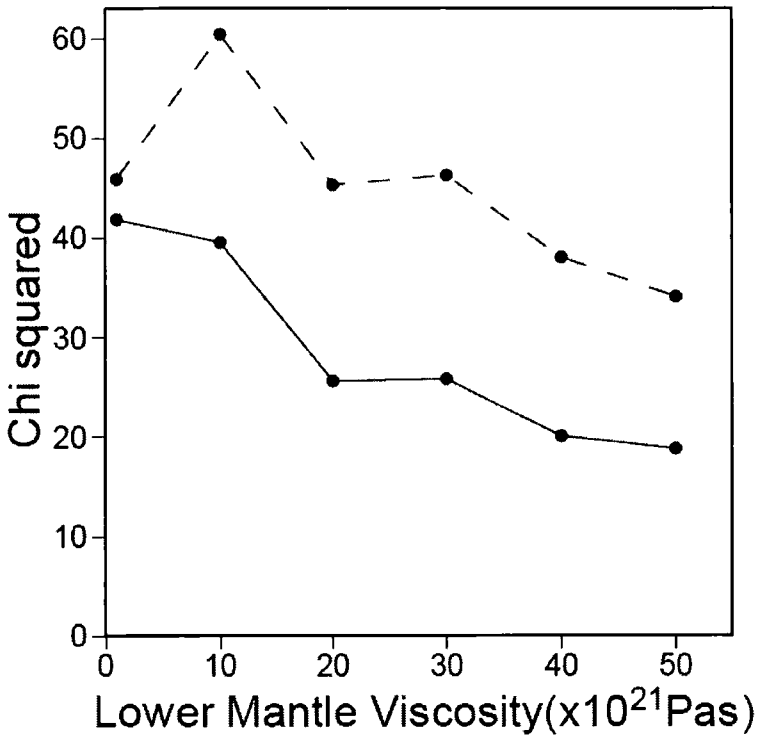

Figure 2.13: Normalised χ^2 misfit between predictions generated using GIA models tuned to the Barbados sea-level record and post-LGM observations as a function of lower mantle viscosity. The models assume either a dominant North American source for the meltwater event mwp-IA (dashed line), or a contribution from the Antarctic ice complex equivalent to 15 m of eustatic sea-level rise (solid line).

In contrast to the monotonic improvement in fit at Huon and Tahiti as the lower mantle viscosity is increased from $2 - 5 \times 10^{22}$ Pa s, the fit at Sunda is relatively constant. This is because the improvement to the post mwp-IA fit at this site is counteracted by degradation of the fit to the older data as the viscosity is increased.

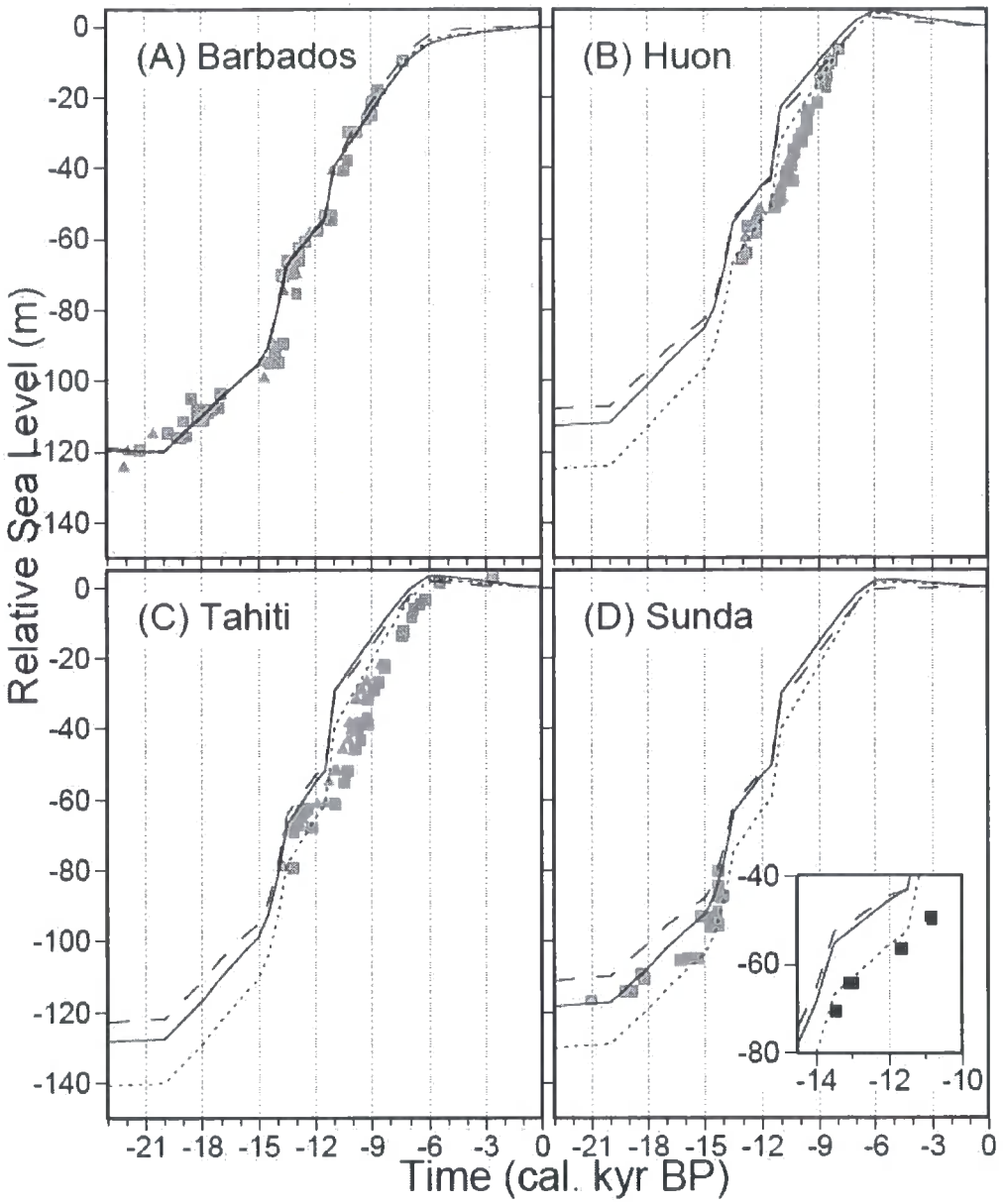

Figure 2.14: Sea-level predictions based on a dominant Antarctic contribution (15 m eustatic) to mwp-IA for the reference earth model (solid line) and two other earth models that are the same as the reference model except that the lower mantle viscosity is reduced to 10^{21} Pa s (dashed) and increased to 5×10^{22} Pa s (dotted). The inset in Frame D shows the fit of the model predictions to the data from location B shown in Figure 2.2.

In Figure 2.14, the effect of changing lower mantle viscosity for the scenario of a dominant Antarctic source to mwp-IA is considered. In this case, reducing the mantle viscosity does not produce a significant change compared to the reference model. This is largely because the mass removal from the Laurentide ice sheet is

less in the Antarctic dominant scenario and so the magnitude of crustal subsidence at Barbados during and shortly after the melt water pulse is significantly reduced. As a consequence, sea-level predictions immediately following mwp-IA will be less sensitive to changes in viscosity. The effect of increasing the lower mantle viscosity is, in contrast, similar to the dominant Laurentide contribution. As before, a stiffer mantle leads to a reduction in the magnitude of the solid earth response at Barbados over the entire post-LGM period; this is compensated for by an increase in mass volume to maintain a good fit to the Barbados record, and thus an increased sea-level rise at the southern sites.

The optimum overall fit is produced by the combination of a dominant Antarctic melt scenario and a lower mantle viscosity of 5×10^{22} Pa s. As can be seen from Figure 2.14, this model provides an excellent fit to the data at Huon, Sunda and Tahiti post mwp-IA and before the occurrence of mwp-IB. The chi-squared value for this optimal model is 18.8, compared to 34.6 for the optimal prediction based on a dominant Laurentide source (see Figure 2.13; this chi-squared reduction is significant to greater than the 99% confidence level). The relatively high chi-squared value for the best fit model reflects the significant misfits to the earlier data from Sunda and the data from Huon, Tahiti and, to a lesser extent, Sunda in the period ~11 to 9 cal. kyr BP.

2.4 Discussion and Summary

The melt scenario characterised by a dominant (15 m) Antarctic source for mwp-IA, combined with the 5×10^{22} Pa s lower mantle viscosity model produces the best fit to the suite of far-field observations. However, as described above, there

remain significant misfits between the data and this model. Here, two further issues in relation to this residual signal are discussed briefly.

First, the poor fit during the period ~11-9 cal. kyr BP, which coincides with the occurrence of mwp-IB at the Barbados site is considered. The existence of this event was proposed following the reconstruction of the Barbados sea-level record [20]. More recent far-field records (e.g., Huon and Tahiti) do not support the existence of this event. The occurrence of mwp-IB has also been questioned on the basis a high quality near-field sea-level record from Scotland that would mark such an event by a change in sign of the trend in sea level at that time [25]. The modelling of this meltwater event and the effect on the fit to the data during the period ~11-9 cal. kyr BP is considered in more detail in Chapter 3.

The over prediction, by the optimal model (Figure 2.14), of LGM sea levels at the Sunda Shelf is now considered. The nature of the dating constraints for the oldest data from this region (index points older than 18 cal. kyr BP) has led to suggestions that the dates may be biased too old (see Section 2.2.2). If this is the case, then it is possible that the misfit in Figure 2.14 may be at least partly due to problems with the data. This misfit is discussed further in Chapter 3.

If the oldest observations from the Sunda Shelf are biased too old, then the model comprising a dominant (15 m eustatic) Antarctic contribution to mwp-IA and Earth structure characterised by a 96 km thick (elastic) lithosphere, a 5×10^{20} Pa s upper mantle viscosity and a 5×10^{22} Pa s lower mantle viscosity simultaneously provides an improved fit to the observations at all four sites considered compared to a Laurentide source model. The preferred viscosity model is broadly consistent with recent inferences of this parameter that suggest relatively high values of lower

mantle viscosity compared to earlier studies ([11, 72]). The optimal ice history is somewhat more controversial given the magnitude of melt required from the Antarctic ice sheet over a short time period (< 1 kyr). Though recent field work has provided evidence for ice retreat in some regions around the time of mwp-IA (e.g. [73]), a volume reduction equivalent to 15 m eustatic sea-level rise between 14.5 and 13.5 cal. kyr BP is large relative to geological and glaciological evidence that suggest the excess ice contained in this ice sheet at LGM was less than ~20 m. The ice history model proposed on the basis of this study requires further, independent testing. In Chapter 4 sea-level modelling of data from Antarctica is used to test the plausibility of different deglaciation scenarios.

The principal limitation of the model applied in this analysis is the assumption of 1-D earth structure. In future analyses the above analysis should be extended to 3-D earth models (e.g., [74]) in order to assess the robustness of the conclusions reached above. There are a variety of ways in which observational constraints can be improved. There is a compelling need for more sea-level records with temporal coverage similar to the Barbados and Sunda Shelf data set; particularly at locations that are not significantly affected by crustal motions due to either GIA or plate tectonics. Also, it is important to consider direct evidence from near-field records. A large and rapid melting event from Antarctica would most likely leave a geomorphological, geochemical and biological signal in local terrestrial and marine records. It is important to focus future initiatives on records of these types in order to further test the hypothesis of a dominant Antarctic source to mwp-IA.

Chapter 3 Far-Field Sea-Level Modelling of Mwp-IB and the 19 kyr Pulse

3.1 Introduction

The far-field sea-level modelling performed in Chapter 2 resolved some of the key misfits to the far-field observations during the period from the LGM to present day, particularly during and shortly after the occurrence of mwp-IA. As stated in Section 2.4, however, there are still some unresolved discrepancies in the optimum fit model from the previous chapter. The work presented in this chapter addresses these misfits further.

Firstly, the misfit observed during the period 11-9 cal. kyr BP is considered. The reconstructions of the previous chapter all included two pulses at 14.5-13.5 cal. kyr BP and 11.5-11 cal. kyr BP (mwp-IA and mwp-IB respectively). These meltwater events were first identified in the reconstruction of the Barbados sea-level curve [20]. Whereas mwp-IA has been observed in the Sunda Shelf record [22] (and indirectly in the Tahiti record) there is no evidence for mwp-IB in either the Huon or Tahiti records (see Figure 2.1) [23, 24]. There is also evidence from high quality near field data in Scotland which does not support the existence of mwp-IB [25]. Therefore, in the following section, we extend the modelling of Section 2.3 to further test the existence of mwp-IB.

The misfit to the LGM data at Sunda Shelf noted in Section 2.4 is also

discussed in more detail in this chapter. As previously suggested, this could be a result of the older data at this site being biased too old (see Section 2.2.2). In Section 3.3 we explore the LGM misfit further by extending our data set to include those recently obtained from the Bonaparte Gulf, north-western Australia [21]. These data provide some of the most accurate constraints on LGM sea level and so present a useful additional test of our sea-level model.

The sea-level record from Bonaparte Gulf has been used to argue for a rapid sea-level rise of between 10 and 15 m at around 19 cal. kyr BP [21]. The existence of a meltwater pulse at this time has been disputed because the proposed pulse event is not captured by data derived from a single core but from a reconstruction of data from a number of different cores [26]. Recently, further evidence for the existence of a rapid sea-level rise of at least 10 m at 19 cal. kyr BP comes from sediment records from the Irish Sea [27]. Climate records from the time of this pulse indicate that the source of meltwater for this event most likely originated from one or more of the northern hemisphere ice sheets [27]. In Section 3.4, we incorporate a 19 cal. kyr event into the sea-level model to determine whether the data from Barbados and Sunda Shelf are consistent with such an event. We also consider a small number of different source scenarios to test if the available data can be used to constrain the source geometry.

3.2 Modelling of Mwp-IB

A revised melt model that includes a 15 m Antarctic contribution to mwp-IA but does not include a distinct mwp-IB event was constructed. The dashed line in Figure 3.1 shows the total predicted sea-level signal at four far-field data locations

for a 15 m Antarctic contribution to mwp-IA and an earth model with a lower mantle viscosity of 5 x 10^{22} Pa s. This model combination provides the best fit to the data set for ice histories that include the mwp-IB event. The solid line demonstrates the improvement to the fit that is produced by not including mwp-IB in the ice history. Of course, this revision results in a diminished quality of fit to the Barbados record post ~11 cal. kyr BP; however, the data are still fit to within the observational error. The slightly poorer fit at Barbados is more than compensated for by the dramatic improvement to the fit at the other three sites (see Figure 3.1).

This "no-mwp-IB" melt model was then adapted to consider a variety of lower mantle viscosity models where the model is refined until a similar fit to the Barbados record is obtained. The results of this exercise are summarised in Table 3.1 where the given total χ^2 values are based on the model fit at Huon, Tahiti and Sunda (since all models are tuned to fit the Barbados record the fit at this site was not considered). As expected, for a given viscosity model, the χ^2 values at Barbados for the "no-mwp-IB" case are slightly larger than those for the ice model that includes this event; however, this is more than compensated for by the dramatic reduction in the χ^2 values at the other three sites. For example, consider the results for the intermediate lower mantle viscosity of 3 x 10^{22} Pa s. The χ^2 misfit at Barbados is increased by 23 %, compared to a decrease in this value of 89%, 59% and 81% at Huon, Sunda and Tahiti, respectively.

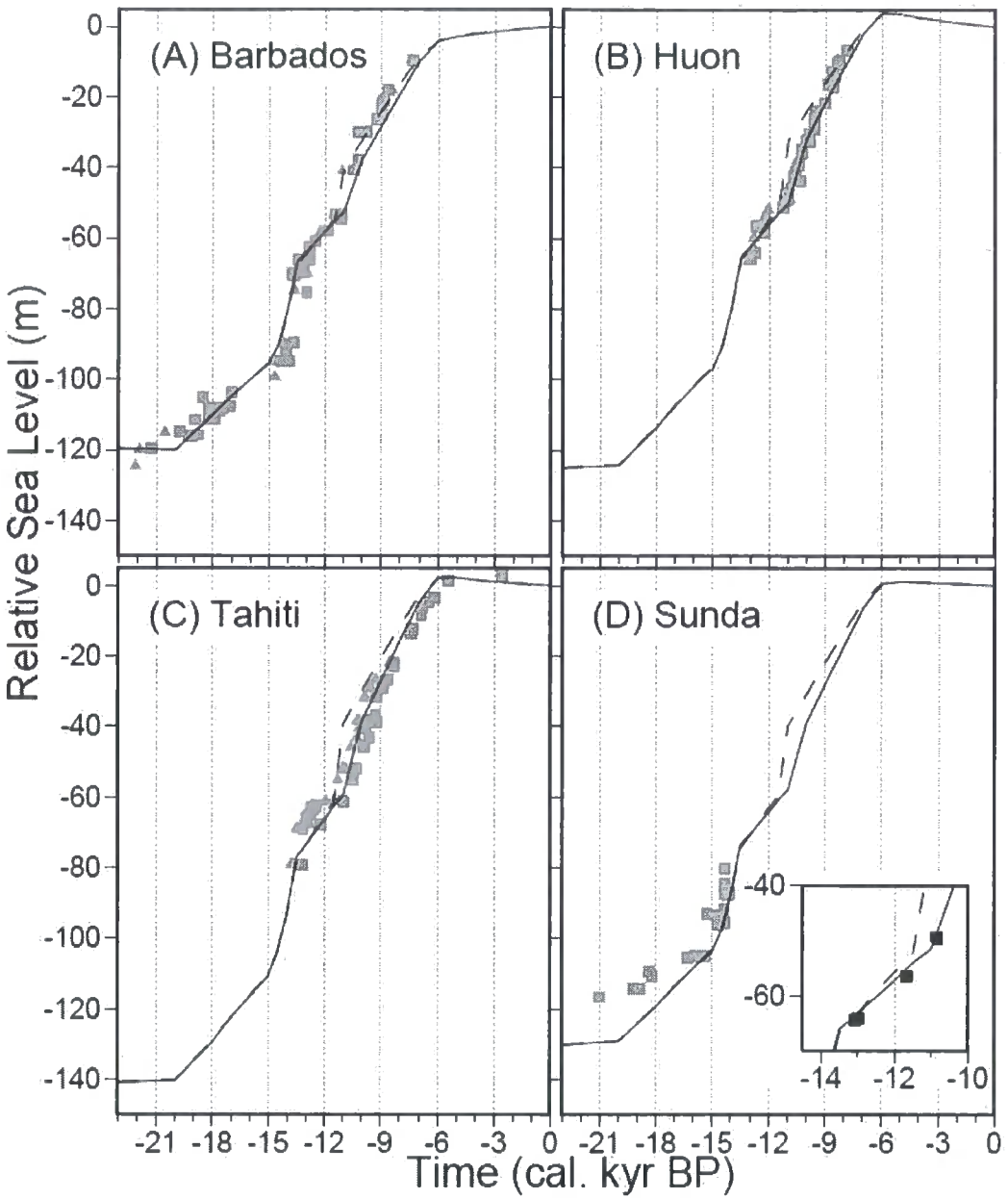

Figure 3.1: Sea-level predictions based on a dominant Antarctic contribution (15 m eustatic) to mwp-IA for an earth model with lower mantle viscosity of 5 x 10^{22} Pa s. The dashed line corresponds to the optimum fit for an ice model that includes the mwp-IB event (see Chapter 2). The solid line demonstrates the change in the predictions for a model with no distinct mwp-IB in the ice history. The inset in frame D shows the fit of these two models to the data from location B (see Figure 2.1, Section 2.2.2).

Lower mantle viscosity (x 10^{21} Pa s)		Barbados	Huon	Sunda	Tahiti	TOTAL
1	With IB	3.86	6.23	16.22	19.44	41.89
	Without IB	3.92	1.85	12.24	5.96	20.05
10	With IB	3.67	7.67	10.76	21.14	51.33
	Without IB	4.21	1.92	6.01	5.27	13.20
20	With IB	3.77	2.63	6.22	18.40	27.25
	Without IB	4.22	0.424	2.73	4.17	7.32
30	With IB	3.52	3.81	5.91	15.64	25.36
	Without IB	4.29	0.44	2.41	3.02	5.87
40	With IB	3.57	3.13	6.60	10.35	20.08
	Without IB	4.07	0.37	4.04	1.92	6.33
50	With IB	3.52	2.41	8.15	8.28	18.84
	Without IB	3.92	0.43	6.06	2.06	8.56

Table 3.1: χ^2 values for a number of different viscosity and ice models as discussed in the text. Note all models are tuned to fit the Barbados record and therefore the "total" value is a sum of the chi squared values at the remaining sites and gives a measure of the goodness of fit.

The optimum fit to the entire data set, based on this "without mwp-IB" melt model, is achieved with a lower mantle viscosity of 3 x 10^{22} Pa s. This particular model yields a normalised χ^2 value of 5.87, which is a 69% reduction compared to

the optimal model that included mwp-IB described in Chapter 2. This improvement in fit is significant at greater than the 99% confidence level. The model with lower mantle viscosity of 4 x 10^{22} Pa s and no mwp-IB also shows significant improvement of fit compared to the optimal fit of Chapter 2. Note that the difference in fit produced by the two best fit lower mantle viscosity models (3 x 10^{22} and 4 x 10^{22} Pa s) is not statistically significant. These two models are shown in Figure 3.2.

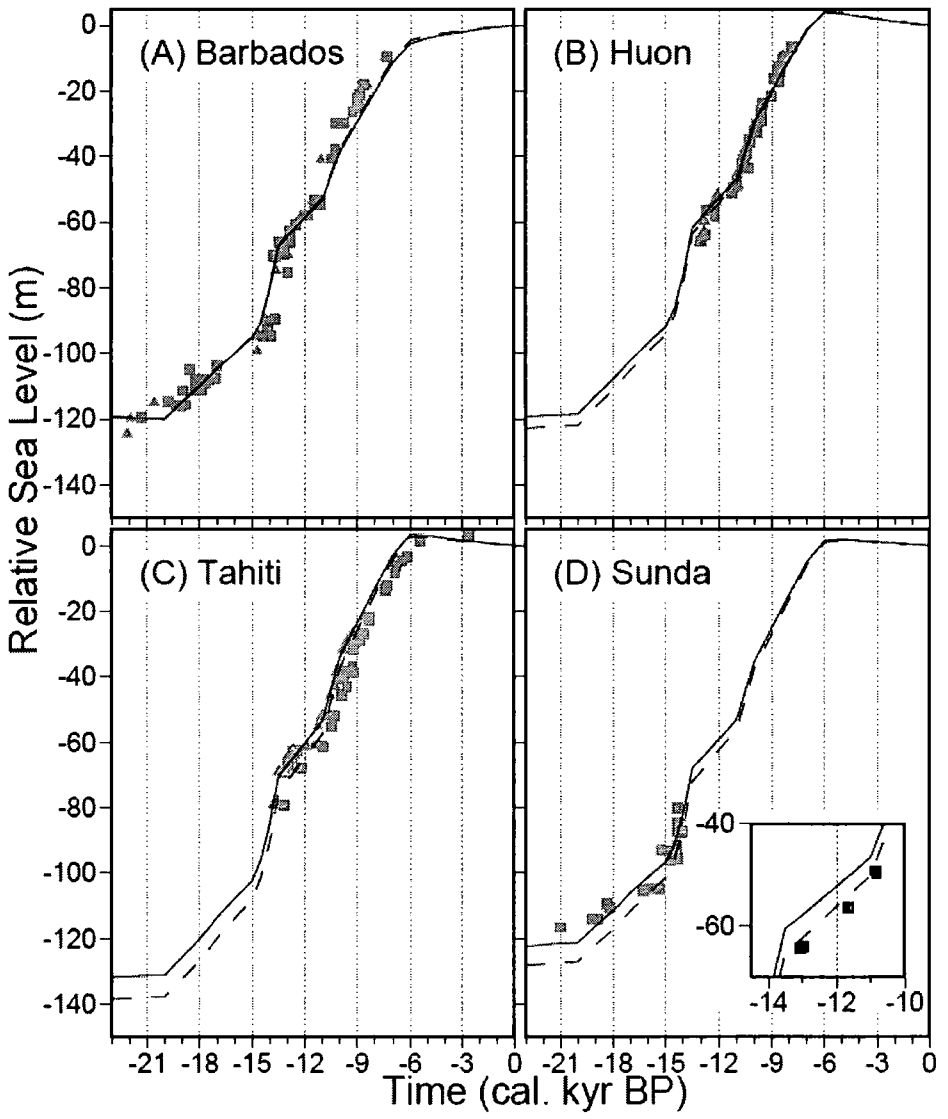

Figure 3.2: Sea-level predictions based on a dominant Antarctic contribution (15 m eustatic) to mwp-IA and no distinct mwp-IB event for earth models with lower mantle viscosity of 3 x 10 ^{22} Pa s (solid line) and 4 x 10^{22} Pa s (dashed line). Frame D shows the fit of these two models to the data from location B (see Figure 2.2, Section 2.2.2).

Figure 3.2 demonstrates the trade off that occurs between the fit to the oldest and youngest data in the Sunda record. By increasing the lower mantle viscosity, the fit to the post mwp-IA data is improved whereas the fit to the LGM data is degraded. These results demonstrate that the oldest Sunda data are driving the overall preference for the 3 x 10^{22} Pa s viscosity model compared to the 4 x 10^{22} Pa s model, which significantly over predicts the depth of LGM sea level at this site. This LGM misfit is considered in more detail in the following section.

3.3 Exploring the LGM misfit

In order to explore the misfit of the optimal models obtained in Section 3.2 to the LGM data at Sunda Shelf, and to test the plausibility of this being a result of problems with the data, we extend our data set to include observations of LGM sea level from Bonaparte Gulf. The data from this region are based, largely, on the analysis of organic material found in sediment cores [21]. Samples indicating brackish or marginal marine conditions are used to reconstruct past sea levels in this area. These data were corrected for formation depth and the vertical errors are those associated with formation depth and tidal range. This area is believed to have been tectonically stable and so no correction has been applied to the observations. The dates are calibrated carbon dates from the CALIB program [45].

Figure 3.3 compares the two best fit earth/ice models from Section 3.2 to the observations at Bonaparte Gulf. Figure 3.3 shows that the Bonaparte Gulf data are more closely fit by the model with lower mantle viscosity of 4 x 10^{22} Pa s (dashed line). The success of this model at Bonaparte Gulf supports the argument that the age of the oldest data at the Sunda Shelf may be biased too old by 2-3 kyr (see

Section 2.4).

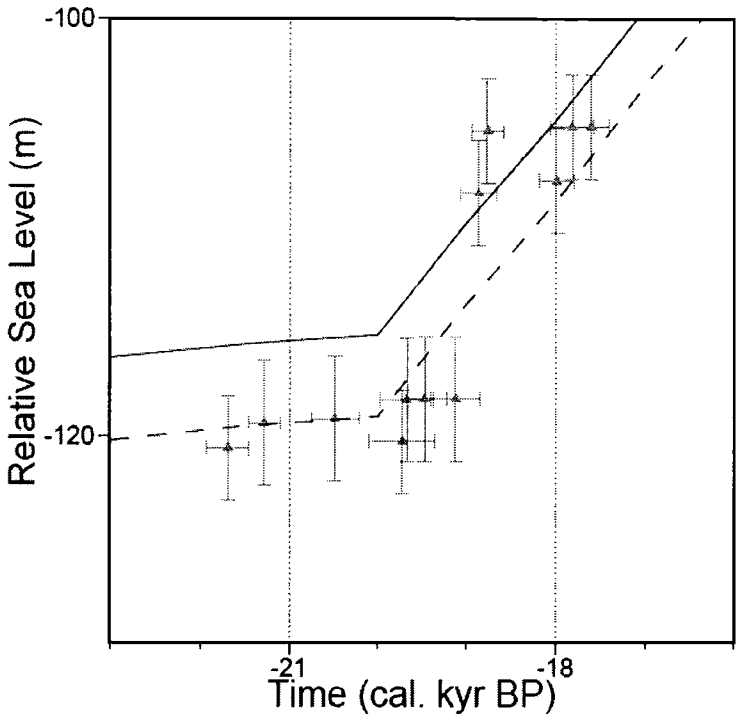

Figure 3.3: Comparison of observed and predicted sea levels at Bonaparte Gulf for the two best fitting earth models of Section 3.2 which include a 15 m eustatic Antarctic contribution to mwp-IA and no distinct mwp-IB event. The two earth models considered have lower mantle viscosities of 3 x 10^{22} Pa s (solid line) and 4 x 10^{22} Pa s (dashed line).

In order to examine this "best fit" earth model a number of ice melt scenarios have been developed that do not include a distinct mwp-IB event but consider different contributions from the Antarctic ice complex. The modelling performed here is similar to that carried out in Section 2.3.2 with the contribution from the Antarctic ice sheet to mwp-IA being scaled to provide 0, 5, 10, 15 and 20 m of eustatic sea-level contribution to the pulse. As before, all models are scaled to give a similar fit to the Barbados record and the fit at the remaining sites provides a measure of the success of the model run. The results are shown in Figure 3.4.

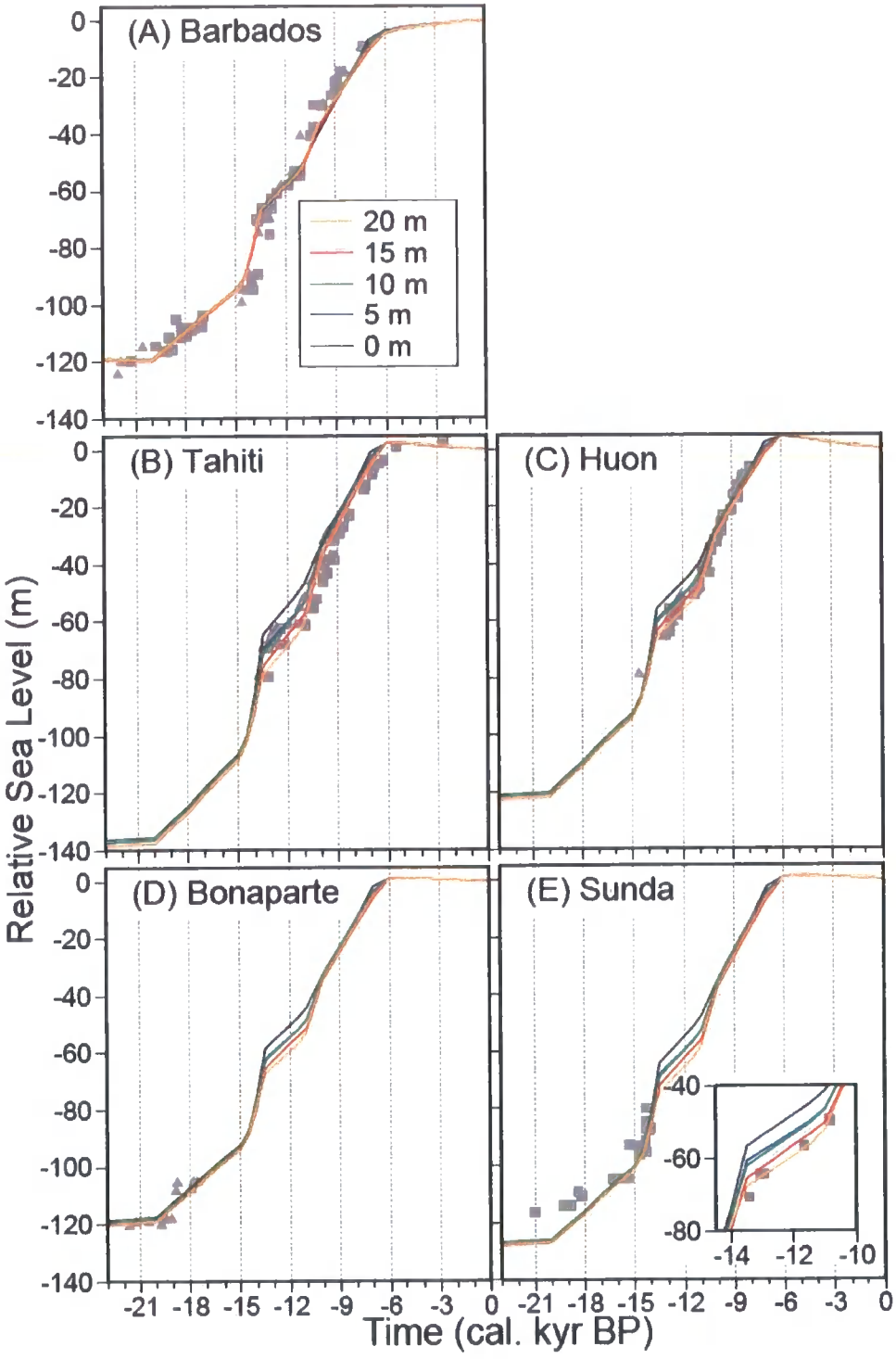

Figure 3.4: Sea-level predictions based on an earth model with lower mantle viscosity of 4 x 10^{22} Pa s and a range of melt scenarios to illustrate the sensitivity to changes in the relative contributions of the Laurentide and Antarctic ice sheets to mwp-IA. The key in Frame A identifies the contribution, in eustatic sea level, from the Antarctic ice sheet for each model run. Each model was tuned to fit the Barbados record and include no distinct mwp-IB event. The inset in Frame E shows the fit of the model predictions to the data from location B shown in Figure 2.2, Section 2.2.2. From [19]

Figure 3.5 shows the χ^2 values for the separate sites over the entire time period (A) and just the period following the pulse, ~14-9 cal. kyr BP (B). Increasing the Antarctic component of mwp-IA up to 15 m decreases the misfit to all the records by 48 %. A further increase in the Antarctic component serves to increase the misfit as a result of pushing the sea level at Tahiti too low after the pulse. This is evident in the χ^2 values shown in Figure 3.5B, in which the deterioration in the goodness of fit is seen for the Lateglacial period at Tahiti (red line). Altering the contribution from Antarctica to mwp-IA has little effect on the fit to the Bonaparte Gulf data (green line in Figure 3.5A) as this data set only samples the period at and shortly after LGM.

Due to the uncertainty in the accuracy of the Sunda Shelf LGM data the discussion here focuses mainly on the Lateglacial fit (Figure 3.5B). Figure 3.5B shows that by increasing the Antarctic contribution from 0 m to 5 m (black and blue lines Figure 3.4) there is a significant improvement in fit at all sites for the Lateglacial period. There is little improvement when the Antarctic contribution is increased to 10 m and then a further significant jump between 10 and 15 m (green and red lines Figure 3.4) most notably at Sunda (blue line Figure 3.5B).

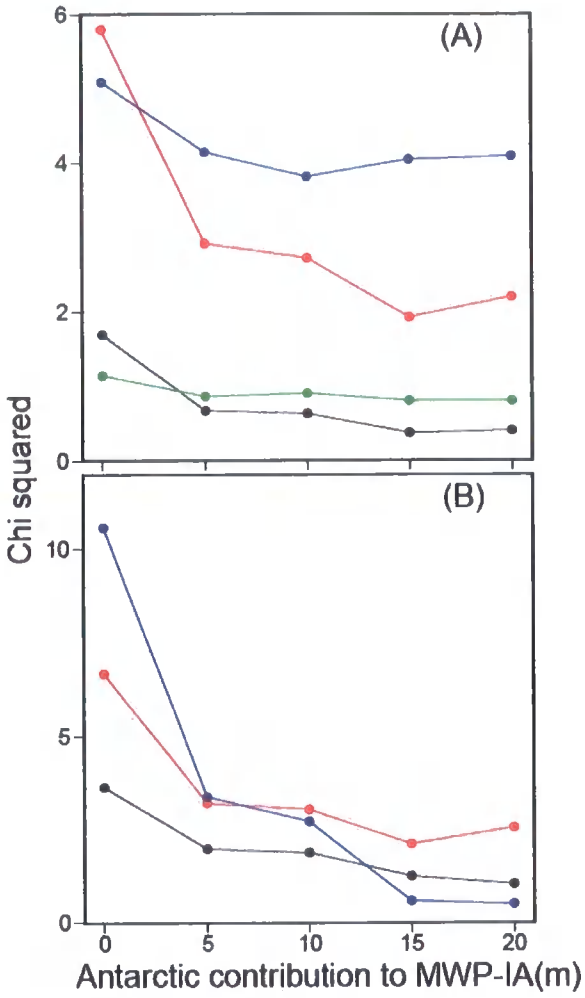

Figure 3.5: (A) Normalised χ^2 misfit between predictions and post-LGM observations at four locations: Huon (black line), Tahiti (red line), Sunda (blue line) and Bonaparte Gulf (green line). Model predictions were generated using a GIA model tuned to the Barbados sea-level record for an earth model with a lower mantle viscosity of 4 x 10^{22} Pa s and a range of Antarctic contributions to mwp-IA (in units of equivalent eustatic sea-level change; see x-axis). (B) Same as (A) but χ^2 is calculated over the Lateglacial period only (~14-9 cal. kyr BP).

3.4 Modelling the 19 cal. kyr pulse

In this section, the misfit of the best fit model obtained in Section 3.3 to the Sunda Shelf LGM data is investigated further. As discussed in Section 2.4 this misfit might be the result of the data being biased too old due to the dating methods used; this possibility is supported by the high-quality fit of the 40 x 10^{21} Pa s viscosity

model at Bonaparte Gulf (see previous section). However, on examination of the Bonaparte Gulf data set (Figure 3.3), it is evident that an ice melt model which includes a rapid melting event at ~19 cal. kyr BP would improve the fit to the observations at this location [21, 27]. We examine, in the following, whether the data at Barbados and Sunda Shelf preclude the occurrence of a rapid sea-level rise at this time.

New models that are based on the best fit model of Section 3.3 have been developed which include a ~10 m eustatic sea-level rise between 19.5 and 19 cal. kyr BP with four dominant melt source regions: North American, European, Antarctic and northern hemisphere. The results for these models are shown in Figure 3.6 along with the optimum model from Section 3.3 which does not include a melt water pulse at this time.

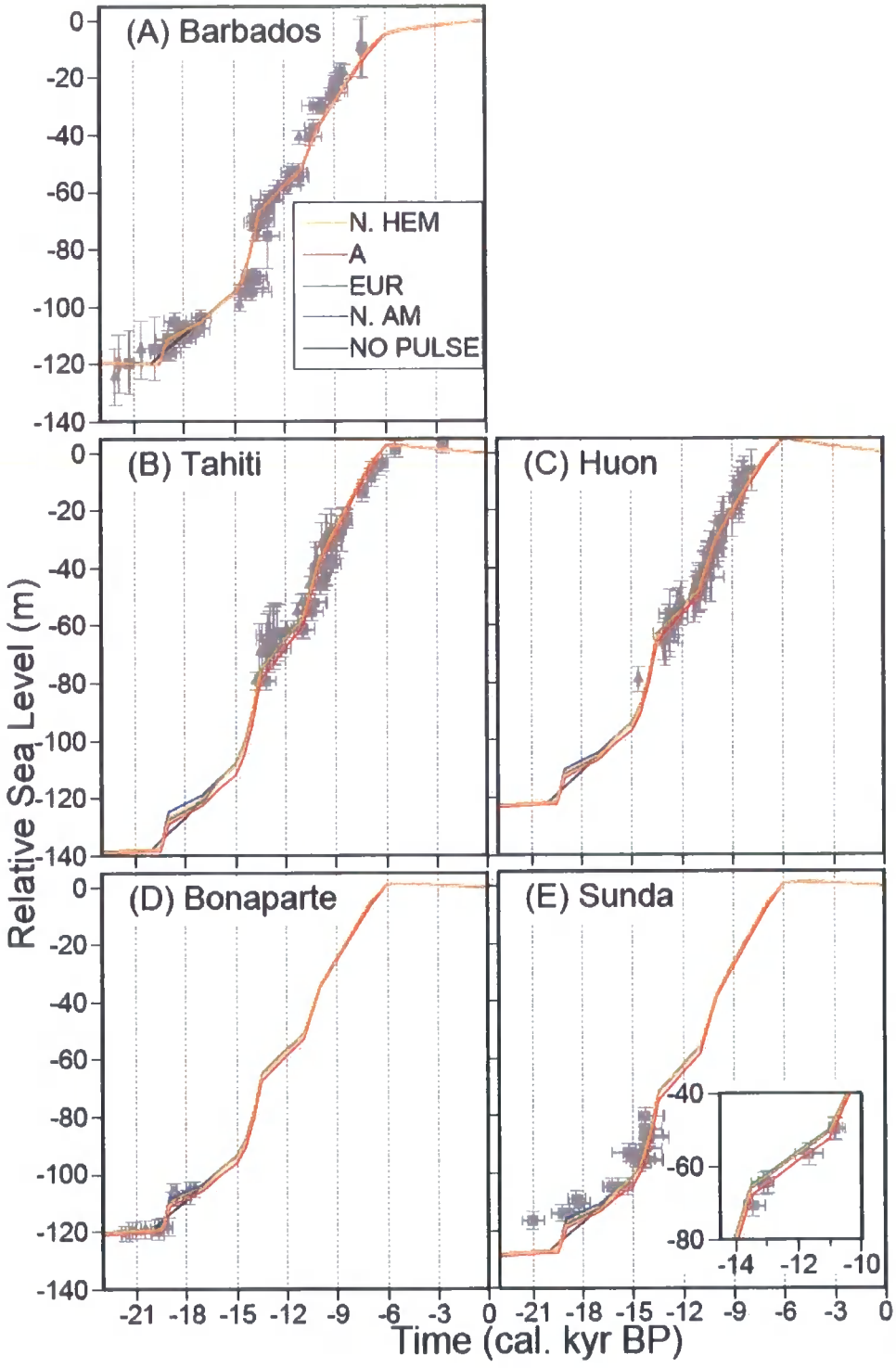

Figure 3.6: Sea-level predictions based on an earth model with lower mantle viscosity of 4 x 10^{22} Pa s and a range of melt scenarios to illustrate the sensitivity to changes in the relative contributions of the N. American, European and Antarctic ice sheets to the 19 cal. kyr BP event (see key in Frame A). Each model was tuned to fit the Barbados record and include no distinct mwp-IB event. The inset in Frame E shows the fit of the model predictions to the data from location B shown in Figure 2.2.

The contribution from the North American ice sheet was altered so the total eustatic sea-level rise between 19.5-19 cal. kyr BP was 10 m (~8 m North American and 2 m European) while still providing a reasonable fit to the Barbados record. This model is shown as the blue line in Figure 3.6. The other models were generated by increasing the eustatic components of each of the other ice sheets to the required contribution and then tuning the North American component in the resulting model to obtain the same fit to the Barbados record (see Section 2.3.2). The eustatic contribution from each ice sheet for each of the models shown in Figure 3.6 is given in Table 3.2. Notice that the total eustatic contribution is different in each case as a result of tuning to the Barbados record.

	North American Ice Sheet	**Antarctic Ice Sheet**	**European Ice Sheet**	**Total**
No 19 kyr pulse (NO PULSE)	0 m	0 m	2.4 m	2.4 m
N. American (N. AM)	7.6 m	0 m	2.4 m	10 m
Northern hemisphere (N. HEM)	4.5 m	0 m	4.5 m	9 m
European (EUR)	0.8 m	0 m	8.0 m	8.8 m
Antarctic (A)	0.8 m	5 m	2.4 m	8.2m

Table 3.2: Table to show the eustatic contributions from each ice sheet in the various ice models used to generate the results in Figure 3.6.

As can be seen from Figure 3.6 the 19 cal. kyr BP event has little effect on the

fit to the late glacial sea-level record except in the case where there is a dominant contribution to this event from the Antarctic ice complex (red line, Figure 3.6). In this case, increasing the Antarctic contribution to this pulse reduces the total eustatic contribution required to produce the modelled sea-level rise at Barbados and thus causes a lowering of the curves predicted at the remaining locations. This result is a consequence of different effects, including, for example, the subsidence effects of the peripheral bulge of the North American ice sheet at Barbados and the distinct sea-level pattern (or fingerprint) associated with Antarctic melting (see Section 2.3.4 for more detail). The implications of this can be seen in the χ^2 values shown in Table 3.3.

	Barbados	**Huon**	**Sunda**	**Tahiti**	**Bonaparte**	**Total**
No 19 kyr pulse (NO PULSE)	4.07	0.37	4.04	1.92	0.8	7.13
N. American (N. AM)	4.13	0.37	3.36	1.92	0.81	6.46
Northern hemisphere (N. HEM)	4.1	0.37	3.48	1.92	0.58	5.99
European (EUR)	4.19	0.37	3.44	1.94	0.54	5.94
Antarctic (A)	4.00	0.45	5.56	2.28	0.43	8.50

Table 3.3: χ^2 values for the period from LGM to present day for a number of different source models for 19 cal. kyr BP event as discussed in the text. Note all models are tuned to fit the Barbados record and therefore the "total" value is a sum of the chi squared values at the remaining sites and gives a measure of the goodness of fit.

The χ^2 values shown in Table 3.3 show that the inclusion of the 19 cal. kyr BP

pulse in the Barbados record does not prove detrimental to the fit to this sea-level record but does improve the fit to the Bonaparte Gulf and Sunda Shelf data. The χ^2 values (Table 3.3) show that a 19 cal. kyr BP pulse sourced from northern hemisphere ice sheets would improve the fit to the complete set of far-field data considered, whereas a dominant Antarctic source produces a fit that is poorer than that achieved with a model that does not include the 19 cal. kyr event. The deterioration in fit is driven mainly by the lowering of the relative sea-level curve after the 19 cal. kyr BP event at all sites. The above results show that including a melt event at 19 cal. kyr BP produces an improvement in the model fit to the data but only for the case in which the meltwater is sourced from the northern hemisphere. In particular, the optimum fit is achieved when the melt is sourced from a combination of northern hemisphere ice sheets (N. HEM. model) or the Eurasian ice sheets (EUR model). These models show a 16-17 % improvement to the data model fit compared to the optimum model obtained in Section 3.3; however, this variance reduction is not statistically significant. The reduction in the χ^2 values is driven by the improvement of fit to the Bonaparte Gulf and Sunda Shelf data for the earliest part of these sea-level records (Figure 3.7).

Figure 3.7 shows only the period from 23 to 16 cal. kyr BP for the three locations which have data that sample this time period (Barbados, Bonaparte Gulf and Sunda Shelf). The χ^2 values associated with the predictions for this time period are shown in Figure 3.7 are shown in Table 3.4.

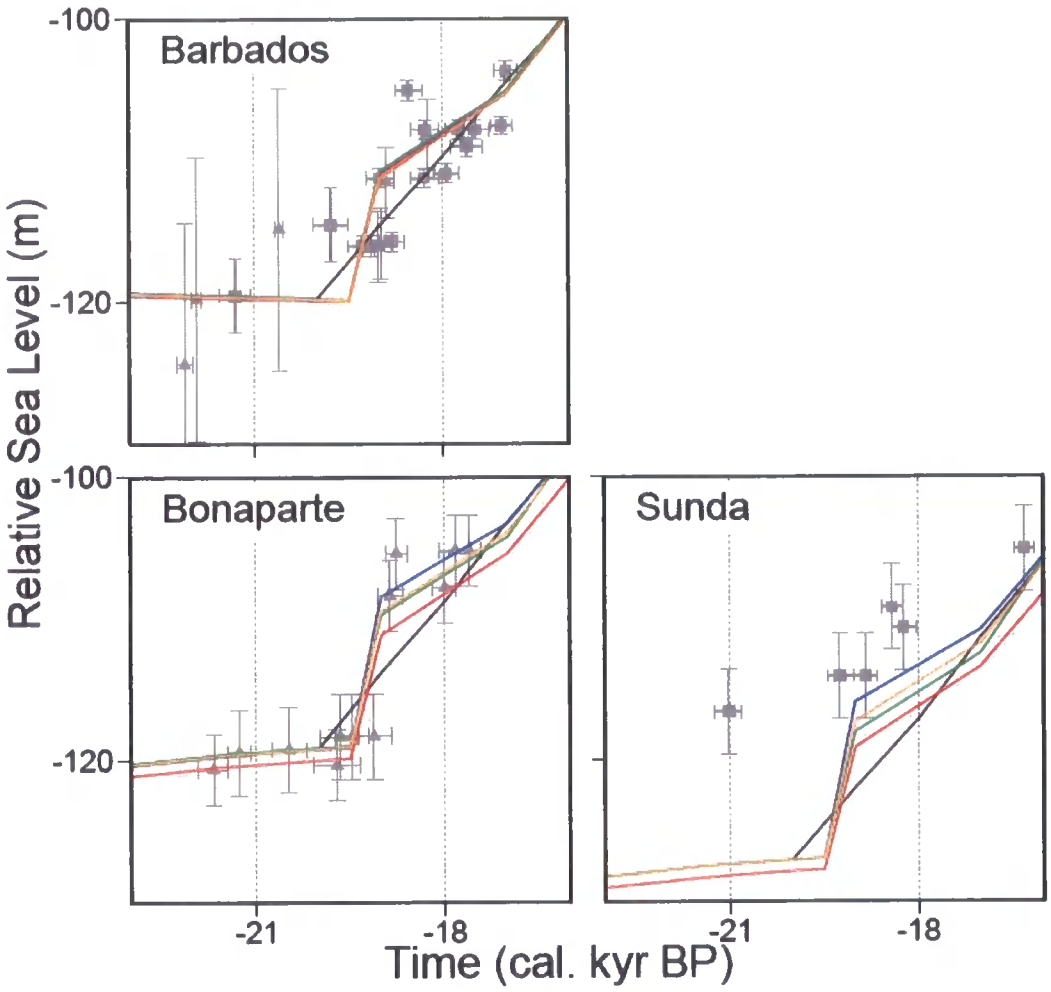

Figure 3.7: Same as Figure 3.6 except only the LGM data and predictions for Barbados, Bonaparte Gulf and Sunda Shelf have been shown. The predictions are described in detail in the text and are: No Pulse=black, N. American=blue, Europe=green, Antarctic=red and N. hemisphere=orange.

The results in Figure 3.7 and Table 3.4 show that including a pulse at 19 cal. kyr BP causes a relatively minor deterioration of fit to the Barbados sea-level observations over this time period compared to an improvement of fit to the sea-level data at both Bonaparte Gulf and Sunda Shelf. The total χ^2 values (Table 3.4) indicate that the best fit is obtained when a North American source for the 19 cal. kyr BP event is considered (blue line). This is supported by the χ^2 values for the Sunda Shelf data-model fit (Table 3.4) which shows a 36 % reduction compared to the "no pulse" case. In contrast, the χ^2 value for the data-model fit at Bonaparte Gulf is highest for

the North American scenario and lowest for the Antarctic scenario. The χ^2 results for Bonaparte Gulf are not consistent with the results shown in Figure 3.7, which indicates that the North American model would produce the lowest χ^2 value.

	Barbados	**Sunda**	**Bonaparte**	**Total**
No 19 kyr pulse (NO PULSE)	0.75	11.35	0.8	12.15
N. American (N. AM)	0.90	7.24	0.81	8.05
Northern hemisphere (N. HEM)	0.83	8.12	0.58	8.7
European (EUR)	0.96	8.66	0.54	9.2
Antarctic (A)	0.87	10.28	0.43	10.71

Table 3.4: Same as Table 3.3 except the χ^2 values are calculated for the time period shown in Figure 3.7 only. Note all models are tuned to the Barbados sea-level record and therefore the "total" value is a sum of the χ^2 values at Bonaparte and Sunda.

This anomalous result is due to the spatial variation of the sea-level prediction across the Bonaparte Gulf data set. As mentioned in Section 3.1 the data that compose the sea-level curve in this region are from a number of cores, specifically the data following the 19 cal. kyr BP event are from a different site to those that precede it. Although there is only a small variation in the predictions across these sites (~1.5 m) this causes a significant effect when plotting the effect of a pulse is at 19 cal. kyr BP on the sea-level curve. The predictions for Bonaparte Gulf considered so far correspond to those for the pre 19 cal. kyr BP data; the predictions

corresponding to the data following the pulse are shallower. The χ^2 values in Table 3.3 already account for the spatial variation. The correct predictions for the younger data at Bonaparte Gulf are shown in the inset in Figure 3.8.

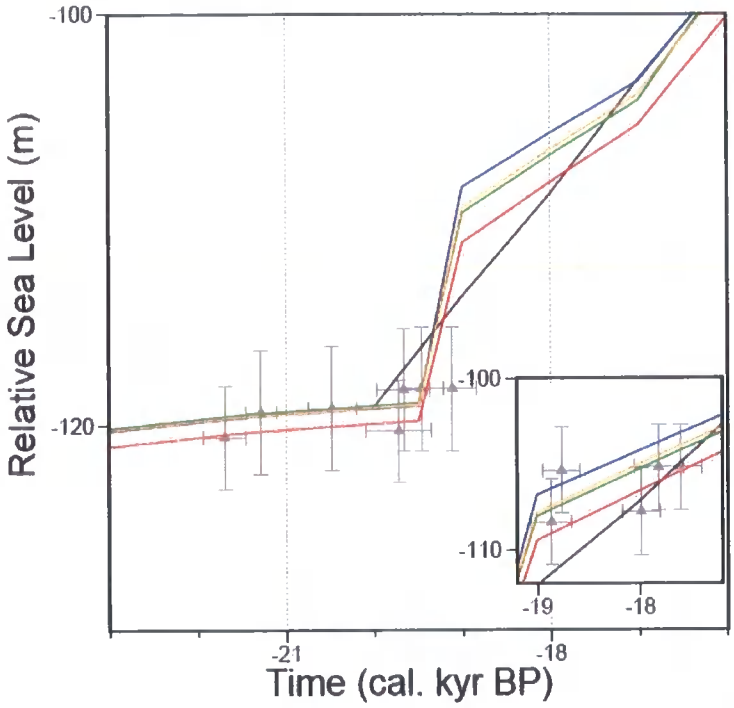

Figure 3.8: The Bonaparte Gulf data and predictions for the 19 cal. kyr BP pulse melt scenarios. The inset shows the younger data and predictions accounting for the spatial variation across the data. The predictions are: No Pulse=black, N. American=blue, Europe=green, Antarctic=red and N. hemisphere=orange.

3.5 Discussion and Summary

The results described in this chapter provide good evidence against the existence of mwp-IB: ice models which do not have any discernable mwp-IB event provide significantly improved fits to the far-field sea-level records. By extending the data to include those from the Bonaparte Gulf data, an optimum fit earth model of 4×10^{22} Pa s is obtained. The fit to the oldest data in this record supports the suggestion that the oldest Sunda Shelf data may be biased too old. Further analysis,

however, shows that an improved fit to the Bonaparte Gulf and Sunda Shelf records over the earliest part of the record can be obtained by including a pulse (~9-10 m eustatic sea-level equivalent) between 19.5 and 19 cal. kyr BP.

Of the four melt source models considered for the 19 cal. kyr BP event (North American, Eurasian, Northern hemisphere or Antarctic), primary sources from the northern hemisphere or Eurasia produced the best fit to the data. This improvement, however, is not statistically significant compared to the model which does not include a 19 cal. kyr BP event. An Antarctic source for the 19 cal. kyr BP event results in an overall deterioration of fit to the data over the whole sea-level record compared to a model with no pulse at this time. Although this deterioration in fit is not significant compared to a model with no pulse it is significantly worse than the best fit models (northern hemisphere or Eurasian source) to greater than 90 % confidence level. In contrast, if only the LGM data at Barbados, Sunda Shelf and Bonaparte Gulf are considered, an Antarctic source for the 19 cal. kyr BP event provides almost 50 % improvement of fit to the data at Bonaparte Gulf. This, however, is not statistically significant as there is a lack of data points. There can, therefore, be no conclusions drawn about the source geometry for this event based on the available data.

The limitations associated with this study include the lack of far-field sea-level records that can conclusively capture the magnitude and timing of either of the two meltwater pulses considered in this chapter. The modelling performed in Section 3.4 indicates that a number of melt scenarios are viable for the sea-level records at Barbados for the LGM period and demonstrates the requirement for more data over this time period to constrain the 19 cal. kyr BP event. Section 3.4 also demonstrates

the need to consider the spatial variation in the Bonaparte Gulf data when estimating the size of the 19 cal. kyr BP event and the fit of sea-level predictions to these observations.

Chapter 4 Near Field Sea-level Modelling of the Antarctic

4.1 Introduction

The far-field sea-level modelling carried out in Chapter 2 and Chapter 3 has been utilised to constrain the source geometry of mwp-IA showing that in order to fit the far-field observations with a single ice history and earth model a dominant, 15 m (eustatic sea-level equivalent) contribution from the Antarctic Ice sheet is required [19]. In this chapter the near-field Antarctic sea-level records are compared to a suite of predictions to test the plausibility of a 15 m Antarctic contribution to mwp-IA.

If the hypothesis of a dominant Antarctic contribution to mwp-IA is to be accepted, it must be shown to be consistent with observations and modelling that relate to the deglaciation history of the Antarctic ice sheet. The volume of ice in the Antarctic ice sheet at the LGM and the subsequent melt history has been discussed extensively in the literature (e.g. summarized in [75] and [76]). Models of the Antarctic ice sheet from glaciological, glacioisostatic and geological reconstructions have suggested contributions to the total eustatic sea-level rise of between 1-38 m from LGM to present (e.g.[12, 14, 33, 68, 75, 77-79]). With more recent research favouring the more tightly constrained range of 13-21 m (e.g. [33, 68]).

With regard to the Antarctic deglaciation history, several recent studies suggest that the East and West Antarctic components did not advance and retreat

concurrently (e.g. [12, 75, 76]). Results from Antarctic model reconstructions suggest that the major phase of Antarctic deglaciation occurred during the Holocene (e.g. [12, 14, 33]). Reconstructions from marine geological and geological data suggest, however, that this may have occurred earlier beginning at around 15 cal. kyr BP (e.g. [75, 76]). It is important to note, however, that none of these studies considered the possibility of a large contribution from Antarctica to mwp-IA.

Figure 4.1 shows the main regions of the Antarctic ice complex. The East Antarctic ice sheet is primarily cold based and is thought to have made a relatively minor contribution to post-LGM eustatic sea-level change (e.g. [33, 75]). There are components of the East Antarctic ice sheet that are less stable, such as the Lambert Glacier region, which could have made a non-negligible contribution to mwp-IA. This suggestion is supported by field evidence from this region that indicates a rapid ice retreat between 15,370-13,440 cal. yr BP [73]. In contrast, the West Antarctic ice sheet is primarily marine-based and so can respond quickly to changing climate or sea levels. Much of the mass lost from Antarctica following the LGM was sourced from the West Antarctic Ice Sheet (e.g. [33, 75]).

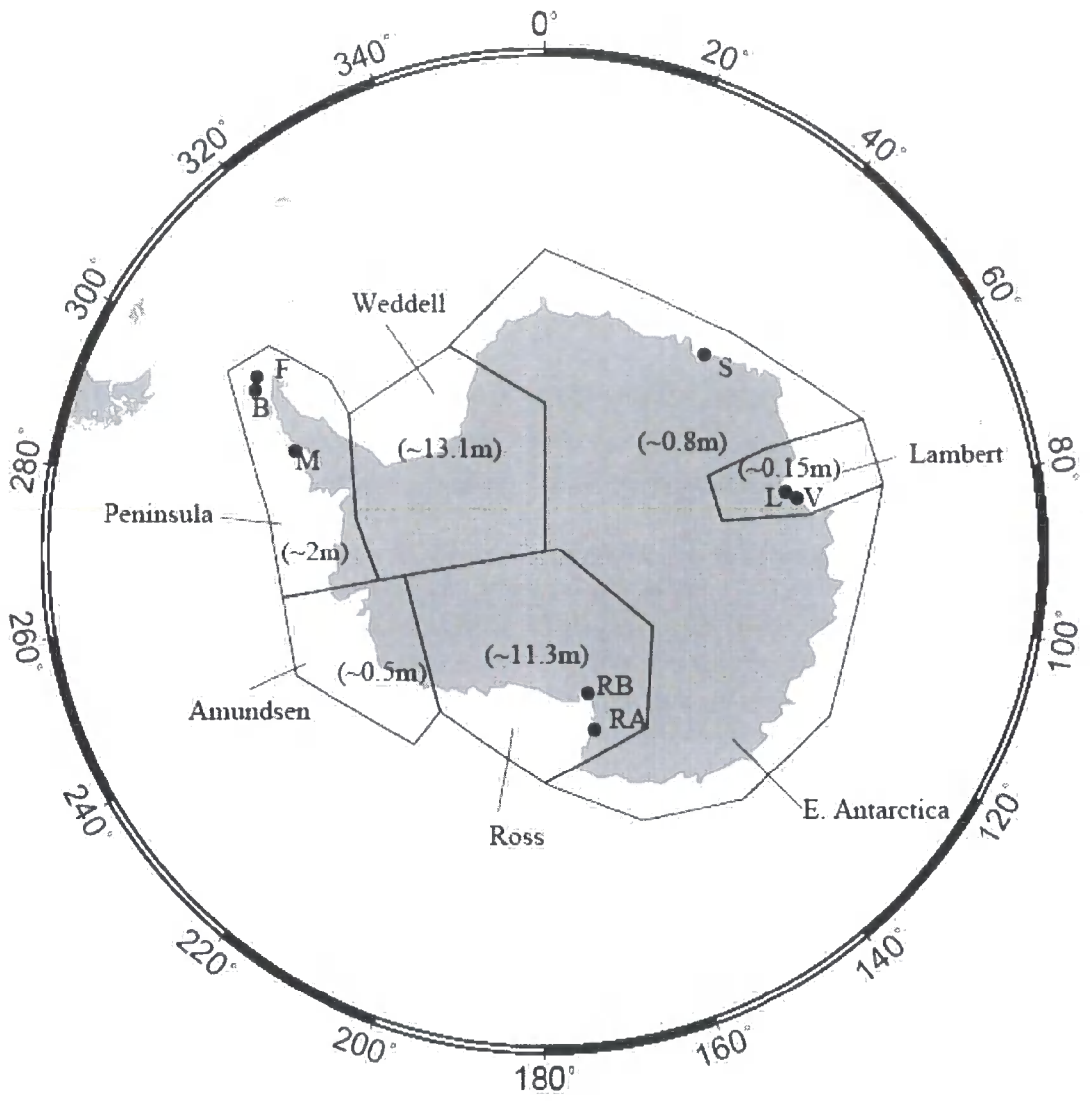

Figure 4.1: Location map for data sites used in this chapter. These are labelled as follows. F = Fildes, B = Byers, M = Marguerite Bay, S = Sôya, L = Larsemann, V = Vestfold, RA = Ross A and RB = Ross B. This map also indicates and labels the different regions of the Antarctic ice sheet referred to in the text. Each region is also labelled with the maximum eustatic sea-level contribution contained in the model. (Note that each region did not attain maximum extent at the time of the last glacial maximum.)

Of the four components of the West Antarctic ice sheet shown in Figure 4.1 (Weddell, Peninsula, Amundsen and Ross), the Ross and Weddell components are believed to have lost the most mass since the LGM and so are most likely to be the primary mwp-IA source regions. The examination of glacio-geological data in the Ross Sea, however, suggests a gradual ice retreat largely during the Holocene, with

little indication of a significant contribution (< 1 m) to mwp-IA [80, 81]. Glacio-geological data for the Weddell Sea region remain inconclusive as to the volume and melt history of this region (e.g. [76, 82]).

In this study, our main aim is to determine whether the available near-field Antarctic sea-level data preclude the possibility of a significant southern contribution to mwp-IA. If this is found not to be the case, a secondary aim is to determine whether the data can be used to infer the components of the ice sheet that were the most likely contributors to mwp-IA. In Section 4.2 the sea-level data employed in the modelling analysis are reviewed and in Section 4.3 the ability of the data to test the veracity of a number of different deglaciation scenarios and Earth model parameters is considered.

4.2 Observational Data

The sea-level data sets used are from eight locations on the Antarctic continent (Figure 4.1) and cover the period 12-0 calibrated kyr before present (cal. kyr BP). The data have been derived from the Antarctic Glaciological Geological Database [83] along with a number of additional, recently published papers not within the database. The model predictions are generated in cal. kyr BP and so wherever necessary radiocarbon dates have been converted to calibrated dates using the CALIB 5.0.1 program [45, 84]. The various data sets are described in detail below and illustrated in Figure 4.2.

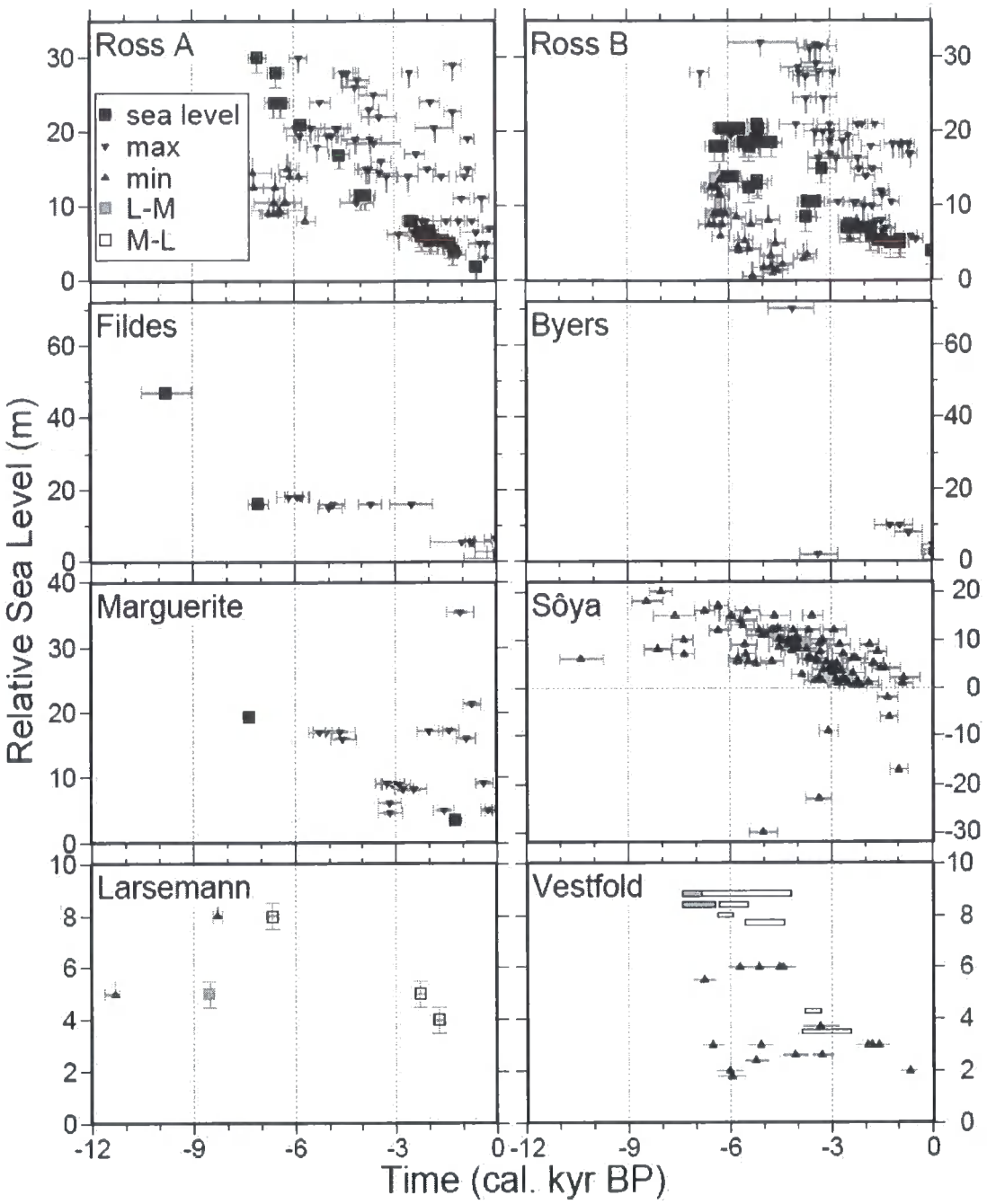

Figure 4.2: Sea-level observations at the eight sites shown in Figure 4.1 and discussed in detail in Section 4.2. The key in the Ross A frame describes the type of sea-level indicator used. Isolation basin indicators are labelled as either lacustrine to marine (L-M) or marine to lacustrine (M-L).

The sea-level reconstructions have been derived from radiocarbon dating of samples of penguin guano and remains, shells, seaweed, seal skin and isolation basins. Isolation basins are coastal inlets or basins that become cut off from the sea as relative sea-level (RSL) falls, or are flooded by seawater as RSL rises. If these

basins have freshwater input, the sedimentary record will show a change from marine to lacustrine environments for RSL fall; the reverse occurs during RSL rise. Dating the transition from marine to lacustrine sediments and measuring the height of the sill that formerly connected the lake to the ocean enables an accurate determination of mean sea-level at the time the basin became isolated. Vertical errors associated with determining sill heights are usually within ± 0.05 m. The Ross Sea RSL curves are relatively unusual in being compiled partly from dates on seal skin: following Hall and Denton [85], the seal skin fragments preserved under beach cobbles are interpreted as providing close dates for the age of the beach. Modern storm beaches can reach about 4 m above mean sea-level in the Ross Sea region [85, 86]. To allow for storm beach variation with time the altitude of beach ages are plotted with an error of ± 2m.

All other sample types provide either minimum or maximum sea-level information. For example, past sea level is interpreted to have been above shells such as *Laternula elliptica* and *Adamussium colbecki* found *in situ* within marine sediment and so they are interpreted as minimum sea level constraints. For shells, the vertical errors on Figure 4.2 reflect the uncertainties associated with depth of habitation relative to mean sea level and tidal ranges: both of the species used are found at a range of depths today and the errors in Figure 4.2 represent the minimum sea level error (depth of 1-2 m required for these species to exist).

Maximum sea-level constraints come from seal hairs, penguin guano and remains in ornithogenic soils and wind blown deposits resting on top of marine deposits. All of these are interpreted to have been deposited above sea level. Elevation errors associated with penguin remains reflect the fact that penguins

colonies occur at some height (usually > 2m) above contemporary sea level.

The errors in the date of the index points are derived from radiocarbon analyses, correction for marine reservoirs, and the calibration of these data. Radiocarbon data from carbonate shells have been corrected for a general marine reservoir effect of 1300±100 yr [87, 88].

The data for the Ross Sea have been obtained from the Terra Nova Bay (Ross A in Figure 4.2) and Southern Victoria Land Coast (Ross B in Figure 4.2) regions of the Ross Sea [89, 90]. Most sea level data here derive from penguin remains (maxima), shells (minima) and seal skin (close ages). These two datasets arguably comprise the best-constrained RSL data in Antarctica. [85, 89].

The data from the South Shetland Islands have been split into two groups to account for the spatial variation in the sea-level predictions that occurs across this region: Fildes Peninsula (King George Island) and Byers Peninsula (Livingston Island) (Figure 4.1). The data are from organic remains (e.g. penguin, whale and seal bones) that provide sea-level maxima and from isolation basins which provide accurate height constraints on past sea levels ([91] and references therein).

Marguerite Bay sea-level index points were determined from isolation basins on Horseshoe Island [92] and Pourquoi Pas Island [91]. Dates from penguin remains and guano provide maximum constraints on sea-level [91, 93] whilst other dates came from seal hair and a penguin feather buried in beaches.

The data from the Sôya coast are almost exclusively derived from marine shells which provide sea-level minima (these species require at least 1-2 m of water to exist). The data plotted here come from a series of Japanese expeditions to the Lützow-Holm Bay region of Enderby Land, and are from the youngest (Holocene)

group within a set of several hundred ages ranging up to >40 ka. Given some widely-known but poorly understood problems with radiocarbon dating of marine fossils [87, 88] there have been some independent tests of these shell dates using Electron Spin Resonance [94]. These have shown that some of the radiocarbon ages for shells may be problematic although it is not clear if this problem applies equally to the younger (Holocene) dates as it does to the older dates in the Sôya region.

The data points from the Larsemann Hills are derived from three isolation basins in the Lambert Glacier-Amery Ice Shelf system [73]. Although geographically close to the Larsemann Hills, the sea-level observations from the Vestfold Hills are significantly displaced to those obtained from the Larsemann Hills area and so have been plotted on a separate sea-level curve for the purpose of this study. The data are from sediment cores from isolation basins [95] and sea-level minima are provided by shells found *in situ* within marine sediments [96].

4.3 Modelling

Sea-level predictions are computed by solving the revised sea-level equation described in Section 0. Recent advances in sea-level modelling, such as perturbations to the rotation vector, time-varying shorelines, and an accurate treatment of sea-level change in regions of ablating marine-based ice are therefore incorporated in the predictions described below. The two variable inputs to the sea-level algorithm are the earth and the ice history models.

As in previous chapters the radial elastic and density structure of the earth model is based on the seismically inferred PREM [41] and is depth parameterised

into 25 km thick shells. The radial viscosity structure is more crudely parameterised into an upper region of effectively infinite viscosity to simulate an elastic lithosphere, and two deeper regions, each with a uniform viscosity, that correspond to the sub-lithospheric upper mantle and the lower mantle (below 670 km). These three parameters are varied in the modelling analysis. It is convenient to define a preferred, or reference, viscosity model. The results of the previous two chapters on far-field sea-level modelling indicate a high viscosity lower mantle model is preferred, however in order to perform a complete sensitivity analysis on the near-field observations this is not assumed to be the case. The reference model is chosen as a 96 km thick elastic lithosphere and viscosities of 0.5×10^{21} Pa s for the upper mantle and 10^{22} Pa s for the lower mantle region. These parameters are broadly consistent with the results of a number of recent viscosity inferences (e.g. [10, 11, 59, 62-66]).

4.3.1 Input Ice Histories

The ice histories utilised in this study were derived by combining the northern hemisphere model based on the ICE-3G reconstruction (see Section 2.3 and [14, 19]) with a model of Antarctic ice sheet evolution output from a realistic, thermomechanical glaciological model (e.g. [33]). As described below, these two components of the ice model were altered in order to test a range of mwp-IA source geometries. For each combination considered, the North American component of the northern hemisphere model was altered to provide a good fit to the Barbados sea-level record in order to ensure that the eustatic component of the hybrid ice model was accurate (as described in Section 2.3.2).

The Antarctic component of the global model used was derived from a realistic glaciological simulation using the three-dimensional thermomechanical model developed by Huybrechts [33]. The simulation, which was run on a high resolution (20 km) grid, computes the evolution of the Antarctic ice sheet in response to a series of forcing factors. These factors include climatic conditions such as sea-level, surface temperature, snow accumulation and ice ablation. As described below, the original simulation is altered to examine a small range of mwp-IA source scenarios. In the original simulation, the maximum extent of the Antarctic ice sheet is attained around 10 cal. kyr BP and the primary component of deglaciation occurs relatively late between 6 and 4 cal. kyr BP contributing ~17 m to eustatic sea level. This total contribution is comprised of ~7.2 m from the Ross Sea region, ~9.3 m from Weddell Sea, ~0.3 m from the Peninsula, ~0.15 m from each of the Lambert Glacier and Amundsen Sea regions. The contribution of this model to post-LGM eustatic sea-level rise is ~22 m.

4.3.2 Sensitivity of Predictions to Antarctic versus North American Source

In order to test the hypothesis of an early and rapid deglaciation of the Antarctic ice sheet, predictions based on two end member mwp-IA source scenarios to the sea-level observations described in Section 4.2 are compared. One scenario assumes that the mwp-IA event was sourced entirely from the northern hemisphere and primarily from the North American ice complex (eustatic components of ~26 m from North American ice and ~2 m from other ice sheets). In order to fit the Barbados record, it was necessary to revise the Antarctic component of the ice model

so that the primary component of deglaciation occurred at the same rate as in the original simulation but 4 kyr earlier (i.e. between 10 and 8 cal. kyr BP).

The second scenario assumes a dominant contribution from the Antarctic ice sheet to mwp-IA. In this case, the main period of Antarctic deglaciation was advanced by 8.5 kyr compared to the original simulation and increased the rate of this event to provide ~17 m of eustatic sea-level contribution from the Antarctic between 14.5 and 13.5 cal. kyr BP (the regional meltwater source distribution within the Antarctic ice sheet model is given above), with ~4 m eustatic sea-level delivered post-mwp-IA. This magnitude of mwp-IA contribution is compatible with the value of 15 m inferred from observations of far-field sea-level changes during the Lateglacial period (Chapter 2 and [19]). The sea-level predictions associated with these two contrasting mwp-IA scenarios are shown in Figure 4.3. Note that predictions are shown only for the past 12 kyr since none of the data predate this time.

In order to understand the predictions it is helpful to refer to 6 distinct regions of the Antarctic ice complex: Weddell Sea, East Antarctic, Lambert Glacier, Ross Sea, Amundsen Sea and the Antarctic Peninsula (Figure 4.1). At each data site, the predicted sea-level changes will show most sensitivity to local variations in the ice model; for example, the Ross sites will be very sensitive to any change in the Ross ice sheet deglaciation. In the ice model utilised here, the Ross Sea and the Weddell Sea components are the largest contributors to the Antarctic portion of eustatic sea-level change and so sites close to these regions should exhibit the greatest sensitivity to the contrasting source scenarios described above.

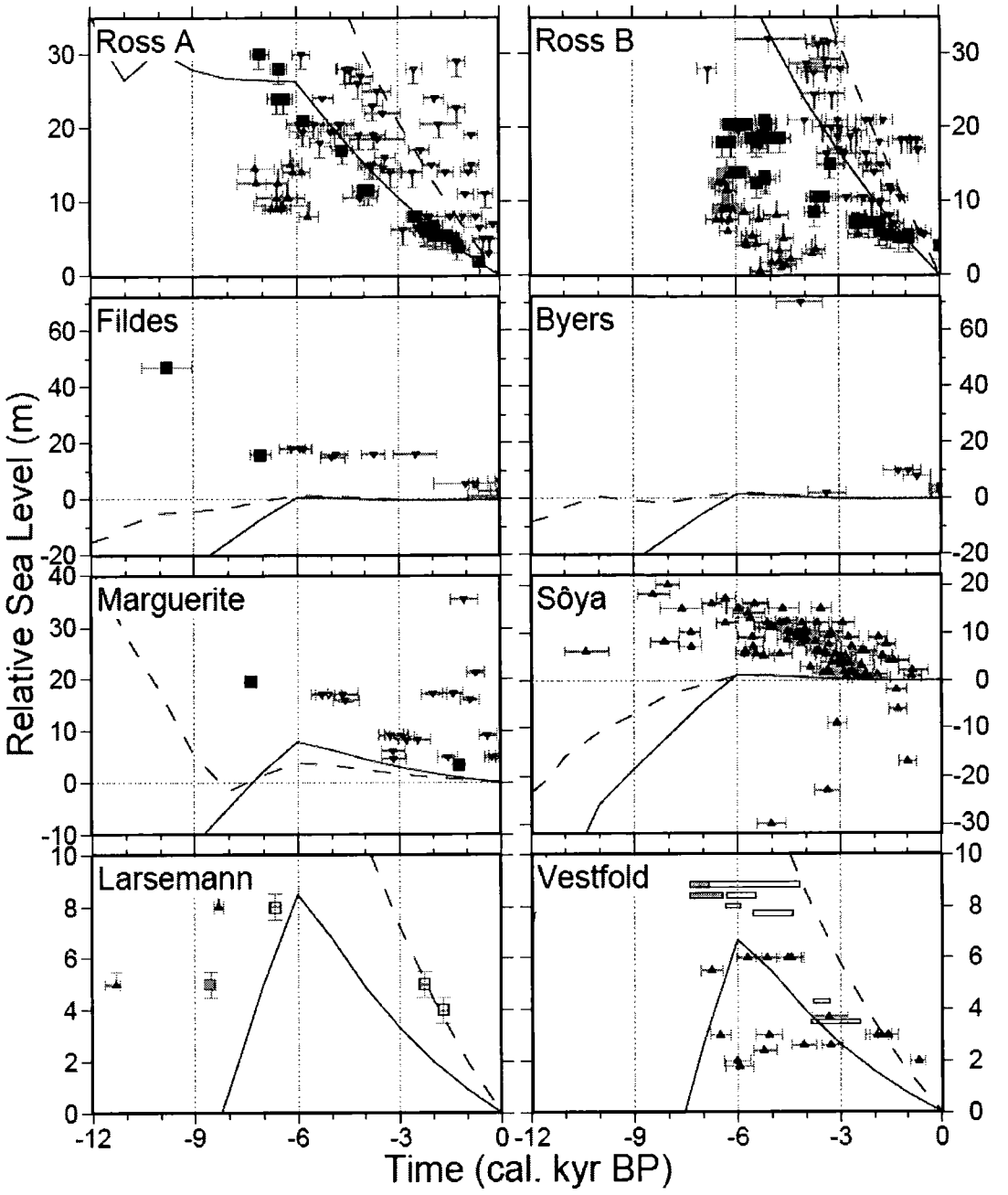

Figure 4.3: Sea-level predictions based on the reference earth model and two end member mwp-IA source scenarios: a sole northern hemisphere contribution (26 m North American ice and 2 m from other sources; dashed line) and a dominant Antarctic contribution (17 m from Antarctic ice, 2 m from North American ice and 2m from other sources; solid line). Both scenarios were tuned to fit the Barbados sea-level record. The difference in the total eustatic contribution for each scenario is a result of the distinct spatial variation, or sea-level "fingerprint", associated with the model [28].

Most regions show a significant change in the predictions depending on whether a North American (dashed line) or Antarctic (solid line) dominant source for

mwp-IA is considered. In both sets of predictions there is a distinct change in the form of the curves at 6 cal. kyr BP. This is exhibited either as a highstand (e.g. the solid black line at Marguerite, Larsemann and Vestfold) or as a change in gradient or levelling off (e.g. Fildes and Byers). This is a result of the cessation of northern hemisphere deglaciation in the adopted ice model at this time.

In the dominant Antarctic source model the Ross Sea deglaciates earlier and more rapidly than in the northern hemisphere source model. At the Ross Sea sites, there is a sea-level rise associated with the northern hemisphere melting until this region deglaciates, after which there is a sea-level fall resulting from the isostatic uplift. The combined effect of these two processes is a sea-level highstand, which occurs earlier in the Antarctic source model (around 15 cal. kyr BP) and thus results in a shallower sea-level fall for this model over the time period covered by the data. At the site Ross A, the Antarctic source model shows a distinct sea-level rise at 11-10 cal. kyr BP. This corresponds to an increase in the eustatic component of the North American ice history in order to fit the Barbados record.

There is little difference between the two predictions at the Fildes and Byers sites after 6 cal. kyr BP. The difference in the predictions prior to this time is primarily associated with ice melt in the Peninsula region. In the Antarctic source model this occurs around the time of the pulse which results in a small sea-level fall around 14 cal. kyr BP associated with the isostatic uplift of the region. In the North American source model this occurs much later, around 10 cal. kyr BP, and is illustrated by the deflection in the dashed line at these sites. The effect is much less noticeable in the North American model due to the unloading occurring over a longer time and during a period of more rapid eustatic rise. Both sets of model predictions

for the South Shetland Islands data (Fildes and Byers) fall significantly below the observations. This suggests that the modelled ice unloading in this area is too small to create the signal required by the data.

The Sôya Coast data indicate that the sea-level should fall at this site for the past 7 kyr from around 20 m. This is clearly not captured by either model prediction. In both of the adopted source models, there is relatively little ice volume change in the East Antarctic and so the dominant component of the signal at this site is the eustatic sea-level rise. The difference between the two predictions is predominantly related to the difference in the eustatic sea-level curves between the two ice models.

The Marguerite Bay predictions are more complex, reflecting the proximity of this site to both the Antarctic Peninsula and Weddell Sea ice masses. The model predictions are vastly different prior to 8 cal. kyr BP. In the northern hemisphere source model the Peninsula and Weddell Sea regions begin to deglaciate around 12 cal. kyr BP and 10 cal. kyr BP, respectively. The result of this is an extended fall in sea-level, from 12 to 8 cal. kyr BP, following a rise associated with northern hemisphere melting. In the Antarctic source model, this period of sea- level fall is subsequent to the mwp-IA event and so the rate of uplift reduces significantly by around 10 cal. kyr BP, leading to a eustatic-dominated sea-level rise during the early Holocene.

Although only a small contributor to the eustatic sea-level signal, the timing of deglaciation in the Lambert glacier region has a dramatic effect on the sea-level predictions at Larsemann and Vestfold. In the northern source model, this occurs at ~10 cal. kyr BP and results in a sea-level highstand (around 25-30 m) at this time. This highstand marks the transition from a eustatic-dominated sea-level rise to an

isostatic-dominated (local) sea-level fall. In the Antarctic source model, most of this region deglaciates at the time of mwp-IA and so pushes the isostatic-induced sea-level fall much earlier. The isostatic component of the signal has sufficiently relaxed by ~10 cal. kyr BP so that the eustatic rise dominates the predicted signal until the cessation of rapid melting in our northern hemisphere ice model. Note that there is a slightly greater isostatic response to the modelled deglaciation of this region at the Larsemann site.

In summary, the Antarctic source model (solid line) provides a better fit to the sea-level observations at most localities and so, based on these preliminary comparisons, the observations do not rule out a dominant Antarctic source to mwp-IA. Furthermore, the largest data-model discrepancies, at Sôya, Fildes and Byers, appear to be associated with an underestimate in the model of the LGM ice volume in these regions.

4.3.3 Sensitivity of Predictions to Earth Viscosity Structure

In the following we extend the above results to further test the validity of the Antarctic source hypothesis by exploring the influence of changing the mantle viscosity structure on the predictions shown in Figure 4.3. For each earth viscosity model considered, the North American ice history was scaled to maintain an accurate fit to the Barbados sea-level history. We considered the following parameter ranges in Figure 4.4-Figure 4.6: lithospheric thickness (71 – 120 km) (Figure 4.4), upper mantle viscosity (1 – 10 $\times$ 10^{20} Pa s) (Figure 4.5) and lower mantle viscosity (1 – 40 $\times$ 10^{21} Pa s) (Figure 4.6). These ranges are quite broad and so most likely include the values that reflect the true volume averaged viscosity structure of the Antarctic

region (e.g. [79, 97]).

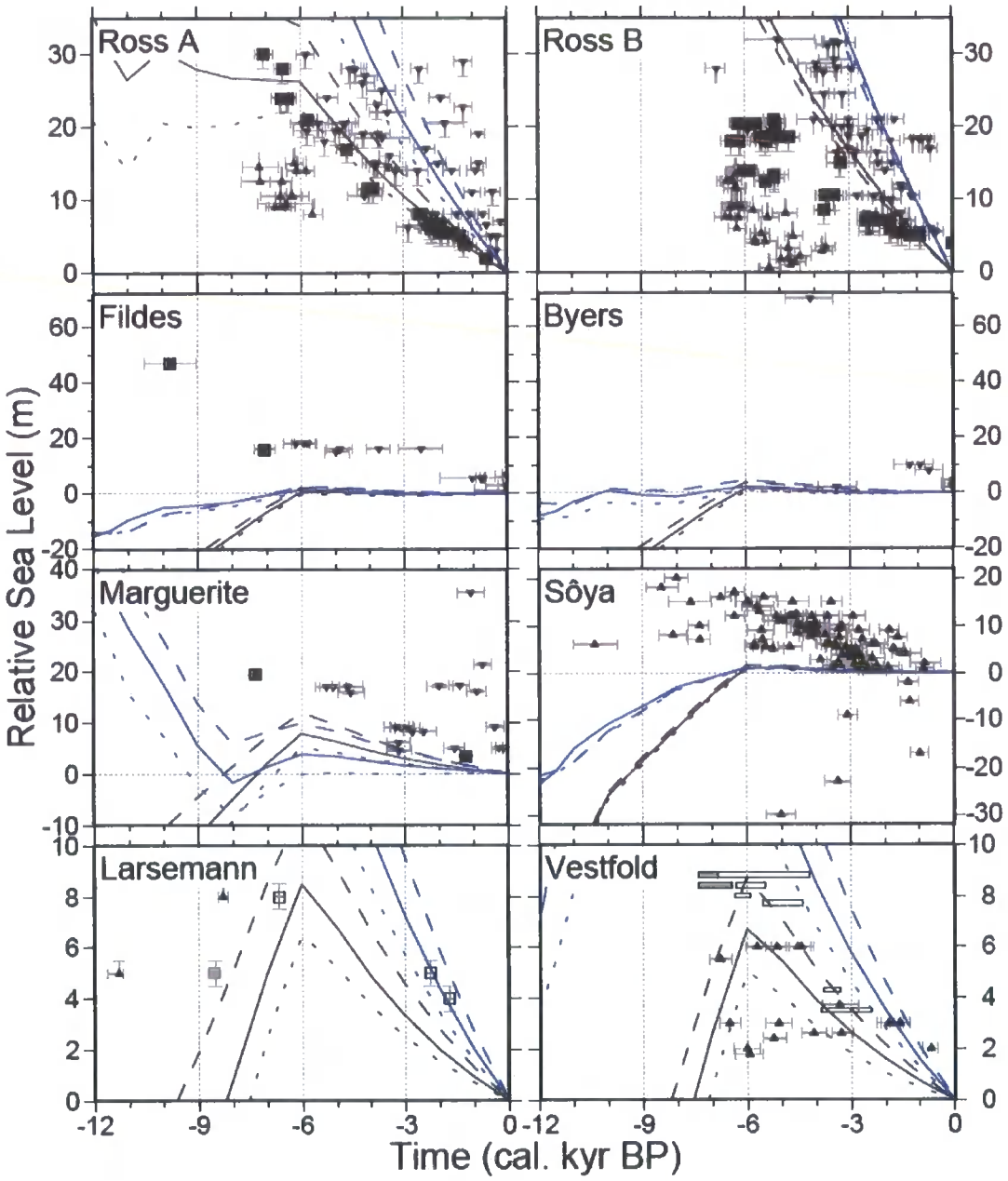

Figure 4.4: Sea-level predictions based on the sole northern hemisphere (blue lines) and dominant Antarctic (black lines) mwp-IA scenarios shown in Figure 4.3 for the reference earth model (solid line) and two other earth models that are the same as the reference earth model except that the lithospheric thickness is increased to 120 km (dotted line) or decreased to 71 km (dashed line).

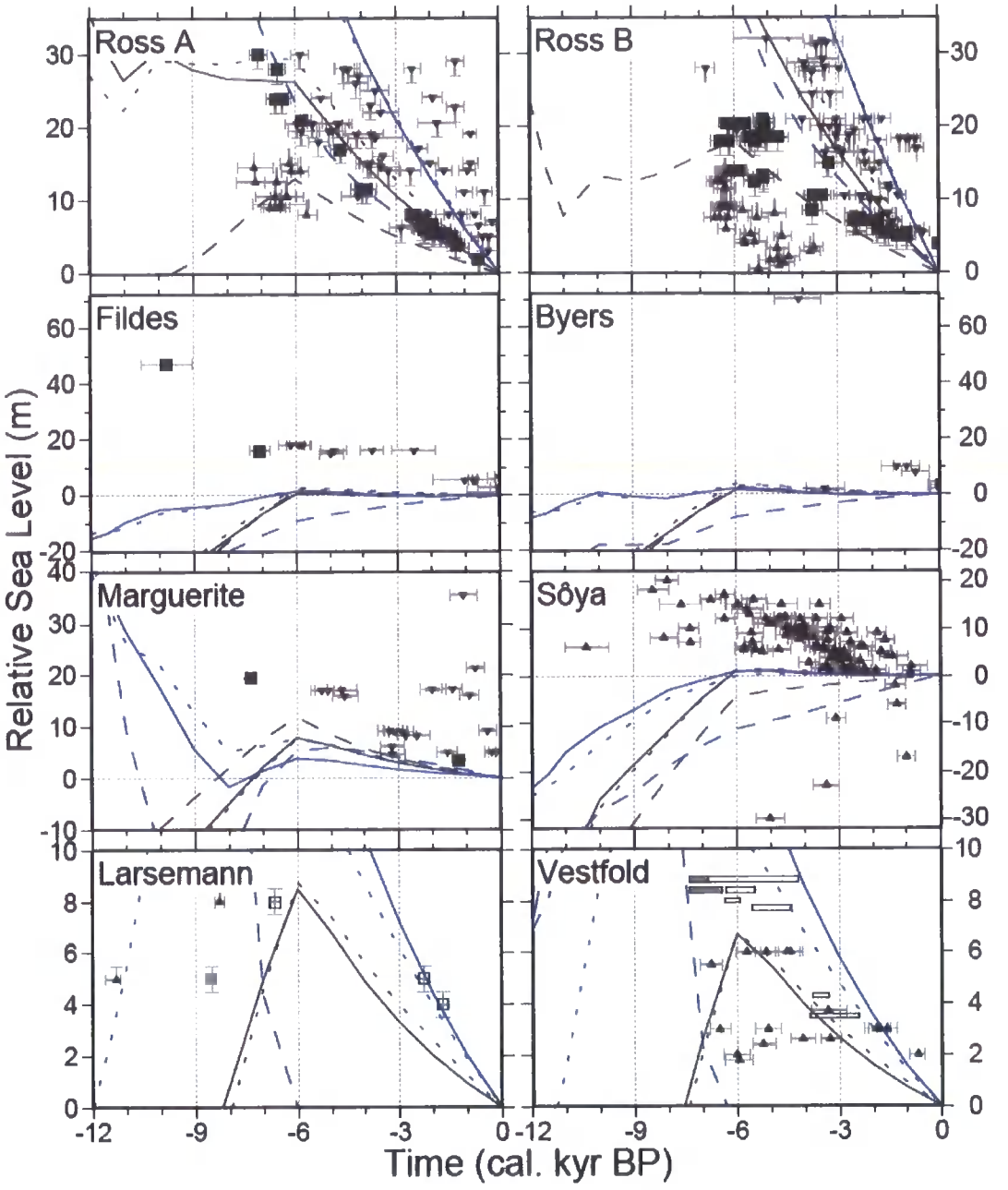

Figure 4.5: The same as Figure 4.4 except that the upper mantle viscosity is increased to 10^{21} Pa s (dotted line) or decreased to 10^{20} Pa s (dashed line) relative to the reference model (solid line).

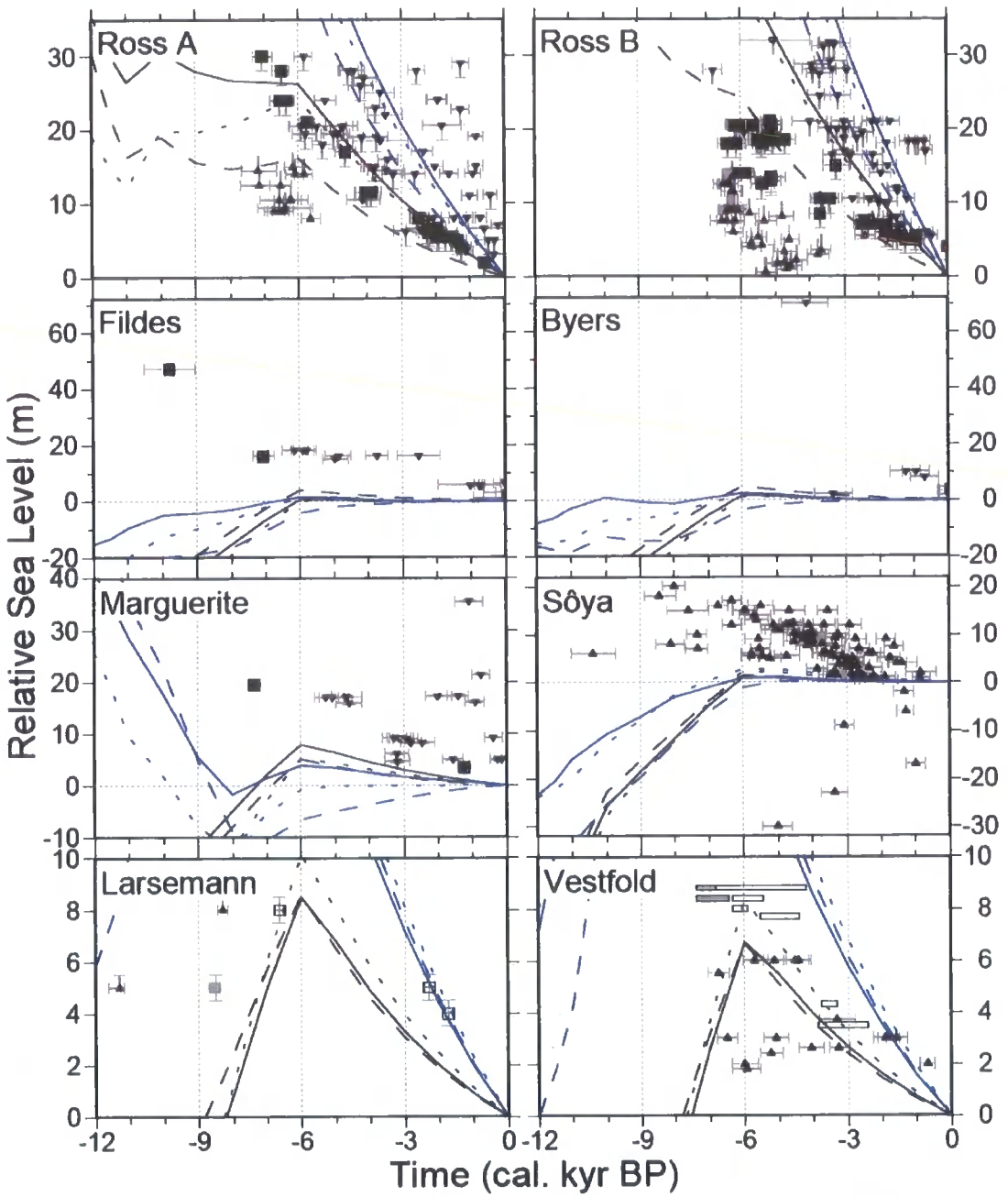

Figure 4.6: The same as Figure 4.4 except that the lower mantle viscosity is increased to 4 x 10^{22} Pa s (dotted line) or decreased to 10^{21} Pa s (dashed line) compared to the reference model (solid line).

Of the eight sites considered, the predictions at Fildes, Byers and Sôya are least sensitive to variations in the viscosity structure. This is directly related to the adopted ice model, which exhibits relatively little deglaciation at these localities. The increased sensitivity at these sites to variations in deeper structure (as opposed to lithospheric thickness variations) is driven by ice sheet changes in other regions. In

contrast, the greatest sensitivity is found at the remaining five sites which are in close proximity to components of the ice model that show larger changes during deglaciation.

At most sites, increasing or decreasing the lithospheric thickness acts to, respectively, decrease or increase the magnitude of the isostatic response (compare dashed and dotted lines in Figure 4.4). For the range of lithospheric thickness values explored in Figure 4.4, the predictions based on the Antarctic source model (black lines) are more compatible with the observations.

The greatest sensitivity to earth model structure is shown for the range of upper mantle viscosity values considered (Figure 4.5). This is particularly noticeable at Larsemann and Vestfold where the earth model with the lowest upper mantle viscosity (dashed lines) responds very rapidly to the unloading and so produces a sharp sea-level fall. This is only visible for the northern hemisphere source model due to the time range chosen. For the Antarctic source model, the rapidity of the solid earth response results in the predictions remaining below present day sea-level for the entire period illustrated in Figure 4.5. The relative insensitivity of the predictions at Larsemann and Vestfold to the range of lower mantle viscosities considered (Figure 4.6) indicates that the spatial scale of the ice sheet changes in this region are not large enough to induce any significant deformation within the model lower mantle.

Inspection of the predictions in Figure 4.5 and Figure 4.6 shows that, of the two ice models considered, the Antarctic source model more consistently results in a better fit to the data for the range of earth models considered. We can conclude, therefore, that the Antarctic sea-level data are more compatible with the dominant

Antarctic scenario for a range of plausible 1-D earth models.

Regardless of the adopted earth model or ice model, the quality of data-model fit at the sites Fildes, Byers and Sôya remained poor. This is further evidence to suggest that the adopted Antarctic ice model underestimates the LGM ice volume in these regions.

4.3.4 Sensitivity of Predictions to Geometry of Antarctic Source

Of the two mwp-IA source models considered above, the dominant Antarctic source scenario is clearly preferred by the observations for the range of earth models considered. Based on this result, our aim in this section is to test the sensitivity of the predictions to changing the geometry of the source within the Antarctic ice complex to determine whether it is possible to constrain the source geometry at a regional scale using the available observations. There are two components within our adopted Antarctic model which contain sufficient volume to contribute significantly to mwp-IA: the Ross Sea and Weddell Sea. The eustatic contributions from different regions of the ice model are shown in Figure 4.1. These values correspond to the eustatic sea-level contribution associated with the maximum glacial extent of each region considered in the figure, which, for most regions, does not coincide with the ice extent at the time of the global glacial maximum (~20 cal. kyr BP).

The Ross Sea and Weddell Sea components of the ice model contain, respectively, ~11 m and ~13 m of eustatic sea level. We have tested three different mwp-IA scenarios for this preliminary study: a sole Ross or Weddell source and a combined Ross and Weddell source (~5 m and ~9 m, respectively). All of the

predictions shown are based on the reference Earth viscosity model, which provided the best fits to the data for a dominant Antarctic source model. The results of these computations are shown in Figure 4.7. As discussed above, for each ice model considered, the volume of North American ice was altered to ensure that a good fit was maintained at Barbados. Although a large Ross component to mwp-IA has been argued against on the basis of geological evidence (e.g. [81]), it has been included here to be compatible with the model adopted in the previous two sections and to make our sensitivity analysis more complete.

As expected, the sole Ross Sea model significantly alters the predictions at Ross A and Ross B. There is however little difference between the scenario in which the Ross Sea is the main contributor (dashed line) compared to that in which it is only a partial contributor (black line), indicating that the predictions are relatively unaffected by the activity in the Weddell Sea for this time period. In both models that consider a proportion of Ross melt, the isostatic uplift occurs sufficiently early to result in a shallower sea-level fall compared to the predictions based on the northern hemisphere source model (see Figure 4.3), in which this region deglaciates much later (10-8 cal. kyr BP). The Weddell Sea model produces a fit which is similar to our northern hemisphere source model, indicating that the predicted sea-level response in the Ross Sea region is relatively insensitive to the timing and magnitude of deglaciation in the Weddell Sea. These results for the Ross Sea region suggest that: (i) either the adopted Antarctic ice model overestimates the ice volume in this region (particularly Ross B); (ii) that this region must have deglaciated early (as in the Antarctic source model) or (iii) a combination of (i) and (ii).

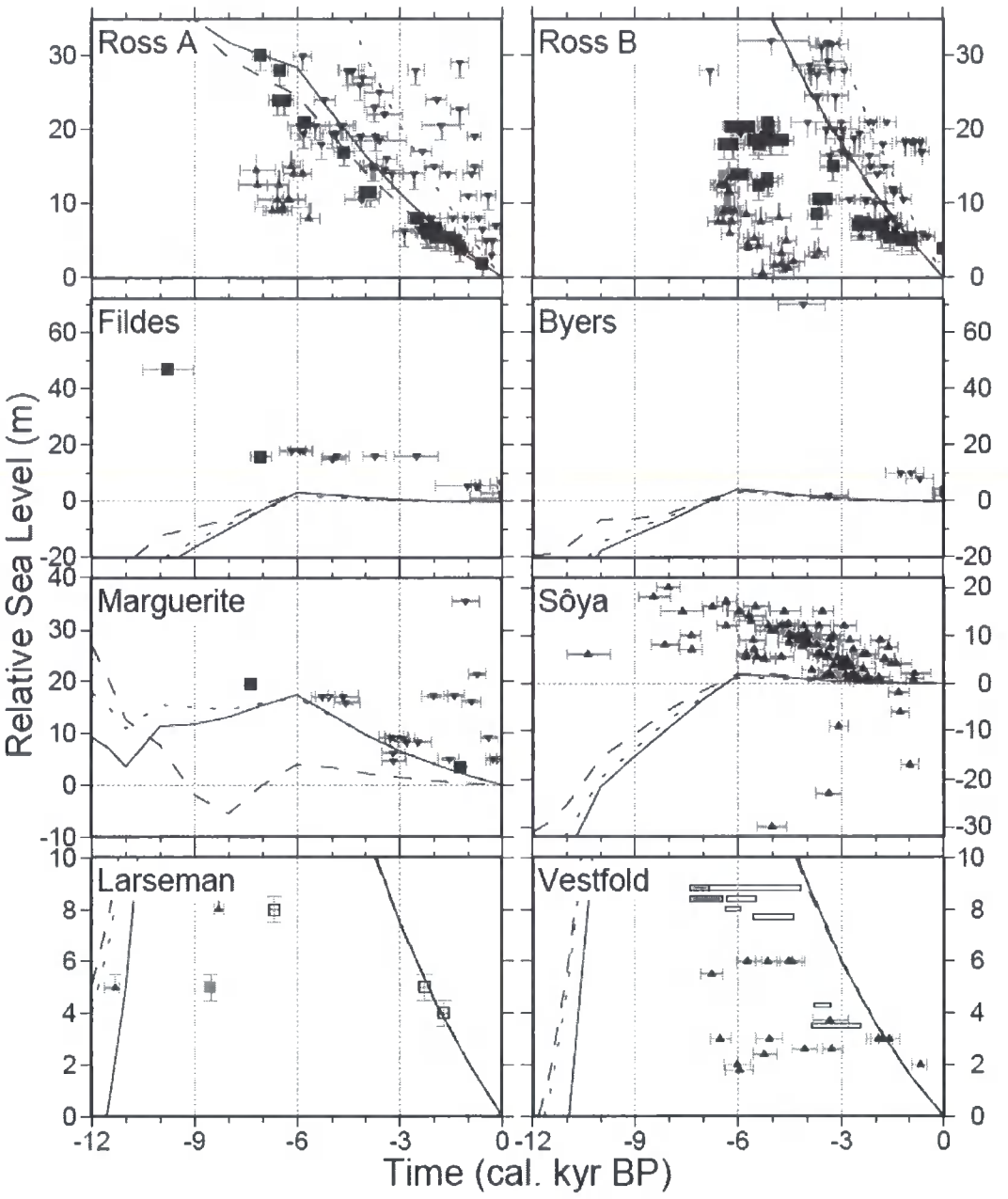

Figure 4.7: Sea-level predictions based on the reference earth model and three different models of Antarctic mwp-IA melt scenarios: Ross Sea source (dashed line), Weddell Sea source (dotted line), combination of Weddell Sea and Ross Sea (solid line). See main text for more details.

The Marguerite Bay observations clearly prefer the scenarios that include either a dominant or partial Weddell contribution to mwp-IA. The Ross Sea dominant scenario falls significantly below the data as a result of a large sea-level fall caused by the relatively late deglaciation of the Peninsula and the Weddell Sea in this model. In the Weddell sea-models, this sea-level fall is predicted earlier and

occurs concurrently with the rapid rise in the eustatic signal. The net effect is to push the predictions higher in the Holocene, which is more consistent with the observations. Although a reasonable fit is found to the more recent data at this location, the oldest sea-level indicator is still not captured by any ice-earth model combination considered thus far. This suggests that the cause of the misfit is an inaccuracy in the eustatic component of the northern hemisphere model, which has not been calibrated to fit data in the mid to late Holocene (the latest sea-level constraint at Barbados is at 7 cal. kyr BP). This issue is explored below.

All of the regional melt models considered in this section perform badly at Larsemann and Vestfold. The fit at these sites was improved by the dominant Antarctic source scenario considered in Section 4.3.2, in which this region deglaciated at the time of mwp-IA. As for the case of the Ross Sea region, the cause of the over prediction of Holocene uplift in this region is ambiguous – it could be related to the timing of deglaciation (i.e. too late in the models considered in this section) or the magnitude of ice removal in the adopted model.

In Figure 4.8, we conclude this analysis by revising the combined Ross/Weddell scenario to include a rapid deglaciation of the Lambert Glacier region (~0.15 m eustatic equivalent) at the time of mwp-IA as well as a Northern hemisphere model in which the rate of melting dramatically reduces at 7 cal. kyr BP. Of the ice models considered in this analysis, the predictions based on this model are the most consistent with the observations. The predictions (solid lines) show a marked improvement compared to the combined Ross/Weddell model (dashed lines) at the Marguerite, Larsemann and Vestfold sites without causing a significant change at the other sites considered.

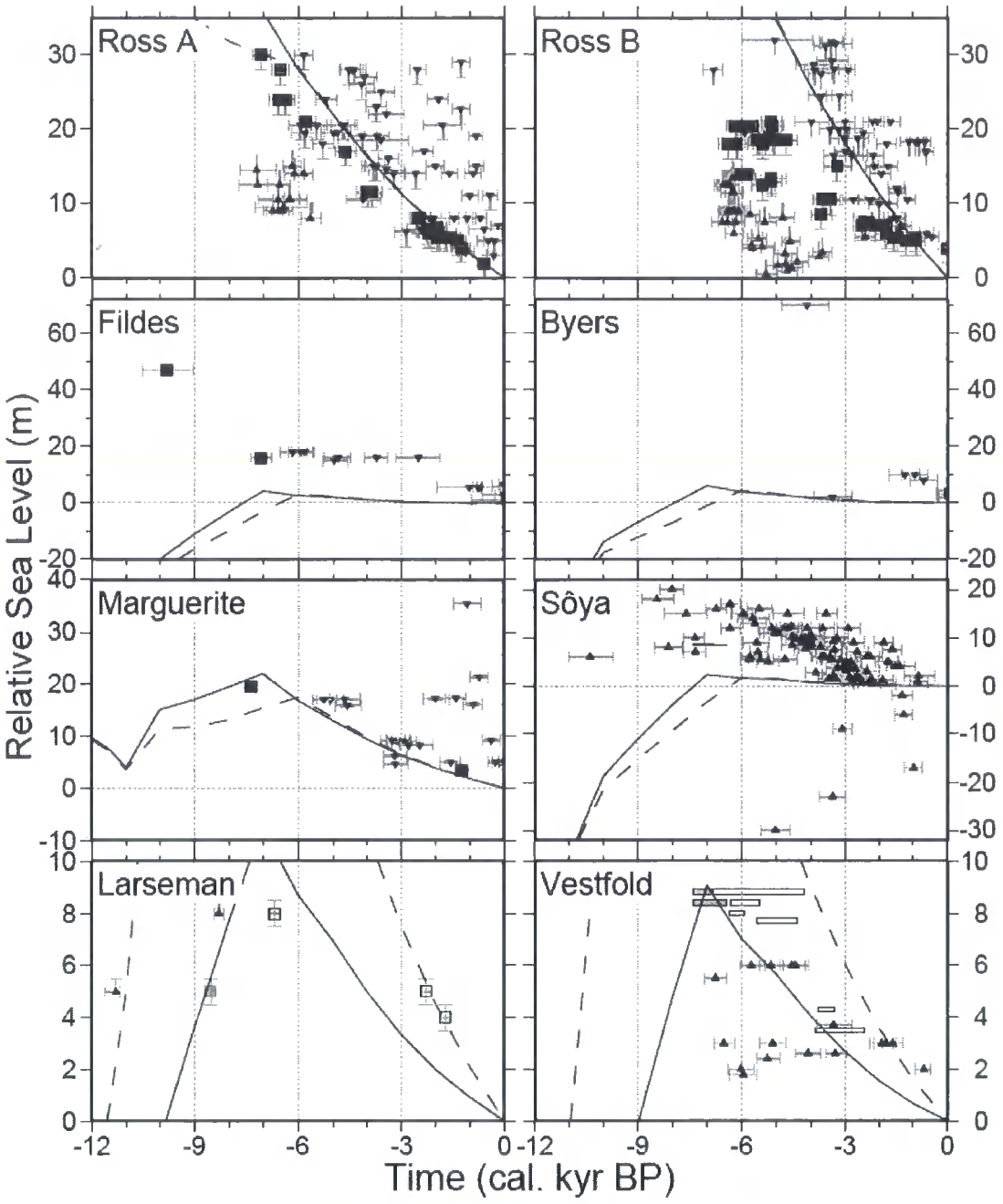

Figure 4.8: Sea-level predictions based on a revised version of the combined (Ross/Weddell) model of Figure 4.7 (dashed line). The model has been revised to include a rapid deglaciation of the Lambert Glacier region (~0.15 m eustatic) at the time of mwp-IA as well as a northern hemisphere ice history in which rapid melting is 1 kyr earlier than in our standard model. The predictions for this model are shown by the solid line.

4.4 Discussion and Summary

The above results indicate that the available sea-level data are unable to preclude the existence of a significant contribution from the Antarctic Ice Sheet to mwp-IA. The conclusion from this preliminary analysis is that, for the case of a dominant Antarctic source, most of the melt water was derived from the Weddell Sea (9 m) and the Ross Sea (5 m). This result is clearly not compatible with the field evidence that suggests the Ross Sea component of the ice sheet made a contribution of less than 1 m to mwp -IA (e.g.[81]). The total excess ice mass in the Ross Sea region of the adopted ice model is 10 m equivalent (eustatic) sea-level rise. The "best fit" model described above includes a 50% contribution from this region during mwp-IA with the remaining 50% being melted in a more gradual fashion until the mid-Holocene.

In the dominant North American source model considered in Figure 4.1 (dashed line), there is a rapid deglaciation of the Ross Sea region between 10 and 8 cal. kyr BP (this rapid change is a feature of the adopted ice model); which results in a poorer fit to the observations compared to the best fit model. The fit to the Ross Sea data may also be improved by reducing the magnitude of ice volume in this region (e.g. [12, 75, 81]). More modelling work is clearly required to investigate the sea-level response of a larger suite of Ross Sea deglaciation scenarios to determine which are consistent with the sea-level observations. Such an in-depth study of this region is beyond the scope of the present analysis.

Although a number of Earth models were investigated, the reference earth model (lithospheric thickness = 96 km, upper mantle and lower mantle viscosity = 5

x 10^{20} and 10 x 10^{21} Pa s (respectively)) provided the best fit to the data. However, as described above, regardless of the ice or Earth model adopted, there remain significant misfits to the observations from the South Shetland Islands and the Sôya coast. These discrepancies indicate that the adopted ice model, which has not been calibrated to fit any sea-level data, contains insufficient ice melt in these regions. These results are consistent with those of Nakada et al. [12], who found that the ice models they considered also under-predicted the isostatic component of the sea-level response in the Sôya Coast and Antarctic Peninsula regions. The requirement of the observations for more extensive ice in East Antarctic and the Peninsula clearly needs further exploration. Ice model changes in the Peninsula region are of particular interest given the proximity of the Marguerite Bay site and the fact that data from this site provided some of the most powerful constraints in this study.

The relatively poor spatial extent of the data and the lack of any constraints on sea-level prior to ~12 cal. kyr BP imply that there are likely to be a number of possible ice melt scenarios that could provide adequate fits to the data. The primary aim of this study was to test whether or not the available data rule out a dominant Antarctic contribution to mwp-IA, and so the issue of non-uniqueness was not explored in any depth. The analysis was based on a single Antarctic ice model and so is clearly limited in this respect. The recent Antarctic deglaciation model proposed by Ivins and James [79], which is based on field constraints and does not include an Antarctic component to mwp-IA, represents a useful alternative model that should be tested against the available sea-level observations.

The non-uniqueness problem can clearly be improved by obtaining, or improving, data from regions that are in proximity to the most likely mwp-IA source

areas. For example, new observations obtained from or closer to the Weddell Sea region would help better constrain the Weddell Sea contribution to mwp-IA. The results presented here indicate that sea-level observations prior to 7 cal. kyr BP from Marguerite Bay would provide powerful constraints with which to test deglaciation models of the Weddell Sea and Peninsula regions.

Preliminary findings from research into sediment analysis in order to determine if rapid melting events are preserved in the sediment record as peaks of ice rafted debris around the Antarctic Peninsula may provide further support for an Antarctic source for mwp-IA [98].

This study has provided useful insight into the plausibility of an Antarctic source for mwp-IA. By exploring a number of melt scenarios based on a glaciologically realistic Antarctic ice model, we have found that the data do not rule out a dominant Antarctic contribution to mwp-IA. The preliminary analysis indicates that the Weddell Sea region is the most likely source for a large Antarctic contribution to mwp-IA. The Ross Sea is also plausible as a significant contributor from a sea-level perspective, although the glaciological field evidence can be used to argue against this. The above results also show that the adopted ice model underpredicts the isostatic component of the sea-level response in the Antarctic Peninsula and the Soya Coast region of the East Antarctic ice sheet. It is plausible that ice melt from regions such as these, the Peninsula in particular, could have made a significant contribution to mwp-IA.

Chapter 5 Discussion and Summary

5.1 Summary of Key Results

The main results of each of Chapters 2, 3 and 4 have been summarised at the end of the respective chapters. This chapter will draw together these results and discuss them more generally in the context of their relevance to ongoing research.

As discussed in Section 2.3, predicting the sea-level change associated with glacio-isostatic modelling requires three primary inputs: models of global ice history and earth structure (rheology and density) and a sea-level algorithm which computes the global meltwater distribution. This thesis has utilised up-to-date methods in order to explore what conclusions can be drawn about global ice history and deep earth structure from both near and far-field sea-level records.

In Chapter 2, the Lateglacial far-field sea-level records are shown to provide a powerful constraint on the source distribution for mwp-IA and show that a substantial Antarctic contribution is a requirement of the data. The modelling results discussed show that long debated discrepancies between predictions and observations of Lateglacial sea levels at Tahiti, Huon Peninsula and Sunda Shelf can be reconciled by adopting a relatively high lower mantle viscosity and a large (~15 m eustatic sea-level equivalent) contribution to mwp-IA from the Antarctic ice sheet with the remainder of the eustatic rise across mwp-IA partitioned into ~6 m from North America and ~2 m from Eurasia. This conclusion is contrary to previous suggestions

that the discrepancy in fit is due to uncertainties in the habitation depth of coral species or errors in the tectonic corrections applied to the raw sea-level markers [13, 29, 32].

Chapter 3 refers again to the far-field sea-level records in order to ascertain if any constraints can be placed on the mwp-IB and 19 cal. kyr BP events. The most striking results shown in Section 3.2 demonstrate that a revised ice model where the mwp-IB event is not included produces a significantly improved fit to the observations at Huon and Tahiti. Thus the analysis presented here does not support the existence of mwp-IB. Incorporating a further data set from Bonaparte Gulf (see Section 3.3), in order to test the hypothesis that the LGM data from Sunda Shelf may be biased too old (see Section 2.4), provides constraints on the optimum viscosity model and also introduces a further rapid sea-level rise event, at 19 cal. kyr BP, to explore. Preliminary modelling of this 19 cal. kyr event shows that including rapid melting from a northern hemisphere source (with a significant Eurasian component) improves the overall fit. The improvement observed when this pulse is included is, however, not statistically significant and therefore no conclusions about the source of this event can be drawn until further data that capture this event become available.

Having concluded in Chapters 2 and 3 that a 15 m contribution to mwp-IA from the Antarctic is required to fit the far-field records, the focus is switched in Chapter 4 to the near-field data available from the Antarctic. By utilising a high resolution ice model [33], the results show that an Antarctic source for this event cannot be ruled out. In addition, a more detailed analysis of possible melt histories during mwp-IA suggest a dominant Weddell Sea source for this event with a component of melt from the Ross Sea. Although the far-field data prefer a high

viscosity lower mantle no such conclusions can be drawn from the results in Chapter 4 due to the more complex nature of the near-field responses to variations in earth structure (see Section 4.3.3). These results should be further tested utilising alternative ice models (e.g. [68, 79]) in order to test the robustness of these conclusions.

The work presented here clearly supports the hypothesis of Weaver et al. [3], that a partial collapse of the Antarctic ice sheet is a possible mechanism to explain both the Bølling Allerød and Younger Dryas intervals through the influence of freshwater forcing of the thermohaline circulation (see Section 1.1). More work is required to test this hypothesis further (see Section 5.2); however, if it is proven correct it represents a major advance in our understanding of the progression of events that occurred during Termination 1 and, furthermore, indicates that climatic events in the southern hemisphere acted as the trigger for northern hemisphere deglaciation.

5.2 Future Work

A primary limitation of the work presented here is the application of earth models that incorporate structure in one dimension only (depth; i.e. no lateral variations are included). This work should, therefore, be extended to encompass a 3-D earth model (e.g. [74]) to explore the significance of any lateral variations in the viscosity structure (e.g. [97]).

Future far-field modelling studies to test the existence of mwp-IB and the 19 cal. kyr event as well as providing further constraints on the exact timing, magnitude

and source geometry of mwp-IA require further data sets which sample the time period when these events occur. Results from a recent IODP (Integrated Ocean Drilling Programme) cruise to gather cores from Tahiti will, hopefully, provide an extended record of sea-level change in this region. This record can then be compared to predictions produced in Chapter 2 in order to test the robustness of the conclusions stated therein.

New sea-level records from locations around the Antarctic continent are of great importance in testing the reconstructions of the spatial and temporal evolution of the Antarctic ice sheet. The work presented in Chapter 4 gives locations where new sea-level records would provide useful information with respect to the mwp-IA source issue. In addition, space geodetic data from GPS studies and various satellite missions (e.g. GRACE and IceSat) could be combined with the relative sea-level curves to enable better constraints to be placed on the Antarctic ice history (e.g. [79, 99-101]).

Finally, it is clearly important to explore the possible mechanisms that could have triggered a large and rapid melt of the Antarctic ice sheet at the time of mwp-IA. This could be done by running various sensitivity experiments with realistic thermo-mechanical ice models.

Bibliography

1. Clark, P.U., R.B. Alley, and D. Pollard, *northern hemisphere ice sheet influences on global climate change.* Science, 1999. **286**(5442): p. 1104-1111.

2. Siegert, M.J., *Ice sheets and late Quaternary environmental change.* 2001, Chichester: John Wiley and Sons.

3. Weaver, A.J., O.A. Saenko, P.U. Clark, and J.X. Mitrovica, *Meltwater pulse 1A from Antarctica as a trigger of the Bølling Allerød warm interval.* Science, 2003. **299**(5613): p. 1709-1713.

4. Clark, P.U., R.B. Alley, L.D. Keigwin, L.D. Licciardi, J.M. Johnsen, and S.J. Wang, *Origin of the first global meltwater pulse following the last glacial maximum.* Paleoceanography, 1996. **11**(5): p. 563-577.

5. Ruddiman, W.F., *Earth's Climate Past and Future.* 2001, New York: W. H. Freeman and Company.

6. Farrell, W.E. and J.A. Clark, *On postglacial sea level.* Geophysical Journal of the Royal Astronomical Society, 1976. **46**: p. 647-667.

7. Clark, J.A., W.E. Farrell, and W.R. Peltier, *Global changes in postglacial sea level: a numerical calculation.* Quaternary Science Reviews, 1978. **9**: p. 265-287.

8. Kaufmann, G., *The onset of Pleistoscene glaciation in the Barents Sea: implications for glacial isostatic adjustment.* Geophysical Journal International, 1997. **131**: p. 281-292.

9. Lambeck, K., *Constraints in the late Wiechselian ice sheet over the Barents Sea from observations of raised shorelines.* Quaternary Science Reviews, 1995. **14**: p. 1-16.

10. Lambeck, K., C. Smither, and P. Johnstin, *Sea-level change, glacial rebound and mantle viscosity for northern Europe.* Geophysical Journal International, 1998. **134**: p. 102-144.

11. Mitrovica, J.X. and A.M. Forte, *The radial profile of mantle viscosity: results*

from the joint inversion of convection and post-glacial rebound observables. Journal of Geophysical Research, 1997. **102**: p. 2751-2769.

12. Nakada, M., R. Kimura, J. Okuno, K. Moriwaki, H. Miura, and H. Maemoku, *Late Pleistoscene and Holocene melting history of the Antarctic ice sheet derived from sea-level observations.* Marine Geology, 2000. **167**: p. 85-103.

13. Peltier, W.R., *On eustatic sea-level history: Last Glacial Maximum to Holocene.* Quaternary Science Reviews, 2002. **21**: p. 377-396.

14. Tushingham, A.M. and W.R. Peltier, *Ice-3g - a new global-model of late Pleistocene deglaciation based upon geophysical predictions of postglacial relative sea-level change.* Journal of Geophysical Research-Solid Earth and Planets, 1991. **96**(B3): p. 4497-4523.

15. Clark, P.U. and A.C. Mix, *Ice sheets and sea level of the Last Glacial Maximum.* Quaternary Science Reviews, 2002. **21**: p. 1-7.

16. Lambeck, K., Y. Yokoyama, and T. Purcell, *Into and out of the Last Glacial Maximum: sea-level change during oxygen isotope stages 3 and 2.* Quaternary Science Reviews, 2002. **21**: p. 343-360.

17. Milne, G.A., J.X. Mitrovica, and D.P. Schrag, *Estimating past continental ice volume from sea-level data.* Quaternary Science Reviews, 2002. **21**: p. 361-376.

18. Shennan, I., W.R. Peltier, R. Drummond, and B. Horton, *Global to local scale parameters determining relative sea-level changes and the post-glacial isostatic adjustment of Great Britain.* Quaternary Science Reviews, 2002. **21**: p. 397-409.

19. Bassett, S.E., G.A. Milne, J.X. Mitrovica, and P.U. Clark, *Ice sheet and solid earth influences on far-field sea-level histories.* Science, 2005. **309**(5736): p. 925-928.

20. Fairbanks, R.G., *A 17,000 year glacio-eustatic sea-level record: influence of glacial melting rates on the Younger Dryas event and deep ocean circulation.* Nature, 1989. **342**: p. 637-642.

21. Yokoyama, Y., K. Lambeck, P. De Deckker, P. Johnston, and L.K. Fifield,

Timing of the Last Glacial Maximum from observed sea-level minima. Nature, 2000. **406**: p. 713-716.

22. Hanebuth, T., K. Stattegger, and M. Pieter, *Rapid Flooding of the Sunda Shelf: A late-glacial sea-level record.* Science, 2000. **288**(5468): p. 1033-1035.

23. Chappell, J. and H. Polach, *Post-glacial sea-level rise from a coral record at Huon Peninsula, Papua New Guinea.* Nature, 1991. **349**: p. 147-149.

24. Bard, E., B. Hamelin, M. Arnold, L.F. Montaggioni, G. Cabioch, G. Faure, and F. Rougerie, *Deglacial sea-level record from the Tahiti corals and the timing of the global meltwater discharge.* Nature, 1996. **382**: p. 241-244.

25. Shennan, I., M.J. Tooley, F.M.L. Green, J.B. Innes, K. Kennington, J.M. Lloyd, and M.M. Rutherford, *Sea level, climate change and coastal evolution in Morar, northwest Scotland.* Geologie en Mijnbouw, 1999. **77**: p. 247-262.

26. Shennan, I. and G.A. Milne, *Sea-level observations around the Last Glacial Maximum from the Bonaparte Gulf, NW Australia.* Quaternary Science Reviews, 2003. **22**: p. 1543-1547.

27. Clark, P.U., A. McCabe, A. Marshall, A.C. Mix, and A.J. Weaver, *Rapid rise of sea level 19,000 years ago and its global implications.* Science, 2004. **304**(5674): p. 1141-1144.

28. Clark, P.U., J.X. Mitrovica, G.A. Milne, and M.E. Tamisiea, *Sea level fingerprinting as a direct test for the source of global meltwater pulse IA.* Science, 2002. **295**(5564): p. 2438-2441.

29. Peltier, W.R., *On the hemispheric origins of meltwater pulse 1a.* Quaternary Science Reviews, 2005. **24**(14-15): p. 1655-1671.

30. Mitrovica, J.X., M.E. Tamisiea, J.L. Davis, and G.A. Milne, *Recent mass balance of polar ice sheets inferred from patterns of global sea-level change.* Nature, 2001. **409**(6823): p. 1026-1029.

31. Edwards, R.L., *Paleotopography of glacial-age ice sheets.* Science, 1995. **267**: p. 536.

32. Peltier, W.R., *Paleotopgraphy of glacial-age ice sheets-reply.* Science, 1995.

267: p. 536-538.

33. Huybrechts, P., *Sea-level changes at the LGM from ice-dynamic reconstructions of the Greenland and Antarctic ice sheets during the glacial cycles.* Quaternary Science Reviews, 2002. **21**(1-3): p. 203-231.

34. Wu, P. and W.R. Peltier, *Viscous gravitational relaxation.* Geophysical Journal of the Royal Astronomical Society, 1982. **70**: p. 435-485.

35. Mitrovica, J.X. and W.R. Peltier, *On postglacial geoid subsidence over the equatorial oceans.* Journal of Geophysical Research-Solid Earth, 1991. **96**(B12): p. 20053-20071.

36. Johnston, P., *The effect of spatially nonuniform water loads on prediction of sea-level change.* Geophysical Journal International, 1993. **114**(3): p. 615-634.

37. Milne, G.A., *Recent Advances in Predicting Glaciation-Induced Sea-Level Changes and Their Impact on Model Applications*, in *Glacial Isostatic Adjustment and the Earth System: Sea Level, Crustal Deformation, Gravity and Rotation.* 2002. p. 157-176.

38. Milne, G.A. and J.X. Mitrovica, *Postglacial sea-level change on a rotating Earth.* Geophysical Journal International, 1998a. **133**(1): p. 1-19.

39. Mitrovica, J.X. and G.A. Milne, *On post-glacial sea level: I. General theory.* Geophysical Journal International, 2003. **154**(2): p. 253-267.

40. Peltier, W.R., *The impulse response of a Maxwell earth.* Rev. Geophys. Space Phys., 1974. **12**: p. 649.

41. Dziewonski, A.M. and D.L. Anderson, *Preliminary reference earth model (PREM).* Physics of the Earth and Planetary Interiors, 1981. **25**: p. 297-356.

42. Milne, G.A., *Refining models of the glacial isostatic adjustment process.* 1998, University of Toronto: Toronto, Canada.

43. Milne, G.A., J.X. Mitrovica, and J.L. Davis, *Near-field hydro-isostasy: the implementation of a revised sea- level equation.* Geophysical Journal International, 1999. **139**(2): p. 464-482.

44. Peltier, W.R., *Postglacial variations in the level of the sea: implications for climate dynamics and solid earth geophysics.* Review of Geophysics, 1998a. **36**: p. 603-689.

45. Stuiver, M., P.J. Reimer, E. Bard, J.W. Beck, G.S. Burr, K.A. Hughen, B. Kromer, F.G. McCormac, V.D. Plicht, and M. Spurk, *INTCAL98 radiocarbon age calibration, 24,000-0 cal BP.* Radiocarbon, 1998. **40**(3): p. 1041-1083.

46. Bard, E., B. Hamelin, R.G. Fairbanks, and A. Zindler, *Calibration of the ^{14}C timescale over the past 30,000 years using mass spectrometric U-Th ages from Barbados corals.* Nature, 1990a. **365**: p. 405-410.

47. Bard, E., B. Hamelin, and R.G. Fairbanks, *U-Th ages obtained by mass spectrometry in corals from Barbados: sea-level during the past 130,000 years.* Nature, 1990b. **346**: p. 456-458.

48. Bard, E., M. Arnold, R.G. Fairbanks, and B. Hamelin, *^{230}Th-^{234}U and ^{14}C ages obtained by mass spectrometry on corals.* Radiocarbon, 1993. **35**: p. 191-199.

49. Lighty, R.G., I.G. MacIntyre, and R. Stuckenrath, *Acropora Palmata reef framework. A reliable indicator of sea-level in the Western Atlantic for the past 10,000 years.* Coral Reefs, 1982. **1**: p. 125-130.

50. Radtke, U., R. Grün, and H.P. Schwarcz, *Electron spin resonance dating of the Pleistocene coral reef tracts of Barbados.* Quaternary Research, 1988. **29**: p. 197-215.

51. Pirazzoli, P.A., *Singapore Tide Guage (Horsburgh Lighthouse),* in *World Atlas of Holocene Sea-level Changes.* 1991, Elsevier: Amsterdam. p. 117.

52. Head, M.J. and W.J. Zhou, *Evaluation of NaOH leaching techniques to extract humic acids from palaeosols.* Nuclear Instruments and Methods in Physics Research B, 2000. **172**: p. 434-439.

53. Chichagova, O.A. and A.E. Cherkinsky, *Problems in radiocarbon dating of soils.* Radiocarbon, 1993. **35**(3): p. 351-362.

54. Kretschmer, W., G. Anton, M. Bergman, E. Finckh, B. Kowalzik, M. Klein,

M. Leigart, S. Merz, G. Morgenroth, I. Piringer, H. Küster, R.D. Low, and T. Nakamura, *^{14}C dating of sediment samples.* Nuclear Instruments and Methods in Physics Research B, 1997. **123**: p. 455-459.

55. Chen, Y. and H. Polach, *Validity of ^{14}C ages in sediments.* Radiocarbon, 1986. **28**(2A): p. 464-472.

56. Raymond, P.A. and J.E. Bauer, *Riverine export of aged terrestrial organic matter to the North Atlantic Ocean.* Nature, 2001. **409**: p. 497-499.

57. Edwards, R.L., J. Beck, G.S. Burr, D.J. Donahue, J.M.A. Chappell, A.L. Bloom, E.R.M. Druffel, and F.W. Taylor, *A large drop in atmospheric $^{14}C/^{12}C$ and reduced melting in the Younger Dryas, documented with ^{230}Th ages of corals.* Science, 1993. **260**: p. 962-968.

58. Chappell, J., A. Omura, T. Esat, M. McCulloch, J. Pandolfi, Y. Ota, and B. Pillans, *Reconciliation of late Quaternary sea levels derived from coral terraces at Huon Peninsula with deep sea oxygen isotope records.* Earth and Planetary Science Letters, 1996. **141**(1-4): p. 227-236.

59. Lambeck, K. and M. Nakada, *Late Pleistocene and Holocene sea-level change along the Australian coast.* Palaeogeography Palaeoclimatology Palaeoecology, 1990. **89**: p. 143-176.

60. Montaggioni, L.F., G. Cabioch, G.F. Camoinau, E. Bard, A. Ribaud-Laurenti, G. Faure, P. Déjardin, and J. Récy, *Continuous record of reef growth over the past 14k.y. on the mid-Pacific island of Tahiti.* Geology, 1997. **25**(6): p. 555-558.

61. Lambeck, K., *Lithospheric response to volcanic loading in the Southern Cook Islands.* Earth and Planetary Science Letters, 1981. **55**: p. 482-496.

62. Lambeck, K., P. Johnston, and M. Nakada, *Holocene glacial rebound and sea-level change in NW Europe.* Geophysical Journal International, 1990. **103**: p. 451-468.

63. Lambeck, K., *Glacial Rebound of the British isles-II. A high resolution, high precision model.* Geophysical Journal International, 1993. **115**: p. 960-990.

64. Forte, A.M. and J.X. Mitrovica, *A new inference of mantle viscosity based on*

a joint inversion of post-glacial rebound data and long-wavelength geoid anomalies. Geophysical Research Letters, 1996. **23**: p. 1147-1150.

65. Nakada, M. and K. Lambeck, *Late Pleistocene and Holocene sea-level change in the Australian region and mantle rheology.* Geophysical Journal International, 1989. **96**: p. 497-517.

66. Milne, G.A., J.L. Davis, J.X. Mitrovica, H.-G. Scherneck, J.M. Johansson, M. Vermeer, and H. Koivula, *Space-geodetic constraints on glacial adjustment in Fennoscandia.* Science, 2001. **291**: p. 2381-2385.

67. Marshall, S.J., T.S. James, and G.K.C. Clarke, *North American ice sheet reconstructions at the Last Glacial Maximum.* Quaternary Science Reviews, 2002. **21**: p. 175-192.

68. Denton, G.H. and T.J. Hughes, *Reconstructing the Antarctic ice sheet at the Last Glacial Maximum.* Quaternary Science Reviews, 2002. **21**(1-3): p. 193-202.

69. Peltier, W.R., *Global glacial isostasy and the surface of the ice-age Earth: The ICE-5G(VM2) model and GRACE.* Annual Review of Earth and Planetary Sciences, 2004. **32**: p. 111-149.

70. Milne, G.A. and J.X. Mitrovica, *The influence of time-dependent ocean-continent geometry on predictions of post-glacial sea level change in Australia and New Zealand.* Geophysical Research Letters, 1998b. **25**(6): p. 793-796.

71. Johnston, P. and K. Lambeck, *Postglacial rebound and sea level contributions to changes in the geoid and the Earth's rotation axis.* Geophysical Journal International, 1999. **136**(3): p. 537-558.

72. Kaufmann, G. and K. Lambeck, *Glacial isostatic adjustment and the radial viscosity profile from inverse modeling.* Journal of Geophysical Research-Solid Earth, 2002. **107**(B11): p. art. no.-2280.

73. Verleyen, E., D.A. Hodgson, G.A. Milne, K. Sabbe, and W. Vyverman, *Relative sea-level history from the Lambert Glacier region, East Antarctica, and its relation to deglaciation and Holocene glacier readvance.* Quaternary

Research, 2005. **63**(1): p. 45-52.

74. Latychev, K., J.X. Mitrovica, J. Tromp, M.E. Tamisiea, D. Komatitsch, and C.C. Christara, *Glacial isostatic adjustment on 3-D Earth models: a finite-volume formulation.* Geophysical Journal International, 2005. **161**(2): p. 421-444.

75. Bentley, M.J., *Volume of Antarctic ice at the Last Glacial Maximum, and its impact on global sea level change.* Quaternary Science Reviews, 1999. **18**(14): p. 1569-1595.

76. Anderson, J.B., S.S. Shipp, A.L. Lowe, J.S. Wellner, and A.B. Mosola, *The Antarctic Ice Sheet during the Last Glacial Maximum and its subsequent retreat history: a review.* Quaternary Science Reviews, 2002. **21**(1-3): p. 49-70.

77. Nakada, M. and K. Lambeck, *The melting history of the late Pleistocene Antarctic ice sheet.* Nature, 1988. **333**: p. 36-40.

78. Colhoun, E.A., M.C.G. Mabin, D.A. Adamson, and R.M. Kirk, *Antarctic ice volume and the contributions to sea-level fall at 20,00 yr BP from raised beaches.* Nature, 1992. **358**(316-318).

79. Ivins, E.R. and T.S. James. *Antarctic Glacioisotasy: A new assessment.* in *XXVIII SCAR Meeting.* 2005. Bremen.

80. Conway, H., B.L. Hall, G.H. Denton, A.M. Gades, and E.D. E. D. Waddington, *Past and future grounding-line retreat of the West Antarctic ice sheet.* Science, 1999. **286**(5438): p. 280-283.

81. Licht, K.L., *The Ross Sea's contribution to eustatic sea-level during meltwater pulse IA.* Sedimentary Geology, 2004. **165**: p. 343-353.

82. Bentley, M.J. and J.B. Anderson, *Glacial and marine geological evidence for the ice sheet configuration in the Weddell Sea Antarctic Peninsula region during the Last Glacial Maximum.* Antarctic Science, 1998. **10**(3): p. 309-325.

83. Hindmarsh, R. Available from: http://www.antarctica.ac.uk/Resources/Data/.

84. Stuiver, M., P.J. Reimer, and R.W. Reimer. *CALIB 5.0.* 2005. Available

from: http://radiocarbon.pa.qub.ac.uk/calib/.

85. Hall, B.L. and G.H. Denton, *New relative sea-level curves for the southern Scott Coast, Antarctica: evidence for Holocene deglaciation of the Western Ross Sea.* Journal of Quaternary Science, 1999. **14**: p. 641-650.

86. Kirk, R.M., *Raised beaches, late Quaternary sea-levels and deglacial sequences on the Victoria Land coast, Antarctica.*, in *Quaternary Research in Australian Antarctica:Future Directions*, D.S. Gillieson and F. D, Editors. 1991, Australian Defense Force Academy: Canberra. p. 85-105.

87. Berkman, P.A. and S.L. Forman, *Pre-bomb radiocarbon and the reservoir correction for calcareous marine species in the Southern Ocean.* Geophysical Research Letters, 1996. **23**(4): p. 363-366.

88. Gordon, J.E. and D.D. Harkness, *Magnitude and geographic-variation of the radiocarbon content in Antarctic marine life - implications for reservoir corrections in radiocarbon dating.* Quaternary Science Reviews, 1992. **11**(7-8): p. 697-708.

89. Baroni, C. and B.L. Hall, *A new Holocene relative sea-level curve for Terra Nova Bay, Victoria Land, Antarctica.* Journal of Quaternary Science, 2004. **19**(4): p. 377-396.

90. Hall, B.L., C. Baroni, and G.H. Denton, *Holocene relative sea-level history of the Southern Victoria Land Coast, Antarctica.* Global and Planetary Change, 2004. **42**(1-4): p. 241-263.

91. Bentley, M.J., D.A. Hodgson, J.A. Smith, and N.J. Cox, *Relative sea level curves for the South Shetlands and Marguerite Bay regions, Antarctic Peninsula.* Quaternary Science Reviews, 2005. **24**(10-11): p. 1203-1216.

92. Wassell, A. and H. Håkansson, *Diatoom strtigraphy in a lake on Horeshoe Island, Antarctica.* Diatom Research, 1992. **7**(1): p. 157-194.

93. Emslie, S.D. and J.D. McDaniel, *Ade'lie penguin diet and climate change during the middle to late Holocene in northern Marguerite Bay, Antarctic Peninsula.* Polar Biology, 2002. **25**(3): p. 222-229.

94. Takada, M., A. Tanib, H. Miura, K. Moriwaki, and T. Nagatomo, *ESR dating*

of fossil shells in the Lützow-Holm Bay region, East Antarctica. Quaternary Science Reviews, 2003. **22**(2003): p. 1323-1328.

95. Zwartz, D., M.I. Bird, J.O. Stone, and K. Lambeck, *Holocene sea-level change and ice sheet history in the Vestfold Hills, East Antarctica.* Earth and Planetary Science Letters, 1998. **155**: p. 131-145.

96. Zhang, Q. and J.A. Peterson, *A geomorphology and Late Quaternary geology of the Vestfold Hills, Antarctica.* ANARE, 1984. **133**.

97. Kaufmann, G., P. Wu, and E.R. Ivins, *Lateral viscosity variations beneath Antarctica and their implications on regional rebound motions and seismotectonics.* Journal of Geodynamics, 2005. **39**(2): p. 165-181.

98. Yokoyama, Y., M. Noumi, H. Miura, N. Ohkouchi, and H. Matsuzaki, *Rapid fluctuations of West Antarctic Ice Sheet during the last deglaciation recorded in the sediment cores from off the Antarctic Peninsula.* EOS Trans. AGU, 2005. **86**(52).

99. Wu, X.P., M.M. Watkins, E.R. Ivins, R. Kwok, P. Wang, and J.M. Wahr, *Toward global inverse solutions for current and past ice mass variations: Contribution of secular satellite gravity and topography change measurements.* Journal of Geophysical Research-Solid Earth, 2002. **107**(B11).

100. Wahr, J., M.D. Wingham, and C. Bentley, *A method of combining IceSat and GRACE satellites to constrain Antarctic mass balance.* Journal of Geophysical Research, 2000. **105**: p. 16,279-16,294.

101. Kaufmann, G., *Ice-ocean mass balance during the Late Pleistocene glacial cycles in view of CHAMP and GRACE satellite missions.* Geophysical Journal International, 2000. **143**: p. 142-156.